
Electronic Thesis and Dissertation Repository

11-21-2017 2:00 PM

Physical Properties Of Faint Meteors Through High-Resolution Observations

Dilini Subasinghe
The University of Western Ontario

Supervisor
Campbell-Brown, Margaret D.
The University of Western Ontario

Graduate Program in Astronomy
A thesis submitted in partial fulfillment of the requirements for the degree in Doctor of Philosophy
© Dilini Subasinghe 2017

Follow this and additional works at: <https://ir.lib.uwo.ca/etd>



Part of the [The Sun and the Solar System Commons](#)

Recommended Citation

Subasinghe, Dilini, "Physical Properties Of Faint Meteors Through High-Resolution Observations" (2017). *Electronic Thesis and Dissertation Repository*. 5077.
<https://ir.lib.uwo.ca/etd/5077>

This Dissertation/Thesis is brought to you for free and open access by Scholarship@Western. It has been accepted for inclusion in Electronic Thesis and Dissertation Repository by an authorized administrator of Scholarship@Western. For more information, please contact wlsadmin@uwo.ca.

Abstract

Small, faint meteors (with masses between 10^{-7} and 10^{-4} kg) were once part of an asteroid or comet, and collide with Earth's atmosphere daily. Studying meteors is an effective way to survey the physical properties of their parent bodies. Meteor light curves and orbital information is easily obtained from wide-field observations, from which meteoroid structure can be inferred through meteoroid ablation modelling. A high-resolution narrow-field camera can provide much more detail about the poorly understood ablation processes and physical properties of the meteoroid. The goal of this thesis is to better understand the physical properties of meteors using high-resolution optical observations.

In the first part of this work, wide-field and narrow-field optical observations of faint meteors were combined to determine what relationships, if any, exist between meteor light curve shapes, orbits, and fragmentation behaviour. Most meteors were found to have symmetric light curves, show fragmentation in the form of a long trail, and come from cometary bodies. More than 90% of meteors observed with the high-resolution camera system showed some form of fragmentation. Unexpectedly, the dynamically asteroidal meteoroids fragmented as often as the dynamically cometary meteoroids, suggestive of dynamical mixing or contamination.

In the second part of this work, the luminous efficiency (the fraction of kinetic energy used for visible light production) of meteors was investigated. It is crucial for determining meteoroid mass, and past results vary by up to two orders of magnitude. An attempt at determining luminous efficiency through the classical ablation equations was made, and verified on simulated meteor data, while quantifying the uncertainty in the method. This was then applied to fifteen real meteor events, observed with the Canadian Automated Meteor Observatory. This is the first study which compares photometric and dynamic meteoroid masses to determine luminous efficiency, with modern high-resolution observations. Twelve of the meteors had luminous ef-

efficiency values less than 1% (agreeing with the lower end results of past studies), and there was no obvious trend with speed. A weak negative trend was observed with meteoroid mass, implying that smaller meteoroids radiate more efficiently.

Keywords: meteors, meteoroids, optical observations, meteor fragmentation, asteroids, comets, meteor masses

Co-Authorship Statement

This thesis is based on three chapters that have either been previously published, or accepted for publication.

Chapter 3: Subasinghe, D., Campbell-Brown, M. D., and Stokan, E. 2016, “Physical characteristics of faint meteors by light curve and high-resolution observations, and the implications for parent bodies.” *Monthly Notices of the Royal Astronomical Society*, 457, 1289.

Chapter 4: Subasinghe, D., Campbell-Brown, M. D., and Stokan, E. 2017, “Luminous efficiency estimates of meteors -I. Uncertainty Analysis.” *Planetary and Space Science*, 143, 71.

Chapter 5: Subasinghe, D., and Campbell-Brown, M. D. 2017, “Luminous efficiency estimates of meteors -II. Application to Canadian Automated Meteor Observatory meteor events.” *The Astronomical Journal*, in press.

I performed the data analysis for each chapter and wrote each of the three manuscripts. My advisor Margaret Campbell-Brown provided guidance at all stages of my research, and gave advice and suggestions for each manuscript. Edward Stokan wrote the code to interpolate the meteor light curves, which was used in Chapters 3, 4, and 5, and provided suggestions and improvements for the manuscripts in Chapters 3 and 4.

All meteor observations were captured with the Canadian Automated Meteor Observatory, an automated system maintained by the Meteor Physics Group at the University of Western Ontario. The software programs METAL and mirfit, developed by Robert Weryk, were used to determine meteor trajectories and light curves.

Acknowledgements

Most importantly, I thank my supervisor Dr. Margaret Campbell-Brown for her guidance and support over the years. Her encouragement and confidence in me made this possible.

I also thank Dr. Peter Brown for inspiring me as an undergraduate student to continue studying astronomy, and for his help and suggestions over the years. Dr. Edward Stokan was a valuable mentor and a great friend throughout my time as a graduate student and I truly appreciate the advice he provided. I thank the Meteor Physics Group, past and present members, for their support and friendship.

I would like to thank the members of the Physics and Astronomy Department - staff, students, and faculty, for the interesting conversations and support which kept me going.

Finally, I thank my parents and siblings for their constant support.

Contents

Abstract	i
Co-Authorship Statement	iii
Acknowledgements	iv
List of Figures	viii
List of Tables	xi
1 Introduction	1
1.1 Motivation	1
1.2 Meteor Physics	2
1.2.1 Parent Bodies	4
1.2.2 Meteor light curves	7
1.2.3 Classical Model	9
1.2.4 Fragmentation	15
1.2.5 Ablation models	15
1.3 Luminous efficiency	18
1.4 Meteor observations	22
1.4.1 Visual	22
1.4.2 Photographic	23
1.4.3 Video	24
1.4.4 Spectral	24

1.5	Thesis Goals	25
2	Equipment and Data Reduction	32
2.1	The Canadian Automated Meteor Observatory	32
2.2	ASGARD	36
2.3	METAL	38
2.4	mirfit	38
2.5	Determining Luminous Efficiency	39
3	Classifying Meteors	43
3.1	Introduction	43
3.2	Equipment	49
3.3	Method and Classification	50
3.4	Results	54
3.4.1	High-Resolution Video Morphologies	54
3.4.2	Light Curve and Tisserand Parameter Data Distribution	56
3.4.3	Video morphology subsets	57
3.4.4	Parent class subsets	59
3.4.5	K_b parameter	60
3.4.6	Orbital elements	61
3.5	Discussion	62
3.6	Conclusions and Future Work	66
4	Luminous Efficiency -I	70
4.1	Introduction	70
4.1.1	Previous luminous efficiency studies	72
4.2	Method	76
4.2.1	Future application to real data	76
4.3	Sensitivity Analysis	77

4.4	Discussion	85
4.5	Conclusion	87
5	Luminous Efficiency -II	90
5.1	Introduction	90
5.2	Method Refinement	93
5.3	Equipment and Data Reduction	96
5.3.1	Equipment	96
5.3.2	Data Reduction	97
5.4	Results	101
5.4.1	Noise analysis	101
5.4.2	Atmospheric density variations	103
5.4.3	Photometry calibration	106
5.4.4	Meteoroid density	107
5.4.5	Error analysis	109
5.4.6	Meteor event 20161009_064237	109
5.4.7	Final Meteor results	111
5.4.8	Luminous Efficiency and mass	111
5.4.9	Fragmentation	115
5.5	Discussion	115
5.6	Conclusion	118
6	Conclusion	123
6.1	Thesis summary	123
6.2	Future Work	125
A	Copyright Permissions	128
	Curriculum Vitae	137

List of Figures

1.1	Meteoroid orbital elements	4
1.2	Meteor light curve shapes	9
1.3	Illustration of meteoroid-atmosphere interaction	10
1.4	Different types of meteoroid fragmentation	16
1.5	Past studies of luminous efficiency	23
1.6	Two-station observations of meteors	25
1.7	Meteor spectrum of a Geminid meteor	26
2.1	Map showing the locations of CAMO	33
2.2	Meteor observations from the wide-field camera vs narrow-field camera	34
2.3	Spectral response of the CAMO system image intensifier	34
2.4	The CAMO guided system	35
2.5	Sample photometric plate for the Elginfield wide-field camera	37
3.1	A sample meteor light curve with the two filters applied	52
3.2	Light curve shapes used to classify CAMO meteor events	54
3.3	The narrow-field video morphologies used to classify meteor events	55
3.4	The 1496 single-morphology, high-resolution videos, classified by their Tisserand parameter and morphology	57
3.5	Histogram of F parameters for 891 meteor events	58
3.6	Histogram of Tisserand parameters	58
3.7	Histograms of meteor events according to their light curve shapes	59
3.8	Meteor events sorted by their Tisserand parameter, and their light curve shape	60

3.9	K_b histograms for the three morphologies	61
3.10	Inclination versus eccentricity for all meteor events with acceptable convergence angles and velocities, that end onscreen	62
4.1	Past studies of luminous efficiency using various methods	75
4.2	Residual plots for fitting the entire lag versus the second half of the lag, with a two-term exponential	79
4.3	The relative percent error in deceleration when fitting the entire meteoroid lag versus fitting only the second half for a simulated meteor	80
4.4	The variation of luminous efficiency with the variables assumed to be constants during ablation	81
4.5	Atmospheric density variations over 2015 and their effect on the derived luminous efficiency	83
4.6	A comparison of the output from a simulated meteoroid to fitted equivalents based on a two-term exponential fit to the simulated lag	86
5.1	Single-term exponential fit to the standard event	95
5.2	Derived speed and deceleration profiles for the standard event based on the fitted lag	95
5.3	Derived luminous efficiency profile for the standard event	96
5.4	Examples of single-body ablation	99
5.5	A single frame from each each of the analysed meteors	102
5.6	Noise analysis for simulated meteor data	104
5.7	Atmospheric density variations (seasonal and solar) for a simulated meteor . . .	105
5.8	The analysis of meteor event 20161009_064237	112
5.9	Luminous efficiency as a function of initial speed	113
5.10	Luminous efficiency as a function of initial mass for non-fragmenting events . .	114

5.11 Luminous efficiency as a function of initial speed, assuming each meteoroid
has a bulk density of either 1000 kg/m^3 or 3000 kg/m^3 119

List of Tables

1.1	Major meteor showers	2
1.2	K_b parameter classification	7
2.1	Technical specifications of the CAMO system	34
3.1	Classification and description of meteors according to their K_b parameter	49
3.2	Classification categories used for the high-resolution video observations	56
4.1	Mean luminous efficiency value (percentage) for each mass - speed group of simulated meteor events	84
5.1	Standard event parameters	95
5.2	Parameter space used to simulate meteors	103
5.3	Meteoroid densities based on Tisserand parameters	108
5.4	Parameters for the twenty meteor events analysed for this work	110

Chapter 1

Introduction

1.1 Motivation

The goal of this thesis is to investigate the physical properties of faint meteors through optical observations. Small objects called *meteoroids* travel through the Solar system and may intersect the Earth's orbit. The plasma surrounding the meteoroid as it *ablates*, or loses mass, in the atmosphere is called a *meteor*. Most meteors are too small to survive ablation and reach the ground, which means that to study them, we need to either visit the objects in space, or observe their ablation and extract information. It is more cost efficient to study these objects from the ground, but simultaneously more difficult to extract information from observations that typically last less than one second, and do not produce an object that can be studied in a lab. These small objects hold valuable information about the conditions in the early Solar system: coming from comets and asteroids, meteoritic material is unprocessed and primitive, and allows us to study comets and asteroids remotely. In a practical sense, understanding meteoroids (their motion and physical properties) allows us to better protect our satellites, on which we rely heavily for daily life: being able to predict the timing of meteor outbursts can be used to schedule maintenance for spacecraft, and understanding how meteoroids behave upon impact can be used to improve material shielding, for both satellites/spacecraft, and astronauts.

Table 1.1: A few major meteor showers, taken from the IMO Meteor Shower Calendar 2017. All parent bodies are comets except for Phaethon, which is an asteroid.

Meteor Shower	Active	Peak	Parent Body	Speed (km/s)
Quadrantids	Dec 28 - Jan 12	Jan 3	96P/Machholz	41
Perseids	Jul 17 - Aug 24	Aug 12	109P/Swift-Tuttle	59
Orionids	Oct 2 - Nov 7	Oct 21	1P/Halley	66
Leonids	Nov 6 - 30	Nov 17	55P/Tempel-Tuttle	71
Geminids	Dec 4 - 17	Dec 14	3200 Phaethon	35

1.2 Meteor Physics

Meteoroids hit the Earth's atmosphere with speeds between 11 and 72 km/s, with the limits corresponding to the object either hitting the Earth head-on at maximum bound speed, or 'catching up' to the Earth in a similar orbit. Once in the atmosphere, meteoroids begin to ablate as they encounter more atmospheric particles. As the meteoroid moves through the atmosphere, inelastic collisions between atmospheric molecules and vaporised meteoroid molecules cause the particles to become ionised and/or excited. Visible radiation is emitted by these meteoritic and atmospheric particles, and results in a meteor. Faint meteors are produced by meteoroids that are typically less than a millimetre in size, have peak magnitudes fainter than +2, and will completely ablate in the atmosphere, often in less than one second. The position in the sky where a meteor appears to originate from is called the radiant, and meteors belonging to a shower will all have the same radiant. Table 1.1 lists a few strong meteor showers. Meteor showers are observed when the Earth's orbit intersects a meteoroid stream, which is a group of meteoroid particles orbiting the Sun in orbits similar to their parent body (the object in space from which they detached). Meteor showers are named for the constellation in which the radiant lies.

Meteors not associated with any particular meteor shower are called sporadic meteors, and

may originate from any part of the sky, but tend to be part of broad radiant groups. Sporadic meteors are far more numerous than shower meteors (Campbell-Brown, 2007), and were once part of meteoroid streams, but their orbits have dispersed enough since the initial separation from their parent body that they cannot be associated with any particular stream. Often the Tisserand parameter is used to determine whether a meteoroid came from an asteroid, a long period comet, or a short period comet; the Tisserand parameter is based on the orbital parameters of that meteor. The three principal orbital parameters of an object are the *semi-major axis*, which is the average of the minimum and maximum heliocentric distances; the *inclination*, which describes how inclined the orbit is relative to the ecliptic plane¹ (can range from 0 to 180°); and the *eccentricity*, which describes how elliptical the orbit is (an eccentricity of 0 describes a circle, between 0 and 1 describes an ellipse, and a value greater than 1 describes a hyperbolic orbit). The line formed by the intersection of the orbital plane and the ecliptic plane is called the line of nodes, and there are two locations where the meteoroid orbit passes through the ecliptic plane. These are called the ascending and descending nodes. Three other orbital elements are required to uniquely determine the location of an object in its orbit. The *longitude of the ascending node* is the angle from a fixed direction in the ecliptic plane to the direction of the ascending node; the *argument of perihelion* is the angle between the ascending node and perihelion (the point in the meteoroid orbit that is closest to the Sun)² and the *true anomaly* describes the angle between the meteoroid's perihelion and instantaneous location. Some of these orbital elements and parameters are illustrated in Figure 1.1. The Tisserand parameter relative to Jupiter (e.g. de Pater & Lissauer, 2010) is defined as:

$$T_J = \frac{a_J}{a} + 2 \left[(1 - e^2) \frac{a}{a_J} \right]^{1/2} \cos(i) \quad (1.1)$$

where a parameter without a subscript is the heliocentric orbital element of the object, and a subscript of J means belonging to Jupiter. The Tisserand parameter assumes that the Sun and

¹The ecliptic plane is the plane in which Earth orbits the Sun.

²A value of 0 for the argument of perihelion means the meteoroid will be closest to the Sun at the same time it crosses the ecliptic plane.

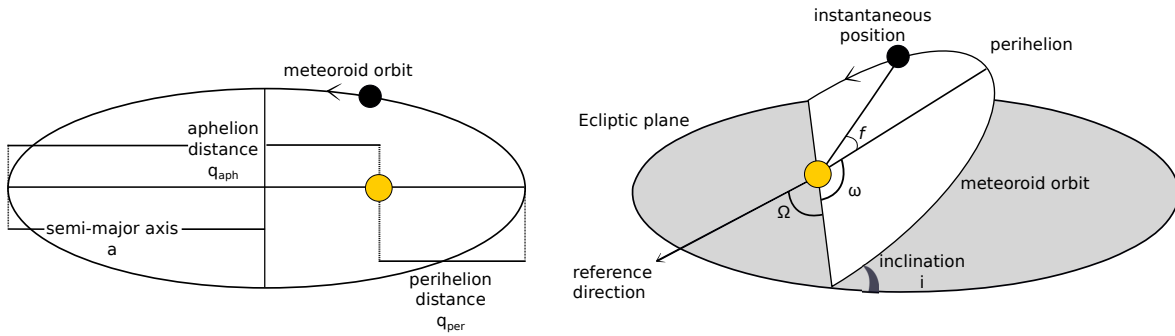


Figure 1.1: The orbital elements for a meteoroid. The figure on the left is a top down view showing the semi-major axis. The aphelion distance and perihelion distance are labelled, and are the distances farthest away and closest to the Sun respectively. The figure on the right shows the inclination i , the longitude of the ascending node Ω , the argument of perihelion ω , and the true anomaly f . The ecliptic plane is in grey, and the meteoroid orbit is white.

Jupiter are on circular orbits; that the meteoroid is only affected by perturbations by Jupiter; and that the mass of the meteoroid is negligible relative to Jupiter. The Tisserand parameter remains constant despite perturbations from Jupiter, and allows the meteoroid to be associated with a class of Solar system bodies. Values greater than 3 describe objects with asteroidal origins; $2 < T_J \leq 3$ describe objects originally from Jupiter family comets; and values less than or equal to 2 describe Halley-type orbits. The Tisserand parameter of an object can be altered through encounters with other planets and radiation forces, however it is a useful proxy for meteoroid origin. Knowing the meteoroid parent body, or even the class of parent body can help with inferring meteoroid properties, since the location in the Solar system where the object formed will define the structure of the body.

1.2.1 Parent Bodies

Meteoroids are released from comets and asteroids, either through outgassing, collisions, rotational bursting after spin-up from YORP³, or thermal disruption. When the meteoroid's orbit brings it into Earth's atmosphere, we can study it as it ablates and learn about the object it originally came from.

³The YORP (Yarkovsky-O'Keefe-Radzievskii-Paddack) effect can change the rotation state of a small Solar system body through thermal torques (reflection and re-emission of solar radiation).

Comets and asteroids are primitive bodies and the material of which they are composed can be thought of as a snapshot of the conditions of the early Solar system. Comets are formed in the outer regions of the Solar system (in the Oort Cloud and Kuiper Belt), and make their way towards the inner Solar system on elliptical orbits. The icy comet model proposed by Whipple (1950, 1951) suggests that comets are clusters of icy material, volatile molecules, and meteoritic material, and are fragile and porous. Asteroids are rocky objects that are mainly found in orbit between Mars and Jupiter. These primitive pieces of rock were unable to coalesce into larger objects due to the gravitational pull of Jupiter.

The first material to be collected in situ and studied on Earth from a known object (not including the Moon) came from comet 81P/Wild 2 during the Stardust mission (Brownlee et al., 2006). Material was captured onto low-density aerogel at a relative speed of 6.1 km/s, and the different types of cometary material showed different behaviour upon impact with the gel. Non-fragmenting particles showed long carrot shaped streaks in the gel, while particles that fragmented showed bulbs with many roots (Brownlee et al., 2006). A major finding from the Stardust mission was evidence for the movement of material from the inner to the outer regions of the Solar system during the formation of comet 81P/Wild 2. The collected material contained minerals that require high temperatures to form; this is suggestive of radial mixing in the early Solar system (Brownlee et al., 2006). The Rosetta mission visited comet 67P/Churyumov-Gerasimenko and released a robotic lander (Philae) onto the surface in 2014 – this was the first soft landing of a spacecraft on a comet nucleus. The Grain Impact Analyzer and Dust Accumulator (GIADA) instrument on Rosetta collected millimetre-sized particles that were found to be either compact processed particles with bulk densities between 800 and 3000 kg/m³ (Rotundi et al., 2015), or fluffy aggregates of submicron grains with bulk densities less than 1 kg/m³ (Fulle et al., 2015). The particles analysed by GIADA were collected at very low speeds (typically a few metres per second), and some particles (with sizes up to 225 μm) were used for chemical analysis by the COmetary Secondary Ion Mass Analyser (COSIMA) instrument (Hilchenbach et al., 2016). The non-fragmenting particles captured during the Stardust mission

may be similar to the compact particles collected with GIADA, while the fragmenting particles that left bulbous tracks may be the same as the low density fluffy particles. These results are indicative of comets being composed of material of differing strengths. However, the particles analysed by Rosetta were recently ejected, and their properties may change over time as they are subjected to processes such as collisions, or sublimation because of solar radiation.

Asteroidal material has also been collected from space and returned to Earth with the Hayabusa mission in 2010. The returned particles had diameters between 3 and 10 μm , and results indicated that the most commonly found type of meteorite (ordinary chondrites), come from siliceous type asteroids (Nakamura et al., 2011). Chondrites contain both chondrules and calcium-aluminium inclusions (CAIs), which contain refractory minerals, which would have formed in high-temperature environments, embedded in a fine grained matrix. At least one particle from the Stardust mission was mineralogically and isotopically linked to CAIs, and is taken as evidence for the movement of material from the inner to the outer Solar system (Brownlee et al., 2006).

In 1958 Ceplecha defined the K_b parameter, given in Equation 1.2:

$$K_b = \log \rho_b + 2.5 \log v_\infty - 0.5 \log \cos(z_R) \quad (1.2)$$

where ρ_b is the atmospheric density at the beginning of the luminous path; v_∞ is the pre-atmospheric velocity; and z_R is the zenithal angle of the radiant. This parameter attempts to classify meteoroids by their strength, or composition, and is often used to determine meteoroid densities.

The K_b parameter classifies meteors into five main groups: A, B, C, D, and asteroidal, and each group is associated with a different type of material. The K_b parameter assumes that meteoroids begin to be luminous at the same surface temperature, meaning the meteoroid begin height is strongly related to the meteoroid composition⁴. The groups refer to meteoroids in the

⁴A meteoroid composed of pure iron will require more energy (and thus will travel deeper into the atmosphere) to become luminous relative to a meteoroid composed of a more volatile material.

Table 1.2: Classification of meteors by their K_b parameter. The bulk density values are from Ceplecha (1988). Group C can be further divided into three groups depending on orbital parameters.

Group	K_b	Bulk density (kg/m ³)
Asteroidal	> 8	3700
A	7.3 - 8	2000
B	7.1 - 7.3	1000
C	6.6 - 7.1	750
D	< 6.6	270

millimetre to centimetre size range, with their values given in Table 1.2.

The K_b parameter depends on the meteoroid begin height, and is thus sensitive to the sensitivity of the camera used for observations. This means that an offset may need to be applied to K_b parameters depending on the system sensitivity. Researchers have attempted to relate the meteoroid density with the K_b parameter, and there is disagreement between results regarding which densities belong in each group (Kikwaya et al., 2011; Bellot Rubio et al., 2002; Ceplecha et al., 1998).

1.2.2 Meteor light curves

Meteors emit visible radiation which is due to excited meteoritic and atmospheric molecules and atoms. The observed brightness I (in units of radiant power, watts) can be converted to an apparent photometric magnitude m_{ph} , with Equation 1.3, where C is a calibration constant.

$$m_{ph} = -2.5\log_{10}I + C \quad (1.3)$$

Because magnitudes are defined through a negative logarithmic scale, brighter objects have smaller or more negative magnitudes, and fainter objects have larger positive magnitudes. The apparent meteor magnitude, which depends on the location of the observer, is often not used. Instead, the meteor absolute magnitude is used; it is the magnitude the meteor would have if

placed at a height of 100 km at the zenith. Mathematically, this conversion can be determined through Equation 1.4, and takes into account the distance R , of the meteor to the instrument.

$$M_{abs} = m_{ph} + 5\log_{10}\left(\frac{100 \text{ km}}{R}\right) \quad (1.4)$$

The observed meteor brightness as a function of time or height is called the *light curve*. Meteor light curves show a variety of profiles. The relative position of the maximum brightness to the length of the entire light curve can be described by the F parameter, given in Equation 1.5,

$$F = \frac{h_{\text{beg}} - h_{\text{max}}}{h_{\text{beg}} - h_{\text{end}}} \quad (1.5)$$

where h_{beg} and h_{end} refer to the beginning and ending heights of the observed meteoroid ablation, and h_{max} is the height at which maximum brightness is observed. The F parameter is a normalized value, where a value of 0.5 describes a symmetric light curve; values greater than 0.5 describe a late peaked light curve; and values less than 0.5 describe early peaked light curves. Jacchia (1955) noted that faint meteors, recorded by the Baker Super-Schmidt cameras at Harvard University in the early 1950s, showed light curve shapes that differed from those predicted by classical meteoroid ablation theory. Classical meteoroid theory suggests that solid, single-bodied objects that do not fragment will produce light curves with late peaks. Studies of both sporadic and shower meteors found that faint meteors typically have symmetric light curves, and that even within a meteor shower, meteors have a variety of F parameter values (Murray et al., 1999; Koteň & Borovička, 2001). Fleming et al. (1993) studied 34 double station meteors and analysed the light curves by determining points up to 3 magnitudes fainter than the maximum and finding the F parameter. For magnitude differences of 1.0 and 2.0, the average F parameter was 0.51. Early, symmetric, and late-peaked are not the only possible meteor light curve shapes – Vaubaillon et al. (2015) reported unexpectedly flat light curves for around 80 Draconids (and those that did show an obvious peak, had an average F parameter of 0.5). Examples of these studied light curve shapes are illustrated in Figure 1.2. The shape

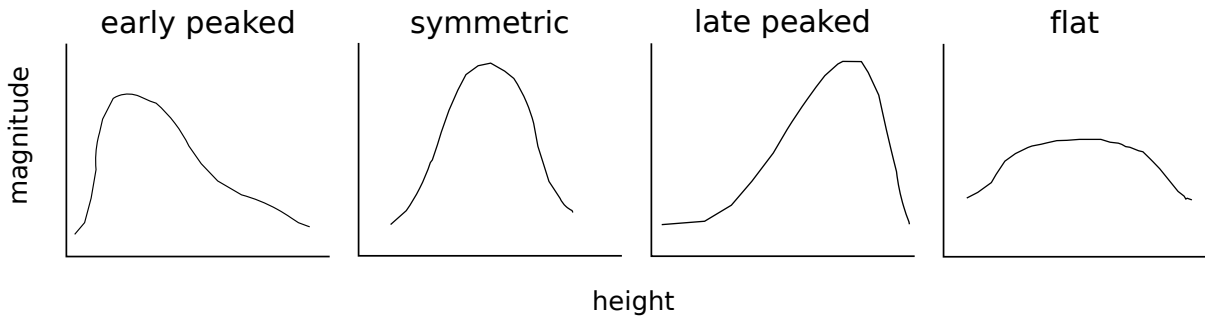


Figure 1.2: Illustrations of different types of observed light curve shapes. In each plot, the height is increasing to the left.

of the light curve is often used to infer whether the meteoroid fragmented (and when) during its ablation. Classical light curves are produced by objects that ablate as self-similar bodies and do not fragment. The late peak is due to the competition between the atmospheric density increase and the cross-sectional area decrease with height (more details are found in Section 1.2.3). However, if a meteoroid fragments, its cross-sectional area will increase, causing the meteoroid rate of ablation to increase, which in turn causes the meteor brightness to increase. This leads to an early peaked light curve if the fragmentation occurs early in the ablation process.

1.2.3 Classical Model

Modelling a meteor observation can be an effective method for determining physical properties of that particular event. The simplest ablation model assumes that the object does not fragment. While this is not an accurate assumption for the majority of meteoroids, it is an appropriate first step in modelling these complicated objects. The classical meteoroid ablation model is derived for an object that is solid and non-fragmenting, and is based on conservation of momentum and energy. There are four equations that form the basis of the classical model, which are derived below (Bronshten, 1983).

If we assume the meteoroid is a solid spherical body with cross-sectional area S , moving with a velocity v , in an atmosphere with a mass density of ρ_{atm} , within a time dt , the meteoroid will carve out a volume V equivalent to $V = S v dt$, illustrated in Figure 1.3. The mass of the

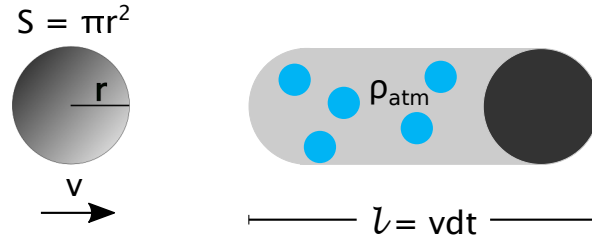


Figure 1.3: Illustration of a meteoroid (with radius r and cross-sectional area S) interacting with atmospheric particles. l is the distance travelled in time step dt .

atmospheric particles encountered in that volume is simply:

$$\begin{aligned} m_{atm} &= \rho_{atm} V \\ &= \rho_{atm} S v dt. \end{aligned} \tag{1.6}$$

The atmospheric particles are approximately stationary compared to the meteoroid⁵. We now switch the reference frame such that the meteoroid is stationary and the initial velocity of the atmospheric particles can be given as $v_{atm,i} = -v$. Momentum is conserved and there are two end cases for the final velocity of an atmospheric particle following a collision with a meteoroid: either the collision is totally elastic, and $v_{atm,f} = +v$, or the collision is totally inelastic, and $v_{atm,f} = 0$. The elasticity of the collision is given by the drag coefficient, Γ , which has a range between 0 and 2, where a value of 2 represents a totally elastic collision, and a value of 1 represents a totally inelastic collision⁶. The final velocity of the atmospheric particle

⁵The atmospheric particles have speeds <1 km/s, compared to meteor speeds which range from 11 - 72 km/s.

⁶A value less than 1 represents the situation in which atmospheric particles deflect off the side of the meteoroid without transferring momentum.

can thus be given as $v_{atm,f} = (\Gamma - 1)v$. We can now consider conservation of momentum:

$$\begin{aligned}
 \Delta p_m &= -\Delta p_{atm} \\
 &= -(m_{atm}(\Gamma - 1)v - m_{atm}(-v)) \\
 &= -\Gamma m_{atm}v \\
 &= -\rho_{atm}Sv\Delta t\Gamma \\
 &= -\rho_{atm}Sv^2\Gamma\Delta t
 \end{aligned} \tag{1.7}$$

The force on the meteoroid is

$$F = \frac{\Delta p_m}{\Delta t} \tag{1.8}$$

from which the deceleration can be found⁷.

$$\frac{dv}{dt} = \frac{F}{m} = -\frac{\rho_{atm}Sv^2\Gamma}{m} \tag{1.9}$$

Conservation of energy may be considered for determining the mass loss equation for meteoroid ablation, which is derived here in the frame of reference where the meteoroid is at rest and the atmospheric particles have $v_{atm,i} = -v$. The energy imparted to the meteoroid by the atmospheric particles is given by:

$$\begin{aligned}
 \Delta E_m &= -\Delta E_{atm} \\
 &= -\left(\frac{1}{2}m_{atm}v_{atm,f}^2 - \frac{1}{2}m_{atm}v_{atm,i}^2\right) \\
 &= -\left(\frac{1}{2}m_{atm}((\Gamma - 1)v)^2 - \frac{1}{2}m_{atm}(-v)^2\right) \\
 &= \frac{1}{2}m_{atm}v^2(\Gamma(2 - \Gamma)) \\
 &= \frac{1}{2}\rho_{atm}Sv^3\Gamma(2 - \Gamma)\Delta t.
 \end{aligned} \tag{1.10}$$

⁷There is a $v\frac{dm}{dt}$ term in the expansion of Equation 1.8 when looking at the force on the meteoroid, however we are only interested in the deceleration of the meteoroid. The lost mass is moving at the same speed as the meteoroid, and does not cause a change in the meteoroid velocity.

The power is then $P = \Delta E_m / \Delta t = \frac{1}{2} \rho_{atm} S v^3 \Gamma (2 - \Gamma)$. This is the energy used for increasing the temperature of the meteoroid and ablating (evaporating or sublimating) the meteoritic material in time dt . Some fraction ψ of this incoming energy ablates the meteoroid. The energy needed to ablate the meteoroid mass in time dt is given by $L \frac{dm}{dt}$, where L is the heat of ablation (energy needed to ablate a unit of mass), which includes the heat of fusion and heat of vaporisation. The meteoroid mass loss can be described with:

$$\begin{aligned} \frac{dm}{dt} &= - \frac{\psi dE}{L dt} \\ &= - \frac{\psi \rho_{atm} S v^3 \Gamma (2 - \Gamma)}{2L} \\ &= - \frac{\Lambda \rho_{atm} S v^3}{2L} \end{aligned} \tag{1.11}$$

where the heat transfer coefficient Λ has been introduced to simplify the expression. Equation 1.11 shows that the rate of ablation is proportional to the cross-sectional area of the meteoroid and the atmospheric density. The interaction between the two variables is the reason late peaked light curves occur in the classical model: the atmospheric density increases more quickly than the cross-sectional area decreases when the meteoroid begins ablating (causing a slow increase in brightness), but as the meteoroid mass approaches zero, the cross-sectional area decreases much more quickly, causing the drop at the end of the light curve. If a meteoroid fragments, its cross-sectional area will increase much faster, increasing the rate of ablation (mass loss), and thus the brightness. This can cause an early peak, or a flare, depending on when the fragmentation occurs.

The meteoroid brightness is related to the mass loss of the object. As the meteoroid ablates, it loses energy and some fraction of that energy is used to produce light. The proportionality constant between the light produced and the rate of kinetic energy lost is called the luminous efficiency, denoted τ ; it is poorly understood (e.g. Verniani, 1965; Ceplecha et al., 1998; Weryk

& Brown, 2013). The meteoroid intensity (the radiated luminous power) can be described by

$$\begin{aligned}
 I &= -\tau \frac{dE_k}{dt} \\
 &= -\tau \frac{d}{dt} \left(\frac{mv^2}{2} \right) \\
 &= -\tau \left(\frac{v^2}{2} \frac{dm}{dt} + mv \frac{dv}{dt} \right).
 \end{aligned} \tag{1.12}$$

The right side of the equation is negative because both the mass loss and deceleration terms are negative. Often, the deceleration term (the second term) is discarded and a simplified version (given below) is used for meteoroid ablation modelling:

$$I = -\frac{\tau v^2}{2} \frac{dm}{dt}. \tag{1.13}$$

The deceleration term is equal in importance to the mass loss term for low speed meteors (around 7 km/s)⁸, but decreases rapidly in importance as speed increases.

The temperature equation can also be derived using conservation of energy. There are three effects to consider: the energy gained from the atmosphere; the energy used for ablation; and the energy emitted as blackbody radiation. The energy gained from the atmosphere in time dt is given by:

$$\frac{dE_k}{dt} = \frac{\Lambda \rho_{atm} S v^3}{2}. \tag{1.14}$$

The energy used for ablation is $L \frac{dm}{dt}$. The energy emitted by the meteoroid as radiation is given by

$$\frac{dE_R}{dt} = 4\sigma\epsilon(T_m^4 - T_a^4)S \tag{1.15}$$

where σ is the Stefan-Boltzmann constant; ϵ is the emissivity of the meteoroid; T_m is the

⁸Meteoroids will not enter Earth's atmosphere with speeds less than 11 km/s, but will slow down as they encounter more atmospheric particles, allowing for these low speeds.

meteoroid temperature; and T_a is the atmospheric temperature.

The change in meteoroid temperature can be calculated as the change in energy with $dT_m = \frac{dE}{cm}$, where c is the specific heat of the meteoroid, and m is the meteoroid mass affected by the heating. Combining the heating and cooling effects gives the temperature equation.

$$\frac{dT}{dt} = \frac{1}{cm} \left(\frac{\Lambda \rho_{atm} S v^3}{2} - 4\sigma\epsilon(T_m^4 - T_a^4)S - L \frac{dm}{dt} \right) \quad (1.16)$$

Ablation models either use the temperature equation for ablation until the boiling temperature is reached, at which point the mass loss equation is used, or the temperature equation is used simultaneously with the mass loss equation.

These four equations (given in Equations 1.17 to 1.20) describing meteoroid deceleration, mass loss, intensity, and temperature, are the basis of many meteoroid ablation models and together describe what is called a classical meteor.

$$\frac{dv}{dt} = -\frac{\rho_{atm} S v^2 \Delta t \Gamma}{m} \quad (1.17)$$

$$\frac{dm}{dt} = -\frac{\Lambda \rho_{atm} S v^3}{2L} \quad (1.18)$$

$$I = -\tau \left(\frac{v^2}{2} \frac{dm}{dt} + mv \frac{dv}{dt} \right) \quad (1.19)$$

$$\frac{dT}{dt} = \frac{1}{cm} \left(\frac{\Lambda \rho_{atm} S v^3}{2} - 4\sigma\epsilon(T_m^4 - T_a^4)S - L \frac{dm}{dt} \right) \quad (1.20)$$

The variables in these equations do not always describe equivalent properties of a meteoroid. In Equation 1.17, the m variable defines the *dynamic* mass, which (if a meteoroid is fragmenting) is the largest and brightest piece of the meteoroid. In Equation 1.19, the m variable refers to the *photometric* mass, which is based on the light produced by all pieces of the meteoroid that are radiating light. In the classical model, the meteoroid does not fragment, and in that case, the photometric and dynamic masses are equivalent. However, most meteoroids

fragment so researchers must be careful in equating the two. A meteoroid following these equations will show a late peaked light curve (sometimes referred to as a classical light curve), but as discussed in Section 1.2.2, this is often not what is observed.

1.2.4 Fragmentation

Early studies assumed that meteoroids did not fragment and that they ablated as self similar objects, but as observational systems improved, it became clear that fragmentation is a commonly occurring process. Meteoroids can fragment in two ways, either by *gross fragmentation*, in which significant pieces break off during the meteoroid ablation, or *continuous fragmentation*, in which meteoritic particles are smoothly sloughed off the main body, as shown in Figure 1.4. The classical ablation model gained support from observations of bright meteors prior to the 1950s (McKinley, 1961); objects seemed to ablate as solid, non-fragmenting bodies. Fragmentation was suggested following a study of faint meteors by Jacchia (1955) (although he notes that he is not the first to suggest it), which found many anomalies between the observations and the theoretical classical predictions. Jacchia noted that the faint meteors recorded by the Harvard Super Schmidt cameras ablated more quickly than theory predicted; the decelerations occurred much faster than expected; and the meteors showed non-classical, symmetric light curves. He proposed that meteoroids undergo progressive fragmentation, in line with the icy-comet model put forth by Whipple (1950, 1951). Jacchia (1955) suggested that meteoroids are porous objects which are quite fragile, and that fragmentation is not a rare occurrence.

1.2.5 Ablation models

The dustball structure proposed by Jacchia (1955) was explained quantitatively by Hawkes & Jones (1975) in their *dustball* model. The model assumes that meteoroids are conglomerates of grains held together by a ‘glue’. The glue is a volatile matrix with a lower boiling temperature than the grains. Once the boiling temperature is reached, the glue vaporises, the grains are released, and each grain ablates according to the classical model. No luminosity is attributed

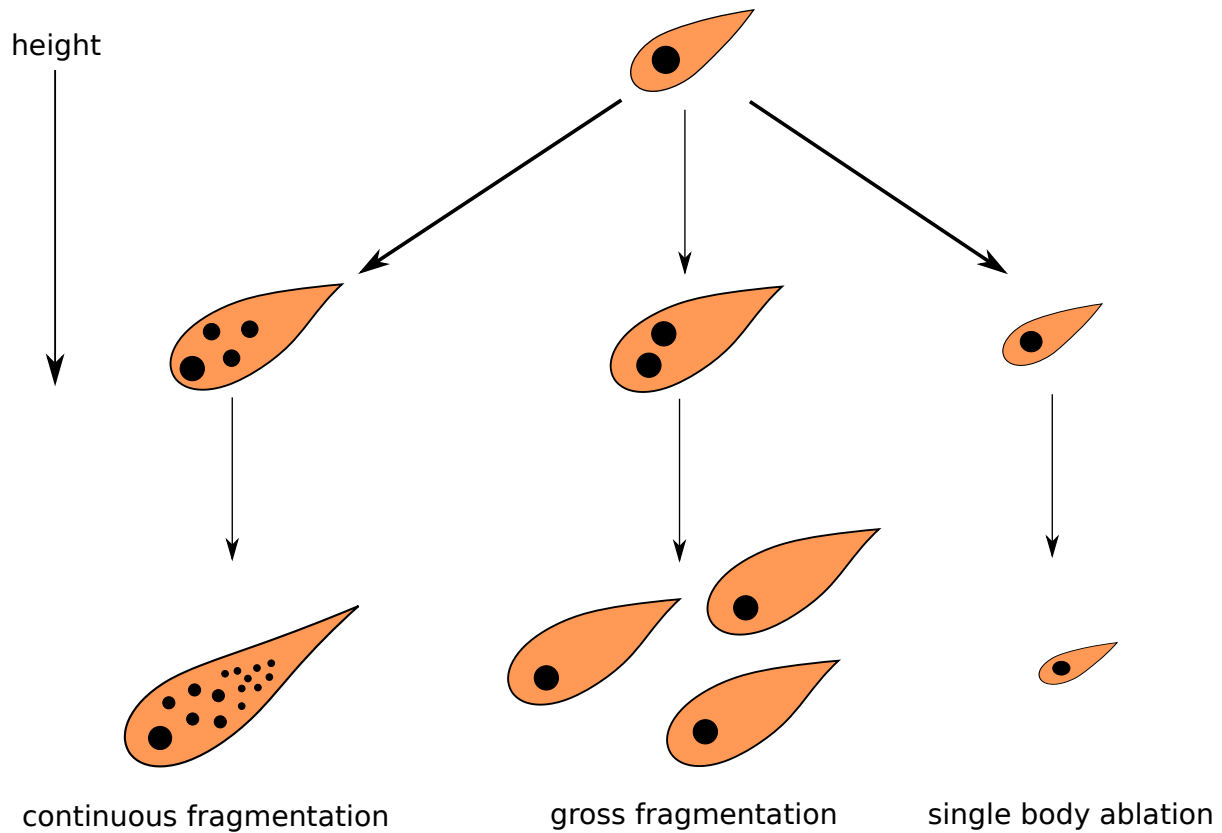


Figure 1.4: Illustration of different types of meteoroid fragmentation. The first example is of continuous fragmentation, where fragments smaller than the meteoroid are constantly removed, and contribute to the observed meteor light. The second example is of gross fragmentation, where the meteoroid fragments a number of times into pieces large enough that they can be distinguished with high-resolution systems. The third example is of single-body ablation, in which the meteoroid does not fragment at all.

to the heating and vaporisation of the glue. Hawkes & Jones (1975) found that their model was successful in reproducing the shorter light curves seen by Jacchia (1955), as well as the shape of the observed light curves.

A modified version of the dustball model was implemented by Campbell-Brown & Koschny (2004) that included a thermal disruption component. In this, the grains are released when the meteoroid surface reaches a specified temperature; typically, all fragments are released early on. Rather than using the classical mass loss equation (Equation 1.18), Campbell-Brown & Koschny (2004) use the Knudsen-Langmuir formula with the Clausius-Clapeyron equation. The Knudsen-Langmuir formula determines the mass loss due to evaporation and the Clausius-Clapeyron equation gives the saturation vapour pressure. These are used because meteoroid mass loss begins prior to the surface reaching the boiling temperature. Another modification to the original dustball model is that the grains have a mass distribution, rather than a single value. Changing the type of distribution gives different shaped light curves. The Campbell-Brown & Koschny (2004) model was successfully tested on three Leonid meteors.

A thermal erosion dustball model was introduced by Borovička et al. (2007), in which grains are continuously detaching from the main body. This model uses the classical ablation equations; however, the mass loss equation has an additional term for the mass lost due to erosion. The grains in the eroded mass ablate classically. Seven Draconid meteors were modelled with this implementation of the dustball model.

Campbell-Brown et al. (2013) applied these two variations of the dustball model on ten meteors observed with the Canadian Automated Meteor Observatory. The thermal erosion model was more successful at reproducing the observed meteor light curves and deceleration curves than the thermal disruption model. However neither model was particularly successful at reproducing the observed brightness in the high-resolution system. This work showed two models reproducing wide-field observations using different fragmentation processes, but neither truly describing the mass loss processes occurring. Additionally, changing the size and mass distribution of grains, as well as the timing of the meteoroid fragmentation can create a

variety of meteor light curve shapes. As there are many parameters that can be adjusted in any given ablation model, an increase in the number and type of observations will only improve our understanding of meteoroid ablation processes and meteoroid physical properties by providing new constraints for ablation parameters.

1.3 Luminous efficiency

The luminous efficiency factor, given in Equation 1.19, is the fraction of meteoroid kinetic energy used for visible light production. If this value is well known the meteoroid mass may be computed. Many authors have utilised various methods for determining luminous efficiency, and the results do not agree well with one another. The lack of understanding of the luminous efficiency is the main limitation to extracting meteoroid masses from optical observations. The difficulty in determining the meteoroid luminous efficiency is that it may depend on many factors: the spectral range of the camera; the meteoroid speed and composition; the atmospheric composition; and possibly the meteoroid mass. The meteoroid composition and speed will determine which spectral lines will be emitted, and the spectral response of the camera will determine which lines will be seen (which will determine the intensity of observed light). The poor grasp on meteoroid masses is a large problem even for those strictly outside the field of meteor physics – those who design and build spacecraft need an accurate idea of the dangers their products will face. Anyone who depends on a satellite for day to day activities (internet, cell phone, GPS, precision timers, weather trackers, etc) can be seriously inconvenienced if a satellite is damaged due to a meteoroid impact, and though rare, this has happened in the past (Caswell et al., 1995).

Early studies regarding luminous efficiency tended towards theoretical calculations involving atomic collisions and their subsequent radiation. A great deal of work was put forth by Öpik (1933, 1955); however, the results have been called into question and are almost exclusively listed in papers for historical completion. Verniani (1965) states that the number of assump-

tions made by Opik make determining the uncertainty in his results impossible, and Thomas & Whipple (1951) dismiss the work due to a number of theoretical errors.

The Harvard Photographic Meteor Project began in 1936 (Jacchia & Whipple, 1956) and produced some of the highest quality meteor observations of the twentieth century. A pair of large cameras (Baker-Super-Schmidt cameras, which were used in the 1950s) photographed 3500 double station meteors over a period of two years. A set of 413 meteors recorded through this program were selected (those with the longest and brightest trails to ensure the highest quality speed and deceleration results) and reduced by Jacchia & Whipple (1961). From this data set, Verniani (1965) determined the luminous efficiency using the drag equation (1.17) and the luminous intensity equation (1.19). He disregarded the second term in the luminous intensity equation (as many authors have done), claiming that there is no light contribution from the deceleration of the meteoroid (other authors state that the deceleration term is negligible compared to the mass loss term). By equating the dynamic and photometric masses, Verniani was able to determine the luminous efficiency. This equality explicitly assumes that the meteoroid does not fragment, and ablates as a single body. Because most of the meteors observed with the Super-Schmidt cameras show fragmentation, Verniani takes this into account and corrects his results.

Assuming that the luminous efficiency is proportional to a constant τ_0 multiplied by the meteoroid speed to some exponent, n , as shown in Equation 1.21, Verniani (1965) found that for one non-fragmenting meteor, assumed to be asteroidal in origin, in the photographic bandpass, $\log_{10} \tau_0 = -4.37 \pm 0.08$ for $n = 1$.

$$\tau = \tau_0 v^n \tag{1.21}$$

The non-fragmenting event was studied by Cook et al. (1963), who suggested the asteroidal origin, and of the six position measurements taken, Verniani (1965) used four to determine his results. The Verniani (1965) results form the basis of many meteor studies today (e.g. Ceplecha & McCrosky, 1976), despite numerous criticisms (e.g. Ceplecha, 1966).

Rather than using observations (from which many parameters need to be assumed due to lack of knowledge), some researchers proposed recreating meteoroid ablation in a laboratory. Small conducting particles are charged and accelerated, and detectors measure the speed, mass, radius, and charge. Particles with undesirable parameters are discarded, and the remaining particles enter a differential pumping system which leads to a gas filled chamber held at some pressure, depending on the experiment, in which the particles ablate. Many experiments were completed in the sixties and seventies (Slattery & Friichtenicht, 1967; Friichtenicht et al., 1968; Becker & Friichtenicht, 1971) using submicron-sized particles that ablated in gaseous targets. The particles were able to reach speeds of up to 50 km/s (Becker & Friichtenicht, 1971). A main difficulty with reproducing meteoroid ablation in a lab is being able to accurately reproduce atmospheric compositions and conditions – faint meteors ablate under free-molecular flow conditions, in which the molecular mean free path is much larger than the dimensions of the body. Another limitation that older studies encountered was the inability to reach meteor speeds greater than 50 km/s; however, modern studies are able to cover speeds between 1 - 100 km/s (Thomas et al., 2016). These experiments provide a method for studying meteors without having to wait for them to occur naturally, and with the prior knowledge of their mass, composition, and speed. However, these submicron-sized particles typically consisted of a single element (copper, iron, magnesium, silicon, aluminium), ablating in gases that were not necessarily accurate representations of the true atmosphere. Another similar method of studying the luminous efficiency, that eliminates the uncertainty of atmospheric conditions, is to use artificial meteoroids. Objects of known mass and composition are launched on rockets into the atmosphere where they are fired back at Earth and observed as they ablate. Ayers et al. (1970) studied iron and nickel projectiles, materials which were chosen due to their presence in many meteor spectra. The artificial meteoroids were shaped as either cones or disks, with masses between 0.64 and 5.66 g. The observed brightness and speeds, combined with the known masses, allowed the authors to determine the luminous efficiency of each object using Equation 1.13. Combining their results with those of Friichtenicht et al. (1968), and another artificial iron

meteoroid study by McCrosky & Soberman (1963), Ayers et al. (1970) produced a best guess curve for iron meteors, which they extended to meteoroids with stony compositions, assuming most of the light from the latter comes from iron lines. A modified result from Ayers et al. (1970) was used by Ceplecha & McCrosky (1976) to study fireballs.

A comparison of simultaneous radar and optical observations of meteors has been used to determine the luminous efficiency by both Saidov & Simek (1989) and Weryk & Brown (2013). By combining the ionisation equation (discussed below) with the simplified luminous intensity equation, it is possible to determine the luminous efficiency with parameters that are measurable from simultaneous radar/optical observations. The only term that needs to be assumed is the ionisation coefficient. The advantage to using this method is that all atoms produce detectable electrons; not all atoms produce visible light in the bandpass of a given detector.

As a meteoroid ablates in the atmosphere, the collisions between atmospheric atoms and vaporised meteoritic atoms leave a trail of ionised atoms in its wake. Radio waves can reflect off this trail of ionisation, providing information about the meteoroid. Meteor theory proposes that the amount of ionisation produced, q , is proportional to the rate of mass loss, as given in Equation 1.22

$$q = -\frac{\beta}{\mu v} \frac{dm}{dt} \quad (1.22)$$

where q is the electron line density (that is, the ionisation produced per metre along the trajectory), β is the ionisation coefficient, representing the average number of electrons produced during a collision, μ is the atomic mass of a meteoritic atom, and v is the meteor speed.

Combining Equation 1.22 and the simplified version of Equation 1.19 allows the luminous efficiency to be determined from simultaneous radar and optical observations, given an estimate for β . This is the approach taken by both Saidov & Simek (1989) and Weryk & Brown (2013). The study by Saidov & Simek used simultaneous radar, visual, and telescopic observations taken in 1972 and 1973 by Znojil et al. (1985) to determine the luminous efficiency. A similar approach was taken by Weryk & Brown (2013) using the Canadian Meteor Orbit

Radar (and several optical systems including the Canadian Automated Meteor Observatory). A simple ratio of the ionisation and luminous efficiencies can be determined based on measurable quantities (shown in Equation 1.23). Jones (1997) used a combination of theory and observations to determine an expression for β , which was used by Weryk & Brown (2013) to determine the luminous efficiency.

$$\frac{\beta}{\tau} = \frac{\mu v^3 q}{2I} \quad (1.23)$$

Figure 1.5 shows some of the luminous efficiency studies mentioned above. However, it is important to note that each study is unique and it is difficult to directly compare the results for luminous efficiency. Each study is specific to a certain bandpass (since luminous efficiency depends on the spectral range of the system used to observe the meteors); some studies require non-fragmenting meteoroids, such as Verniani (1965), but technology at the time made it difficult to ensure that was the case and corrections needed to be made (which were not necessarily correct); some studies used meteoroids that may have fragmented, which did not affect their results (e.g. artificial meteoroid studies used the known mass, or simultaneous radar/optical studies); in-lab studies were completed for specific individual elemental particles, and meteor spectra show a range of elements.

1.4 Meteor observations

1.4.1 Visual

Visual observation of meteors is the oldest method for studying meteors, but is useful only for certain particular measurements due to the lack of accuracy. Visual observations can be done without any equipment, and experienced observers can record approximate meteor radiant, magnitudes, and duration. While visual observations are uncommon today in scientific studies, visual activity curves for meteor showers are sometimes used due to the large number of consistent observations over a range of longitudes, and visual observations are valuable

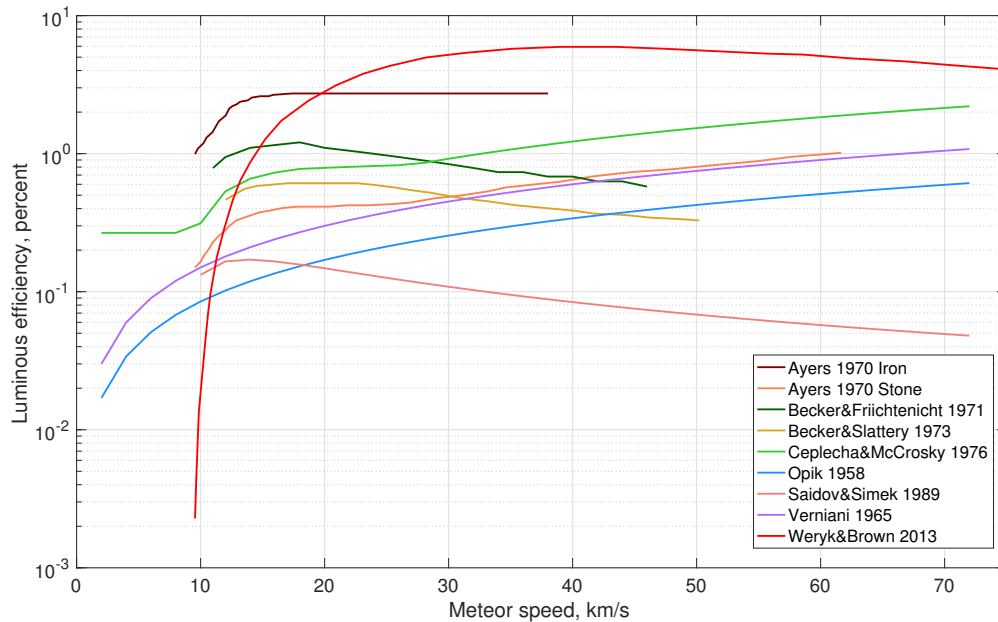


Figure 1.5: Past studies of luminous efficiency as a function of speed.

when meteor networks fail to capture meteor events. Moser (2017) found that visual meteor observations are reliable when at least 75 eyewitness curves are reported.

1.4.2 Photographic

Photographic meteor observations have been used since 1885 (Ceplecha et al., 1998), and because photographic plates typically have very high resolution (slightly better than typical video systems today), meteoroid orbits, structure, and physical properties have been studied in the past using this technique. Rotating shutters allowed Whipple (1938) to study meteor speeds, decelerations, radiants, heights, and velocities. A major study conducted at the Ondřejov Observatory in Czechoslovakia in the 1950s was the first to photograph a recovered fireball, and was the motivation for other photographic fireball networks (Ceplecha et al., 1998). Super-Schmidt cameras were used in the early 1950s at Harvard, and detailed studies of 413 very precisely recorded meteors were completed (Jacchia & Whipple, 1961; Ceplecha, 1967). The Harvard Super-Schmidt cameras were able to observe down to +3 magnitude, and showed

many anomalies relative to brighter meteors, such as shorter ablation durations; meteors that decelerate faster than theory predicts; and light curves that increase suddenly at the onset of visible ablation. These observations led to the proposal of progressive fragmentation (Jachia, 1955), which describes meteoroids as porous and fragile objects. Further evidence for fragmentation led to the dustball model, put forth by (Hawkes & Jones, 1975).

1.4.3 Video

Video observations have greater timing resolution compared to photographic observations, and the addition of image intensifiers to video systems allows much fainter objects to be observed. Multi-camera image-intensified video systems are commonly used today, and are able to collect meteor light curves, orbits, and fluxes – useful information for determining meteoroid structure, physical properties, and when considering shielding for satellites and spacecraft. Personal video cameras have been found to be quite useful, specifically in the study of the Chelyabinsk fireball – personal videos such as dashcams and security cameras were used to determine the orbit and trajectory of this large daytime bolide (Borovička et al., 2013). Orbits can be determined from two-station video camera systems, as described in Figure 1.6: the observed meteor start and end positions combined with the camera position define a plane, for each camera station. The line of intersection for the two planes is the trajectory of the meteoroid, and can be used to determine the orbit of the object. Currently typical multi-station video systems can detect meteors down to $+6.5^M$ (Weryk et al., 2013), however with modifications some systems can get down to $+9^M$.

1.4.4 Spectral

Meteors emit light mostly in atomic emission lines (with a small portion coming from molecular bands and continuum radiation, and no more than 3% coming from atmospheric constituents) and by studying meteor spectroscopy, one can determine some elemental components of a meteoroid. Commonly identified species include iron, magnesium, sodium, calcium, and

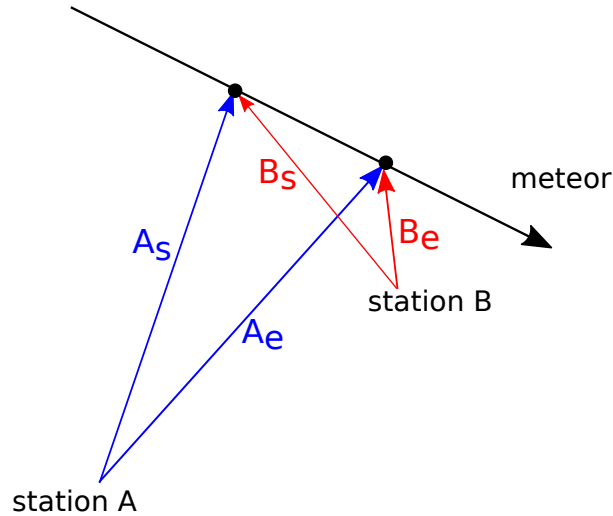


Figure 1.6: Two-station observations of meteors can be used to determine the trajectory of the object. Two observations from each station create two intersecting planes, with the line of intersection defining the meteoroid trajectory. The subscript S refers to the initial observation and E refers to the final observation.

silicon (Bronshten, 1983). An example of a meteor spectrum is shown in Figure 1.7. The classical ablation model assumes that the meteoroid ablates uniformly as a self similar object; however, meteor spectra have shown that differential ablation occurs frequently (e.g. Borovika, 2005; Bloxam & Campbell-Brown, 2017), and that more volatile atoms (e.g. sodium) ablate earlier than the more refractory ones (e.g. calcium)⁹. Meteor spectroscopy studies can model line emissions to determine the ratio of one element to another, but is difficult to do as ionisation and excitation conditions need to be known, and for simplicity, thermal equilibrium is assumed¹⁰.

1.5 Thesis Goals

The primary goal of this thesis is to use high-resolution optical observations to determine (or better constrain) physical properties of faint meteors. A better understanding of meteoroid

⁹Differential ablation can cause non-classical light curve shapes without fragmentation, if the meteoroid is not homogeneous. The volatile components will ablate quickly, while the more refractory components will ablate at a slower rate.

¹⁰Thermal equilibrium is unlikely since at meteor heights the atmospheric temperature is much less than that of the meteoritic material. The atmospheric density is also low which makes it difficult to quantify a temperature.

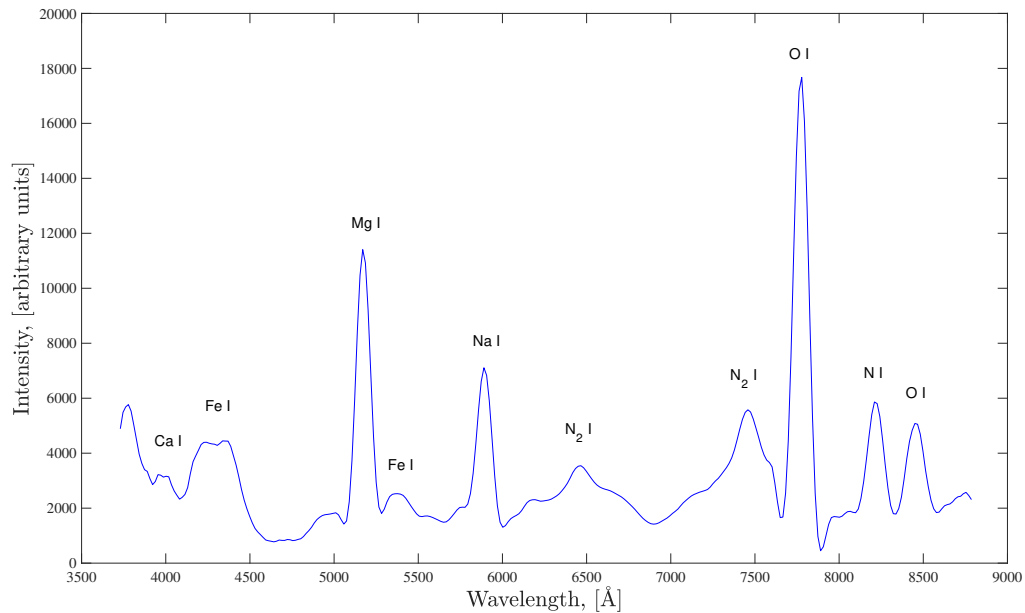


Figure 1.7: Meteor spectrum of a Geminid, corrected for the spectral response of the detector, with some prominent lines labelled. Figure adapted from Vojáček et al. (2015). The spectrum consists of the continuum, and lines from both the heated atmosphere and evaporated meteoritic material.

properties provides information about the small bodies in our Solar system, and can be used to protect spacecraft and satellites with regards to shielding.

The specific goals of this work are to examine current ideas of meteor behaviour with different observations to determine which are valid, and to determine meteor luminous efficiency values in a more thorough manner than has previously been attempted.

Chapter 3 (published as Subasinghe et al. (2016)) combines high-resolution narrow-field observations with more typical wide-field observations to investigate meteoroid strength, origin, and structure. Chapter 4 (published as Subasinghe et al. (2017)) investigates meteor luminous efficiency, in particular, the uncertainty associated with equating the dynamic and photometric meteoroid masses to determine luminous efficiency for meteors observed with the Canadian Automated Meteor Observatory (which will be discussed in Chapter 2). Chapter 5 extends that work by applying that method to fifteen observed non-fragmenting meteor events. This is the first study to use photometric and dynamic masses with modern high-resolution

observations. This thesis work is summarised in Chapter 6 and future work is discussed.

Bibliography

- Ayers, W. G., McCrosky, R. E., & Shao, C.-Y. 1970, SAO Special Report, 317
- Becker, D. G., & Friichtenicht, J. F. 1971, *Astrophysical Journal*, 166, 699
- Bellot Rubio, L. R., Martínez González, M. J., Ruiz Herrera, L., et al. 2002, *Astronomy and Astrophysics*, 389, 680
- Bloxam, K., & Campbell-Brown, M. 2017, *Planetary and Space Science*, 143, 28
- Borovička, J., Spurný, P., Brown, P., et al. 2013, *Nature*, 503, 235
- Borovička, J., Spurný, P., & Koten, P. 2007, *Astronomy and Astrophysics*, 473, 661
- Borovika, J. 2005, *Proceedings of the International Astronomical Union*, 1, 249271
- Bronshten, V. A. 1983, *Physics of meteoric phenomena*
- Brownlee, D., Tsou, P., Aléon, J., et al. 2006, *Science*, 314, 1711
- Campbell-Brown, M. 2007, *Dust in Planetary Systems*, 643, 11
- Campbell-Brown, M. D., Borovička, J., Brown, P. G., & Stokan, E. 2013, *Astronomy and Astrophysics*, 557, A41
- Campbell-Brown, M. D., & Koschny, D. 2004, *Astronomy and Astrophysics*, 418, 751
- Caswell, R. D., McBride, N., & Taylor, A. D. 1995, *International Journal of Impact Engineering*, 17, 139
- Ceplecha, Z. 1958, *Bulletin of the Astronomical Institutes of Czechoslovakia*, 9, 154
- . 1966, *Bulletin of the Astronomical Institutes of Czechoslovakia*, 17, 347
- . 1967, *Smithsonian Contributions to Astrophysics*, 11, 35

- . 1988, *Bulletin of the Astronomical Institutes of Czechoslovakia*, 39, 221
- Ceplecha, Z., Borovička, J., Elford, W. G., et al. 1998, *Space Science Reviews*, 84, 327
- Ceplecha, Z., & McCrosky, R. E. 1976, *Journal of Geophysical Research*, 81, 6257
- Cook, A. F., Jacchia, L. G., & McCrosky, R. E. 1963, *Smithsonian Contributions to Astrophysics*, 7, 209
- de Pater, I., & Lissauer, J. J. 2010, *Planetary Sciences*
- Fleming, D. E. B., Hawkes, R. L., & Jones, J. 1993, in *Meteoroids and their Parent Bodies*, ed. J. Stohl & I. P. Williams, 261
- Friichtenicht, J. F., Slattery, J. C., & Tagliaferri, E. 1968, *Astrophysical Journal*, 151, 747
- Fulle, M., Della Corte, V., Rotundi, A., et al. 2015, *The Astrophysical Journal Letters*, 802, L12
- Hawkes, R. L., & Jones, J. 1975, *Monthly Notices of the Royal Astronomical Society*, 173, 339
- Hilchenbach, M., Kissel, J., Langevin, Y., et al. 2016, *The Astrophysical Journal Letters*, 816, L32
- Jacchia, L. G. 1955, *Astrophysical Journal*, 121, 521
- Jacchia, L. G., & Whipple, F. L. 1956, *Vistas in Astronomy*, 2, 982
- . 1961, *Smithsonian Contributions to Astrophysics*, 4, 97
- Jones, W. 1997, *Monthly Notices of the Royal Astronomical Society of Canada*, 288, 995
- Kikwaya, J.-B., Campbell-Brown, M., & Brown, P. G. 2011, *Astronomy & Astrophysics*, 530, A113

- Koten, P., & Borovička, J. 2001, in ESA Special Publication, Vol. 495, Meteoroids 2001 Conference, ed. B. Warmbein, 259–264
- McCrosky, R. E., & Soberman, R. K. 1963, *Smithsonian Contributions to Astrophysics*, 7, 199
- McKinley, D. W. R. 1961, *Meteor science and engineering*.
- Moser, D. E. 2017, *Planetary and Space Science*, 143, 182
- Murray, I. S., Hawkes, R. L., & Jenniskens, P. 1999, *Meteoritics and Planetary Science*, 34, 949
- Nakamura, T., Noguchi, T., Tanaka, M., et al. 2011, *Science*, 333, 1113
- Öpik, E. 1933, *Atomic Collisions and Radiation of Meteors* (Harvard Reprint No 100, Harvard College Observatory), reprinted from *Acta et Commentationes Univ. Tartuensis (Dorpatensis)* A26, Pt 2
- . 1955, *Proceedings of the Royal Society of London. Series A, Mathematical and Physical Sciences*, 230, 463. <http://www.jstor.org/stable/99792>
- Rotundi, A., Sierks, H., Della Corte, V., et al. 2015, *Science*, 347, aaa3905
- Saidov, K. H., & Simek, M. 1989, *Bulletin of the Astronomical Institutes of Czechoslovakia*, 40, 330
- Slattery, J. C., & Friichtenicht, J. F. 1967, *Astrophysical Journal*, 147, 235
- Subasinghe, D., Campbell-Brown, M. D., & Stokan, E. 2016, *Monthly Notices of the Royal Astronomical Society*, 457, 1289
- . 2017, *Planetary and Space Science*, 143, 71
- Thomas, E., Horányi, M., Janches, D., et al. 2016, *Geophysical Research Letters*, 43, 3645
- Thomas, R. N., & Whipple, F. L. 1951, *Astrophysical Journal*, 114, 448

- Vaubailion, J., Kolen, P., Margonis, A., et al. 2015, *Earth Moon and Planets*, 114, 137
- Verniani, F. 1965, *Smithsonian Contributions to Astrophysics*, 8, 141
- Vojáček, V., Borovička, J., Kolen, P., Spurný, P., & Štork, R. 2015, *Astronomy and Astrophysics*, 580, A67
- Weryk, R. J., & Brown, P. G. 2013, *Planetary and Space Science*, 81, 32
- Weryk, R. J., Campbell-Brown, M. D., Wiegert, P. A., et al. 2013, *Icarus*, 225, 614
- Whipple, F. L. 1938, *Proceedings of the American Philosophical Society*, 79, 499. <http://www.jstor.org/stable/984939>
- Whipple, F. L. 1950, *Astrophysical Journal*, 111, 375
- . 1951, *Astrophysical Journal*, 113, 464
- Znojil, V., Hollan, J., & Simek, M. 1985, *Bulletin of the Astronomical Institutes of Czechoslovakia*, 36, 44

Chapter 2

Equipment and Data Reduction

2.1 The Canadian Automated Meteor Observatory

The Canadian Automated Meteor Observatory (CAMO) is a two-station, image-intensified video system used for faint meteor studies. This is a fully automated system that operates under certain conditions (Moon position, cloud cover, and weather are taken into account). The CAMO guided system is able to observe meteors at resolutions up to 3 metres per pixel at a range of 100 km, from which meteor fragmentation behaviour can be determined. The two-station system means that meteor orbits can be determined, as shown in Figure 1.6.

One of the two stations is located in Tavistock, Ontario, Canada (43.265°N , 80.772°W), and the other is approximately 45 km away in Elginfield, Ontario, Canada (43.193°N , 81.316°W), with their locations shown in Figure 2.1. Complete details of the system can be found in Weryk et al. (2013).

The CAMO guided system was used for all parts of this work. The guided system consists of two cameras at each station: a wide-field camera (28° field of view), and a narrow-field camera (1.5° field of view); the cameras are identical at the two-stations. The objective lens of the narrow-field camera is a refracting telescope, which provides high-resolution observations. The detection and tracking software used (described below) determines if a meteor is in the



Figure 2.1: Map from Google showing southern Ontario, Canada, with the locations of the Elginfield and Tavistock stations indicated.

wide-field field of view, and if so, will direct the meteor light with a pair of mirrors into the narrow-field camera. Details of the wide and narrow-field cameras are given in Table 2.1. An example of the resolution obtained with the CAMO guided system is shown in Figure 2.2.

The CAMO system has image intensifiers which allow fainter meteors to be observed. As mentioned in Section 1.3, luminous efficiency studies depend on the bandpass of the equipment used for the experiment or observations, and the spectral response of the intensifiers used with CAMO is shown in Figure 2.3, compared to Johnson-Cousins R, V, and I bands. This is the bandpass in which the results of Chapter 5 are calculated. Because the CAMO Gen III image intensifiers match the Johnson-Cousins R band best, all photometric calibrations (discussed below) are done in the R band.

The cameras are enclosed in a shed, with a roof that opens automatically under certain conditions. A weather station provides information about temperature, wind speed, and humidity. An image of the shed and cameras is shown in Figure 2.4a.

Table 2.1: Specifications of the CAMO guided system cameras. The wide-field observations are used for trajectories and meteor light curves. The narrow-field camera provides information on meteor fragmentation behaviour because of its high spatial resolution.

	Wide-field	Narrow-field
Field of View	28°	1.5°
Frame Rate	80 fps	100 fps
Limiting Stellar magnitude	+7.5	+7
Limiting Meteor magnitude	+5.5	<+5
Precision (at 100 km range)	71 m/pixel	3.2 m/pixel
Objective lens	25 mm f/0.85	545 mm f/11

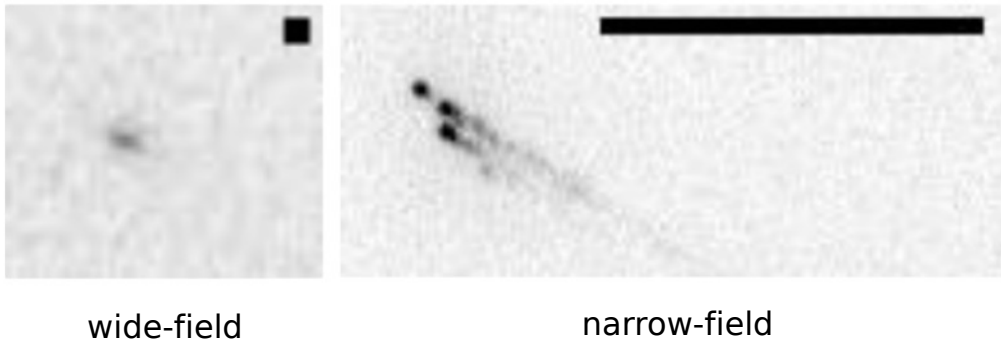


Figure 2.2: Two views of the same meteor taken at the same time as seen from the two cameras of the CAMO guided system. The scale bar in each frame is 250 metres, and the meteor is at a height of 85 km. The wide-field meteor image is smeared due to the motion of the meteor, while the narrow-field, which smoothly tracks the meteor, is not smeared. The images are inverted to show details.

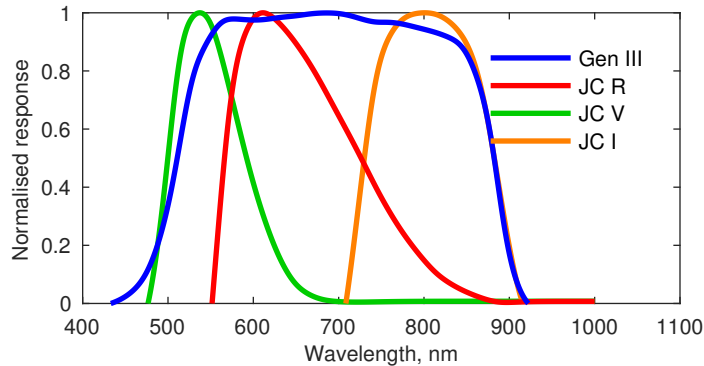
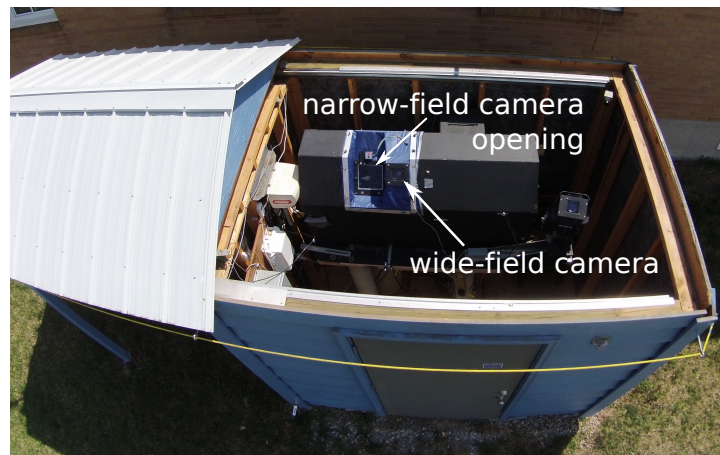
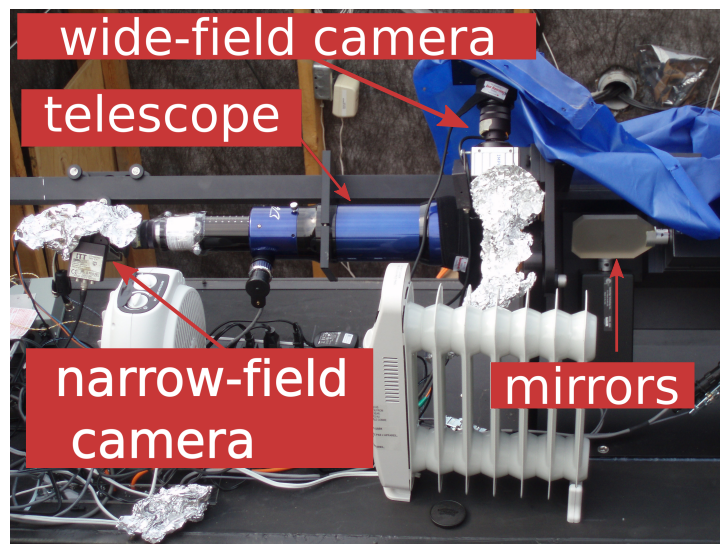


Figure 2.3: The spectral response of the Gen III image intensifiers used with CAMO compared to the Johnson-Cousins R, V, and I bands.



(a) The CAMO system at Elginfield seen inside the shed, with the retractable roof.



(b) The CAMO system seen without the cover. The telescope is a William Optics Zenithstar 80 II ED APO f/6.8 refractor. The mirrors reduce the aperture (from 80 mm to 50 mm) giving the narrow-field camera an effective focal ratio of f/11.

Figure 2.4: The CAMO guided system.

2.2 ASGARD

The software used to detect meteors in real time in the wide-field camera is called ASGARD (All Sky and Guided Automatic Realtime Detection) (Weryk et al., 2008). The software compares frames by going through each pixel and finding where the intensity exceeds five standard deviations above the mean background. At least six pixels in an 8 X 8 pixel region greater than the set threshold is considered a meteor, as long as this occurs in at least 3 consecutive frames. Weryk et al. (2013) found that a 5σ threshold detects 67% of meteors. Lowering this threshold will increase the number of meteors detected, however fainter meteors will not be well tracked in that case. If a meteor is detected, galvanometers will move two orthogonal mirrors such that they direct meteor light into the telescope attached to the narrow-field camera. Most meteors are tracked smoothly, since the galvanometers are updated at 2000 Hz and have a slew rate of 2000° per second. The entire meteoroid ablation profile may be fully captured in the wide-field camera, but is not fully captured in the narrow-field camera: it takes between 4 - 7 frames of observation in the wide-field camera before the mirrors are focused on the meteor in the narrow-field camera, and it typically takes a few frames before the meteor is tracked smoothly. Generally, once the meteor is being tracked in the narrow-field camera, the meteor appears stationary.

Meteor events recorded with the wide-field camera are automatically reduced using ASGARD, which provides a meteor trajectory (and orbit), and a light curve. A user will pick a minimum of 10 stars (typically 20 or more are selected), which will determine the *astrometric* and *photometric plates*. The stellar positions and brightnesses are calibrated against those from the Sky2000v4 catalogue (Myers et al., 2001). A flat needs to be applied to the frames before the photometric plate can be computed. The flat is computed by taking the median value for each pixel from a stack of frames recorded over the night. This will correct for differences in pixel sensitivity over the field of view and vignetting in the lens. The flat is only background and does not include stars as they move during the night. The photometric offset is determined by fitting a line between the instrumental magnitude and the R-band magnitude, setting the

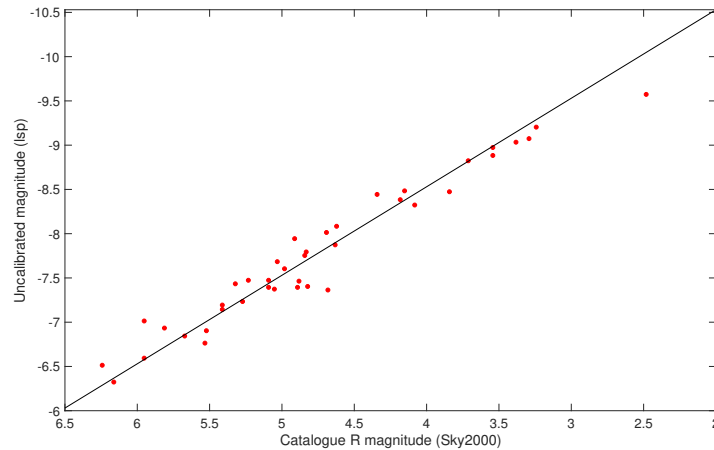


Figure 2.5: The photometric plate for the Elginfield wide-field camera on March 29, 2017. The photometric offset is the intercept of the line and is -12.53 ± 0.10 . Forty stars of various stellar types are plotted here

slope to one, as shown in Figure 2.5.

The intercept is the photometric offset and is used to convert between the two magnitudes. The photometric plate then allows meteor photometry to be calibrated against the stellar photometry. The astrometric plate is created by selecting stars in the wide-field camera (giving the (x,y) pixel location) and calibrating against the positions of those stars in the catalogue. The celestial coordinates of the stars from the catalogue are converted to local zenith and azimuth coordinates (θ, ϕ) . These celestial coordinates are projected onto a flat plane which represents the field of view of each station, and the projected pixel coordinates (p,q) can be compared to the manually selected positions (x,y) . A third order polynomial fit is used to convert between the projected coordinates and the manually selected coordinates.

The pixel location of the meteor is selected automatically through centroiding, but the software may make errors due to transient bright pixels, or nearby stars. ASGARD determines the meteor trajectory with a program called MILIG (Borovicka, 1990), which uses the least squares method. For the photometric analysis, any pixels above the background threshold in the group of pixels that make up the meteor are masked out. Those pixels are used to calculate the log of the sum of the meteor pixel brightness, which can be converted into an apparent

meteor brightness using the photometric offset, and then converted to an absolute meteor magnitude using the range to the meteor. The uncertainty in the photometry for these automated reductions is around 0.5 mag (Subasinghe et al., 2016). More refined meteor trajectories and light curves can be obtained through manual reductions, but the automated reductions provide a large survey of meteor events for analysis.

2.3 METAL

Wide-field meteor events can be reduced manually with a program called METAL (METeor AnaLysis) (Weryk & Brown, 2012). Rather than common astrometric and photometric plates being used for all events, plates are made by the user for each meteor being studied. The user picks a minimum of 10 stars for calibration against the Sky2000v4 catalogue (Myers et al., 2001) (which are used to create photometric and astrometric plates), and then picks the head of the meteor in each frame for both stations. From these position picks, the meteor trajectory is determined using MILIG. Meteor photometry can be determined by masking out pixels containing meteor light and taking the log of the sum of the pixels. This gives the apparent meteor magnitude, which can be converted to an absolute meteor magnitude using Equation 1.4.

2.4 mirfit

Narrow-field meteor observations can be analysed in a software program called mirfit. Unlike METAL, photometric and astrometric plates cannot be made in mirfit due to the small field of view. The field of view for the narrow-field camera is also moving as observations are collected, and this movement needs to be considered when determining the meteor position. The mirror positions (h_x, h_y) are recorded every 0.5 ms. The offset between the centre of the narrow-field image and the position of the meteor is converted into an offset in mirror encoder coordinates $(\Delta h_x, \Delta h_y)$: this quantifies how much the mirrors should be moved such that the meteor is in

the centre of the field of view. A change of 3 mirror encoder units will shift the narrow-field image by 1 pixel. This offset is then added to the mirror position, which is mapped to celestial coordinates (θ, ϕ) . Determining the offset from the centre of the image is done with a scale plate. Every two hours the mirrors are pointed at stars to update the calibration. This can also be calibrated by deliberately moving the stars off the centre of the field of view. The mirror encoder coordinates are transformed to celestial coordinates using what is called an exact plate.

When analysing a meteor event in mirfit, the user makes selections for the position of the meteor (centroiding works well for non-fragmenting meteors). As in METAL, bright pixels due to the luminosity of the meteor can be masked out to determine the meteor photometry. The narrow-field meteor photometry can be determined by comparing the stellar calibrated wide-field meteor photometry with the narrow-field apparent meteor magnitude.

2.5 Determining Luminous Efficiency

In this thesis, the luminous efficiency of meteors was determined by equating the dynamic and photometric masses, which were each calculated using the classical ablation equations. This method requires meteors that do not fragment. The selected meteors were reduced in both METAL and mirfit to obtain orbital information, photometric information, and in particular, high-precision position measurements from mirfit. The deceleration and intensity equations (given in Equations 1.17 and 1.19) require deceleration values to calculate their respective masses. The precise position measurements can be converted to lag measurements (how far a meteoroid falls behind an object travelling at a constant speed), and the second derivative of this lag gives the deceleration. Despite the high precision provided by the narrow-field cameras, taking two derivatives (through finite differencing) introduces significant noise. Different functional fits were tested by Subasinghe et al. (2017) on simulated meteor data and a two-term exponential fit to the simulated meteor lag was found to provide reasonably good results. Because the atmospheric density decreases exponentially with increasing height, an exponential

function is most meaningful, with a higher order fitting the data better (but not necessarily providing a more physical model). Because real meteor data is noisy (unlike the simulated data used in Subasinghe et al. (2017)), a simplification was made in Subasinghe & Campbell-Brown (2017) to a single-term exponential function. From the fit parameters a meteoroid deceleration profile can be found. The meteoroid photometry (from mirfit, but calibrated with METAL meteoroid photometry, described below), atmospheric density profile (from NRLMSISE-00 (Picone et al., 2002)), and speed and deceleration profiles based on the fit parameters, combined with best guess values for other parameters (drag coefficient; shape factor; meteoroid density), allow the luminous efficiency to be calculated for a meteoroid.

The meteoroid photometry can be determined in mirfit; however, as no photometric plate is made for mirfit, the meteoroid photometry cannot be calibrated against stars observed in the narrow-field camera. The narrow-field observations show very few stars, making it difficult to do a direct comparison, the way ASGARD does in METAL. To calibrate the photometry in mirfit, pixels are masked out, and the log of the sum of pixel (lsp) brightness is calculated, which is the instrumental apparent brightness. By comparing these lsp values with the absolute magnitude of the meteor determined in METAL, a correction can be found to determine the absolute meteor magnitude in the narrow-field camera. For meteors that showed a leading fragment (a piece of a meteor that has separated from the main body and shows little to no fragmentation: see Figure 5.4a for an example), the photometry calibration has an extra step – the first step calibrates the METAL photometry with the entire meteoroid observed in mirfit, and the second uses that calibration offset on the photometry of just the leading fragment observed in mirfit. This provides the photometry of only the relevant part of the meteoroid. For meteoroids that show single-body ablation (see Figure 5.4b), only the first step is required for calibrating the meteoroid photometry.

Despite the low number of visible stars in the narrow-field camera field of view, it is possible to use those stars to calibrate the meteoroid photometry. The average instrumental apparent magnitude needs to be determined for each visible star. The offset from the Sky2000v4 cat-

alogue (Myers et al., 2001) R magnitude can be added to the instrumental apparent meteor magnitude to correct the values to apparent meteor magnitudes. Using the range of the meteor to the observing station, the absolute meteor magnitude can be determined. An analysis of meteor photometry based on wide-field stellar photometry compared to narrow-field stellar photometry was done in Subasinghe & Campbell-Brown (2017): the average difference between the determined meteor magnitude calculated using the narrow-field and wide-field visible stars was found to be -0.3098 and -0.2666 magnitude, for Tavistock and Elginfield respectively.

Bibliography

- Borovicka, J. 1990, *Bulletin of the Astronomical Institutes of Czechoslovakia*, 41, 391
- Myers, J. R., Sande, C. B., Miller, A. C., Warren, Jr., W. H., & Tracewell, D. A. 2001, *VizieR Online Data Catalog*, 5109
- Picone, J. M., Hedin, A. E., Drob, D. P., & Aikin, A. C. 2002, *Journal of Geophysical Research: Space Physics*, 107, doi:10.1029/2002JA009430
- Subasinghe, D., & Campbell-Brown, M. D. 2017, *Astronomical Journal*, in press
- Subasinghe, D., Campbell-Brown, M. D., & Stokan, E. 2016, *Monthly Notices of the Royal Astronomical Society*, 457, 1289
- . 2017, *Planetary and Space Science*, 143, 71
- Weryk, R. J., & Brown, P. G. 2012, *Planetary and Space Science*, 62, 132
- Weryk, R. J., Brown, P. G., Domokos, A., et al. 2008, *Earth Moon and Planets*, 102, 241
- Weryk, R. J., Campbell-Brown, M. D., Wiegert, P. A., et al. 2013, *Icarus*, 225, 614

Chapter 3

Classifying Meteors

A version of this chapter has been published as:

Subasinghe, D; Campbell-Brown, M.D., & Stokan, E. (2016). *Physical characteristics of faint meteors by light curve and high-resolution observations, and the implications for parent bodies*. Monthly Notices of the Royal Astronomical Society, 457, 1289

3.1 Introduction

Characterising the meteoroids that impact the Earth each day is of the utmost importance for spacecraft, satellites, and life on Earth. While most of these bodies are too small to survive ablation and reach the ground, objects in the millimetre to centimetre size range are capable of damaging satellites (Drolshagen, 2008). These faint meteors [masses between 10^{-7} and 10^{-4} kg, based on luminous efficiency values from Weryk & Brown (2013)] may be studied as they ablate in the atmosphere, and understanding their physical properties helps us understand those of their parent bodies: asteroids and comets.

Determining the physical properties of meteoroids is useful. In a practical sense, estimates of meteoroid penetration and spacecraft damage may be improved by determining more ac-

curate values of meteoroid density and structure. Scientifically, differences between asteroids and comets can be deduced by observing how meteoroids from each parent body ablate and fragment in the atmosphere. Current models of Solar system formation suggest that asteroids and comets should differ significantly in their fundamental composition and constituents due to their formation at different distances from the Sun; in particular, comets should be lacking in refractory elements which condensed into particles at high temperatures in the inner Solar system. Calling this into question, in 2004, the Stardust probe flew by comet Wild 2 and collected thousands of particles containing refractory material believed to have formed in the inner Solar system (Brownlee et al., 2006). These observations suggested similarities in composition between asteroids and comets, and large scale mixing in the solar nebula. The Stardust mission collected samples between 1 and 300 μm in size: no millimetre-sized particles from comets or asteroids have ever been collected, apart from meteorites. Additionally, the presence of large refractory meteorite components such as chondrules and calcium-aluminium inclusions in comets, which are too large to have been collected during the Stardust mission, are of interest to Solar system formation modellers. For these reasons, observing faint meteors and modelling their ablation are important for studying the composition and structure of cometary and asteroidal particles in this size range.

Meteoroid ablation models vary, but are based on the same assumptions: energy and momentum are conserved, and the observed brightness is proportional to the lost kinetic energy. There are up to four equations that make up the classical model: the deceleration equation, which describes the momentum transferred from the meteor to the intercepted air column; the mass loss equation, which describes the energy needed to ablate the meteoroid; the luminosity equation, which describes the energy used to produce visible light; and the temperature equation, which is based on conservation of energy. These equations have many coefficients and make various assumptions. Three important coefficients are the drag coefficient, which describes what fraction of the meteoroid's momentum is transferred to the air column; the heat transfer coefficient, which describes what fraction of kinetic energy is used for ablating the

meteoroid; and the luminous efficiency, which is the fraction of kinetic energy which produces light. The meteoroid is assumed to be spherical and uniform in composition; and the object is a solid, single body that is non-fragmenting. As the meteoroid descends, interactions between it and the exponentially thickening atmosphere heat it up and result in a late-peaked light curve (the variation in observed brightness as a function of time). This is often called a classical light curve.

The relative position of the maximum brightness of a meteor during ablation can be described by the F parameter, by which single peaked light curves are often classified (Fleming et al., 1993). The F parameter (which ranges from 0 to 1) describes the ratio of the position of maximum brightness to the length of the entire light curve, and is expressed as:

$$F = \frac{h_{\text{beg}} - h_{\text{max}}}{h_{\text{beg}} - h_{\text{end}}} \quad (3.1)$$

where h_{beg} is the beginning height, h_{max} is the height at which the maximum brightness occurs, and h_{end} is the end height of the light curve. The beginning and ending heights are related to the meteor limiting magnitude of the system used. For this work, this value is +5 mag. An F parameter value of 0.5 corresponds to a symmetric light curve; a value less than 0.5 describes an early peaked light curve; and a value greater than 0.5 is associated with a late-peaked light curve (classical light curves are late peaked by definition, but non classical models are also able to produce late-peaked curves).

The classical, non-fragmenting ablation model was accepted for lack of evidence to the contrary until Jacchia (1955) noted that the model did not agree with the behaviour of faint meteors observed with Super-Schmidt cameras. He found that the photometric masses of faint meteors (calculated from the light they produce) were much larger than the dynamic masses (determined by deceleration), and concluded that faint meteors fragment during their descent through the atmosphere. He also found that many of the faint light curves had their peak brightness near the beginning of the trajectory, and the length of the light curves (i.e. the

difference between the beginning and ending height) tended to be smaller than predicted by classical ablation theory. The classical light curve shape (a steady rise to a maximum brightness followed by a steep drop) is not typical of faint meteors, which show a wide variety of light curve shapes (Fleming et al., 1993; Murray et al., 1999; Koten & Borovička, 2001; Beech & Murray, 2003). Within a single meteor shower different light curve shapes have been measured, and year to year differences in meteor shower families can also be seen (Murray et al., 2000). A study by Faloon et al. (2004) found no statistically significant differences in the F parameter between shower and sporadic meteor light curves, suggesting similar structures for the two groups of meteors. Similarly, Koten & Borovička (2001) found meteor light curves to have, on average, symmetric shapes, and large variation within individual meteor showers.

Fragmentation and the quantitative dustball model presented by Hawkes & Jones (1975) are able to explain the anomalous features observed in faint meteor light curves. The dustball model suggests that meteoroids are comprised of grains with a high boiling point held together by a material (a ‘glue’) with a lower boiling point. When the boiling temperature of the glue is reached during ablation, the glue is vaporised and the stony or metallic grains being held together are released. Once they reach their boiling temperature, each grain ablates classically, and the light produced is assumed to be the summed light production from each grain. The glue does not contribute to the observed brightness. This model suggests that small (millimetre-sized) meteoroids will have approximately constant begin, end, and maximum brightness heights, with respect to mass. The heights are set by the physical properties chosen for the grains. The dustball model has been used as the basis of recent numerical meteoroid ablation models somewhat successfully (Campbell-Brown & Koschny, 2004; Borovička et al., 2007). The models by Campbell-Brown & Koschny (2004) and Borovička et al. (2007) were able to reproduce meteor light curves and observed decelerations (using two different fragmentation methods), but neither was able to simultaneously reproduce the high-resolution behaviour of the meteoroids. Both models predicted longer and brighter wakes than observed with the high-resolution (metre scale) cameras (Campbell-Brown et al., 2013). A shorter or

fainter predicted wake would be acceptable and the difference between observed and predicted wake may be explained through light emission by atoms in the trail. These high-resolution observations represent a new constraint for modellers and a new source of information on meteoroids.

Some meteors can be linked to specific parent bodies (shower meteors), but most meteors are sporadic (Wiegert et al., 2009) and their parent bodies are unknown. These sporadic meteors can be linked to classes of parent bodies using the Tisserand parameter, which can be used to determine whether an orbit is consistent with that of an asteroid or comet. The Tisserand parameter is typically calculated with respect to Jupiter and derived from the restricted 3 body problem, in which it is invariant. The assumptions made with this parameter are: the Sun and Jupiter travel on circular orbits about their common center of mass; the meteoroid's orbit is only affected by perturbations from Jupiter; and the mass of the meteoroid is negligible compared to Jupiter. In this case, the Tisserand parameter will remain constant even after perturbations from Jupiter, which allows meteoroids to be associated with asteroidal (main belt) or cometary parent bodies. The Tisserand parameter is given by Equation 3.2, where the variables a , e , i are the semi-major axis, eccentricity, and inclination of the meteoroid, and a_J is the semi-major axis of Jupiter.

$$T_J = \frac{a_J}{a} + 2 \left[(1 - e^2) \frac{a}{a_J} \right]^{1/2} \cos(i) \quad (3.2)$$

If $T_J \leq 2$, the meteoroid had a Halley-type orbit. Values greater than 2, but less than or equal to 3 suggest meteoroids from Jupiter family comets, and Tisserand values greater than three are associated with asteroids. These boundaries are not absolute: objects on asteroidal orbits can show cometary features (e.g. comet Encke), and asteroidal objects can have cometary Tisserand values (e.g. near Earth objects). The Tisserand parameter can be changed by close encounters with any of the planets other than Jupiter, and by radiation forces, which are particularly important for millimetre-sized objects. Nevertheless, the Tisserand parameter can separate meteoroids into three broad origin groups: asteroids, Jupiter family comets, and

long period comets. For this work, we will be using the Tisserand parameter as a proxy for the origin of observed meteor events.

The structure of a meteoroid depends on the properties of the region of the Solar system in which it formed. Cometary meteoroids are porous, fragile objects, according to Whipple's icy-comet model (Whipple, 1950, 1951), and this is consistent with studies of cometary meteoroid density and strength. Borovička et al. (2007) found that the Draconids, a Jupiter family meteor shower, have low mechanical strength, between 5 - 20 kPa. Borovička (2007) reports bulk densities around 300 kg/m^3 for Jupiter family meteoroids (inferred from studies of the Draconids). He also reports that Halley-type meteoroids have densities around 800 kg/m^3 (inferred from studies of the Perseids and Leonids), which agrees with Kikwaya et al. (2011), who find densities between $360 - 1510 \text{ kg/m}^3$. Kikwaya et al. (2011) also find that asteroidal meteors have an average bulk density of 4700 kg/m^3 , and Borovička (2007) suggests strengths between 100 - 5000 kPa for the same class of meteoroids. The general trend from these data is that cometary meteoroids are soft, porous, fragile objects that crumble easily, while asteroidal meteoroids are stronger objects that do not fragment as readily.

The K_b parameter defined by Ceplecha (1958) is a classification based on meteoroid begin height, pre-atmospheric velocity, and entry angle. This parameter, given in Equation 3.3, assumes that all meteoroids will begin to be luminous at the same surface temperature, and so the meteoroid begin height will be strongly related to its composition.

$$K_b = \log \rho_b + 2.5 \log v_\infty - 0.5 \log \cos(z_R) \quad (3.3)$$

In Equation 3.3, ρ_b is the atmospheric density at the beginning of the luminous path; v_∞ is the pre-atmospheric velocity; and z_R is the zenithal angle of the radiant. Ceplecha (1988) used the K_b parameter to classify meteors into five main groups: asteroidal, A, B, C, and D. The groups refer to mm-cm sized meteoroids and are associated with different types of material, as described in Table 3.1. The K_b parameter cannot distinguish between the effects of density, fragmentation, and volatility.

Table 3.1: Classification and description of meteors according to their K_b parameter. The bulk density values are from Ceplecha (1988).

Group	K_b	Description	Bulk density (g/cm^3)
Asteroidal	> 8	ordinary chondrites	3.7
A	7.3 - 8	carbonaceous chondrites	2.0
B	7.1 - 7.3	dense cometary material	1.0
C	6.6 - 7.1	regular cometary material	0.75
D	< 6.6	weak cometary material	0.27

High-resolution video observations are able to provide strong constraints for meteoroid ablation models, which improves our understanding of both meteor-atmosphere interactions, and the physical properties (strength, density, mass) of meteoroids and their parent bodies (Campbell-Brown et al., 2013). In this work, we combine analysis of meteor light curves with high-resolution observations of meteor wake (or morphology) and the meteoroid orbit to infer the properties of parent bodies. Our questions include how often and in what way do cometary and asteroidal meteoroids appear to fragment? Do meteors from Jupiter family comets, long period comets, and asteroids show similar light curve shapes? Do single body meteors (which we have defined as those showing very short wake, implying negligible fragmentation) show classical light curve shapes, and can the shape of light curves indicate the strength or fragmentation mode of meteoroids in general?

3.2 Equipment

The data used for this analysis were collected with the Canadian Automated Meteor Observatory (CAMO) (Weryk et al., 2013). Each night, weather and moon permitting, the two station system automatically collects meteor observations. The two stations are located 45 km from each other, in Elginfield, Ontario, Canada (43.193°N , 81.316°W) and Tavistock, Ontario, Canada (43.265°N , 80.772°W). The guided system has two intensified cameras: a wide-field camera with a 28° field of view, used to collect the meteor light curve and compute its orbit,

and a narrow-field 1.5° field of view camera that tracks the meteoroid in flight and provides high-resolution observations. Both cameras have resolutions of 640×480 , and have 12 bit image depth to decrease the chances of image saturation. The wide-field cameras run at 80 frames per second and the narrow-field at 110 frames per second. The narrow-field camera is able to resolve 3 metres per pixel at a range of 100 km.

The wide-field camera detects meteors in real time with the All-Sky and Guided Automatic Real-time Detection (ASGARD) software (Weryk et al., 2008). This software guides a pair of mirror-mounted galvanometers to track the meteor and direct the light into the narrow-field camera. For each frame of the wide-field video, ASGARD searches for pixels above a threshold set at five standard deviations above the mean background. If at least 6 pixels in any 8×8 pixel region are brighter than the threshold, it is flagged as a meteor, provided the detection occurs in at least three consecutive frames. A 5σ threshold detects 67 per cent of all meteors (Weryk et al., 2013).

The two station light curve observations were collected between 2010 April 21, and 2014 May 11, and 3561 observations were recorded in total. The high-resolution video observations were collected between 2010 October 10, and 2014 May 11, and 2041 high quality videos were collected. The discrepancy in collection dates is due to a few factors: the narrow-field cameras were not operational until late 2010; occasionally hardware failures occur (e.g. failure of the mirror control card; shifts of the wide-field plate); and sometimes the tracking is incomplete and the meteor moves out of the field of view.

3.3 Method and Classification

The first task was to classify both the light curve shapes and narrow-field morphologies in our sample. By combining these observations with the meteor's Tisserand parameter, we can investigate the physical properties of different classes of meteoroids, and the relationship between the light curve shape and the fragmentation behaviour.

Because the height, brightness, and orbits of meteors are obtained automatically, errors can occur: ASGARD may mistakenly pick a nearby star or a transient bright pixel instead of the meteor, resulting in erroneous calculated trajectories, orbits, and light curves, or an error in the flat correction can affect the determined brightness values. As a result, the first goal was to examine each of the automated reductions and select the ones with fewest errors for additional analysis.

Our filter was run on all 3561 meteor light curves. 18 per cent of these events belong to meteor showers (the majority being North Taurids, South Taurids, Geminids, and Orionids). As a first filter, any meteors that began or ended off of the field of view were removed from consideration, since accurate calculation of the F parameter requires the beginning and ending heights. These events made up 55 per cent of our original 3561 meteor events.

Next, we plotted the light curve (in terms of absolute magnitude, which is the magnitude the meteor would have if placed at a range of 100 km) as recorded from each station, and generated a smooth curve with low pass filter interpolation. Three interpolated light curves were generated: one from each station, and one that considered data from both stations. A filter based on light curve coverage and agreement between stations was then implemented in two steps:

1. At heights where there was overlap between the stations, the light curves were compared to verify that there was a variance of less than 0.5 mag for at least 50 per cent of the overlapping heights.
2. The overlapping height interval of light curves from each station was verified to span at least 70 per cent of the combined light curve derived from both stations.

The purpose of this filtering was to improve confidence in the ASGARD-generated light curves and trajectories by ensuring that there was good coverage and agreement of each meteor's light curve from both stations. The filters as applied to a sample meteor event are shown in Figure 3.1 Varying sky conditions from each station and spurious ASGARD picks could

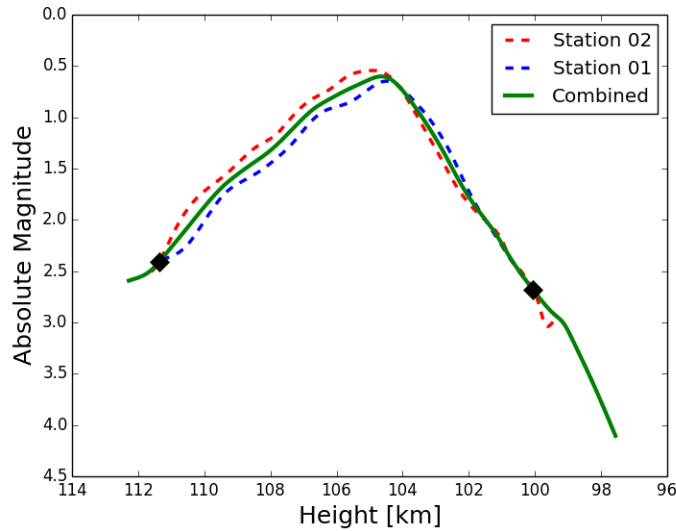


Figure 3.1: The two filters applied to the collected data set ensured that the two station observations agreed with each other. The black diamonds indicate where light curves from both stations (Tavistock is Station 01 and Elginfield is Station 02) begin and end their height overlap.

cause differences in the photometry from each station. In manual reductions of the data, uncertainties are typically of the order of 0.2 mag, but are closer to 0.5 mag for the automated reductions.

After this filtering, the initial set of 3561 meteors was reduced to 891 high-quality observations. The remaining combined meteor light curves were then classified. Light curves with a single peak were classified according to the F parameter. Other shapes seen include double peaked and flat curves, and are shown in Figure 3.2.

There are a few variations on flat light curves that were observed: the entire curve may have a small range of measured brightness; the curve may increase in brightness and remain almost constant at its maximum intensity for the remainder of the observation; or it may begin and remain near a maximum intensity before decreasing. For this work, flat meant that at least 50 per cent of the light curve on both sides of the point of maximum brightness was within 0.5 magnitudes of the maximum brightness. For meteor light curves that fall into this category, it is not informative to calculate an F parameter because the majority of the curve is within the estimated uncertainty of the maximum point. The light curve shape classifications are thus:

early peaked ($F < 0.35$); symmetric ($0.35 \leq F \leq 0.65$); late peaked ($F > 0.65$); double peaked; and flat. We expect classical light curves to fall into the late peaked category.

The next step was to classify the high-resolution narrow-field video observations. These observations offer a new way to study meteoroid ablation, as development of the wake and any fragmentation can be observed directly. These videos were classified manually based on the dominant morphology of the head and wake of the meteor and the fragmentation mode (see Figure 3.3). The morphology of the meteor wake and the head of the meteor are intertwined. A meteoroid experiencing continuous fragmentation is expected to show a long trail and a smeared head due to the differential deceleration of grains of assorted sizes. The meteoroid is crumbling apart as predicted by the dustball model, and may be made of weak material. A meteoroid experiencing negligible fragmentation, on the other hand, may indicate strong material, and will show a rounded head and little to no wake, indicating that very little solid material is being shed by the meteoroid. Meteors that show gross fragmentation, either along the line of motion or transversely, are poorly understood at the heights of the meteoroids being examined in this study (typically $h > 90$ km). The mechanism that allows a meteoroid to disrupt into similarly sized portions is unknown: for large meteoroids, pressure is the cause, but pressure is negligible at the heights at which these faint meteors ablate (Stokan & Campbell-Brown, 2014). The video classifications are listed in Table 3.2 and illustrated in Figure 3.3.

Some meteors (545) clearly showed multiple consecutive morphologies during their ablation; they were not included in this analysis and will be studied in a future work. In total 1496 high-resolution single-morphology video observations were classified.

A sample of long- and short-trailed meteors were measured to determine the average length in metres for the two categories. The length of the meteor was measured as the distance between the head and the portion of the trail that exhibited brightness below the mean background brightness plus two standard deviations. Meteors classified as having long trails were found to be on average, 195 m in length, whereas those classified as having short trails were 90 m. These lengths took into account the range to each meteoroid, as well as a correction for

the perspective angle (the angle between the meteoroid velocity vector and the camera line of sight).

The meteors that made up our final data set had two station observations in agreement with each other, were well tracked, had high-resolution video observations that began and ended on screen, and showed only one dominant morphology.

After classifying the high-resolution narrow-field videos our final data set was made up of 295 meteor events. The range of meteor maximum absolute magnitudes for this set of events is -2.7 to 3.1 mag.

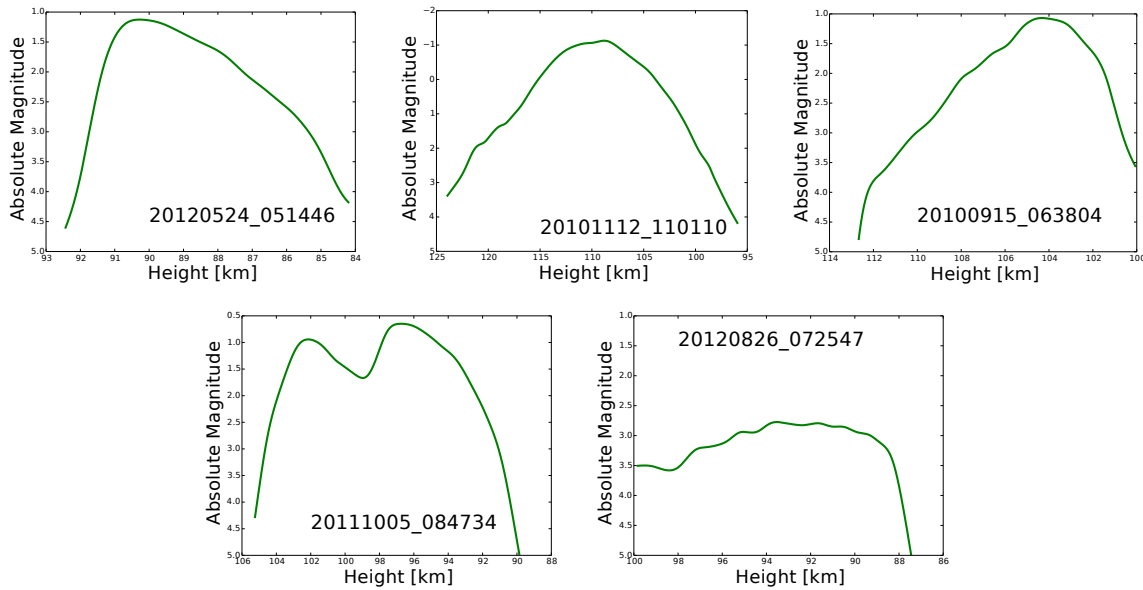


Figure 3.2: Interpolated combined curves of CAMO meteor events showing the different light curve shapes used for the classification. The top three figures are single peaked curves (early, symmetric, late), the bottom left is a double peaked light curve, and the bottom right is a flat light curve.

3.4 Results

3.4.1 High-Resolution Video Morphologies

Over the data collection period for narrow-field video observations, 27 per cent of the videos collected showed multiple morphologies. These events show various combinations of the mor-

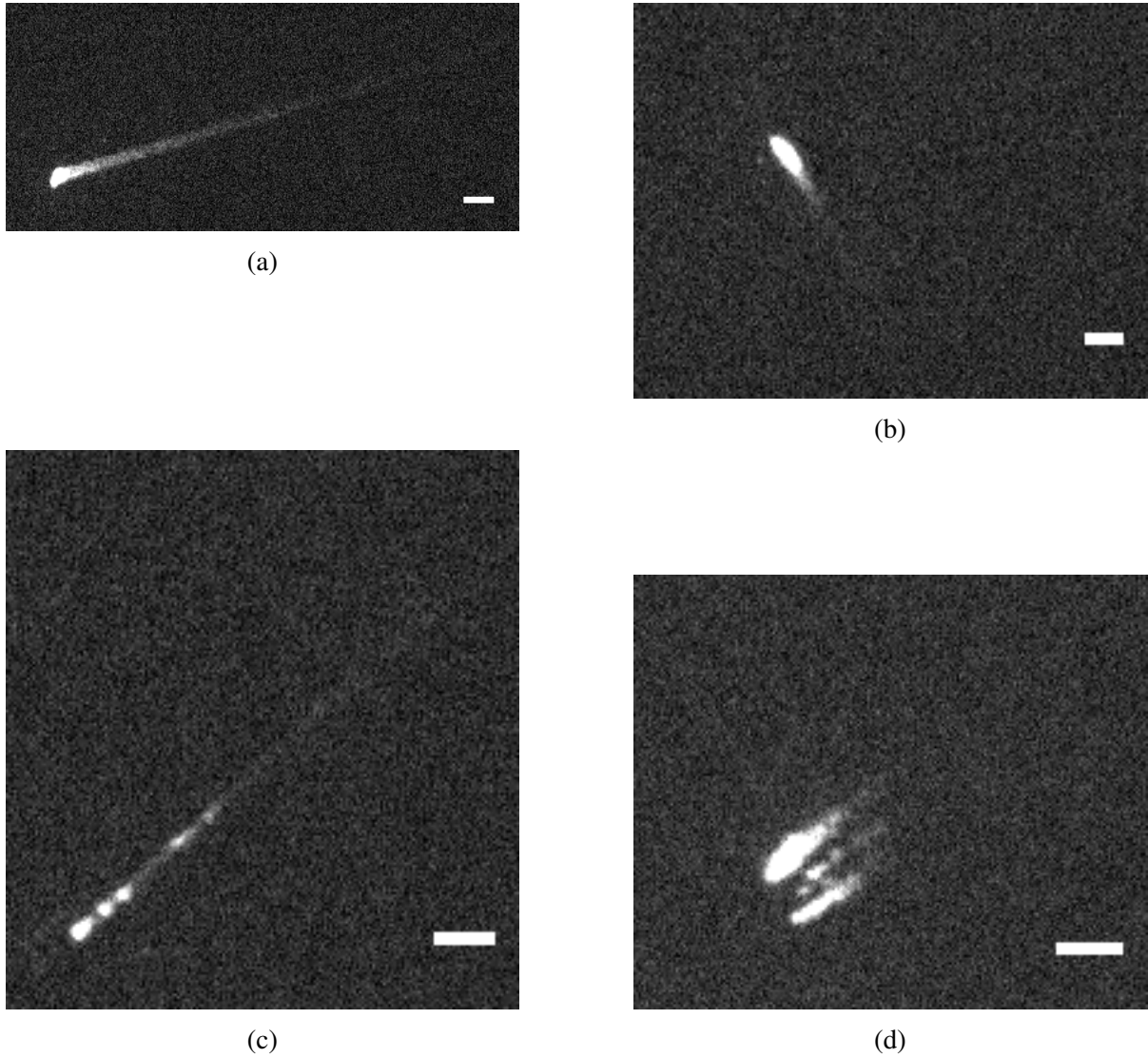


Figure 3.3: The different morphologies used to classify meteor events. The scale bar in each figure corresponds to 100 m. (a) shows a distinct trail (continuous fragmentation) and a smeared head, (b) shows a meteor with a short trail (negligible fragmentation) and a round head, (c) shows a meteor experiencing gross fragmentation, and (d) is a meteor showing transverse fragmentation.

Table 3.2: Classification categories used for the high-resolution video observations collected from CAMO.

Description
Smeared head; distinct wake; no distinct fragments
Round head; little to no wake; no distinct fragments
One or more noticeable fragments
One or more fragments showing transverse speed

phologies described in Table 3.2. For example, many meteors initially show a short trail, and then a long, distinct trail, and then finally gross fragmentation. Others show long distinct trails and then fragmentation either along the line of motion or transversely. These meteor events will be discussed in a future work.

The 1496 single-morphology meteor events are shown in Figure 3.4. Meteors that show distinct trails make up the majority of events seen by CAMO. The surprising proportions of each parent class described by each narrow-field morphology is also indicated on Figure 3.4. Contrary to expectations based on predicted meteoroid strengths, there is equal probability for a meteoroid showing a distinct trail as originating from an asteroid or cometary parent body. Similarly, this also applies to meteoroids showing short trails or gross fragmentation.

3.4.2 Light Curve and Tisserand Parameter Data Distribution

Each of the 891 high-quality light curve meteor observations were classified according to light curve shape. For most events, this meant a description based on the F parameter value. The distribution of all single-peaked, non-flat light curves is shown in Figure 3.5. Flat light curves made up 15 per cent of the classified light curve shapes and double-peaked curves made up 18 per cent (but in reality, the contribution is much less). As described previously, classifying flat light curves according to the F parameter was avoided as at least 50 per cent of the light curve on both sides of the maximum brightness value are within 0.5 mag, the uncertainty in magnitude for light curves computed by ASGARD. The mean F parameter value is 0.49, and

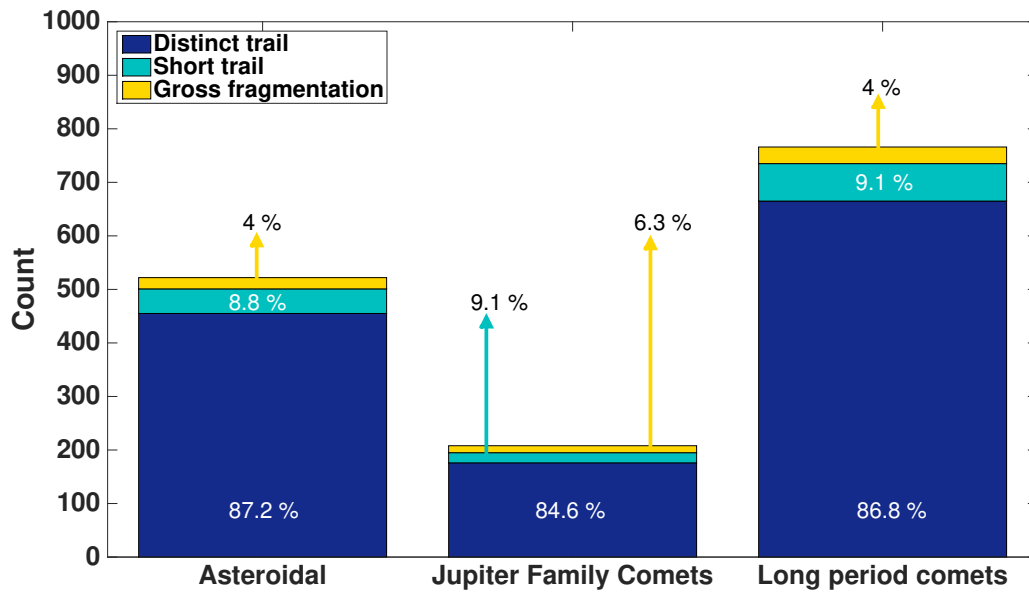


Figure 3.4: All 1496 single-morphology, high-resolution videos, collected between October 10, 2010 and May 11, 2014, according to Tisserand parameter. There are 1296 meteor events that were classified as having distinct trails; 135 meteor events that showed short trails; and 65 events that showed gross fragmentation.

based on Figure 3.5, most single-peaked light curves are symmetric in shape.

Figure 3.6 shows the distribution of meteor events by Tisserand parameter. Values greater than three describe objects with asteroidal orbits: 37 per cent of meteor events fall into this category. Values less than or equal to three but greater than two describe Jupiter family comets, and values less than or equal to two describe long period comets. These make up 14 per cent and 49 per cent of our data set, respectively.

3.4.3 Video morphology subsets

Each video morphology is associated with an expected light curve shape and origin. For example, we would expect asteroidal meteoroids to exhibit high material strength compared to cometary bodies, and thus show less fragmentation, corresponding to short trails in the high-resolution video, and late-peaked light curves. Conversely, we would expect cometary meteoroids to fragment, showing either distinguishable fragments or long trails, and producing a

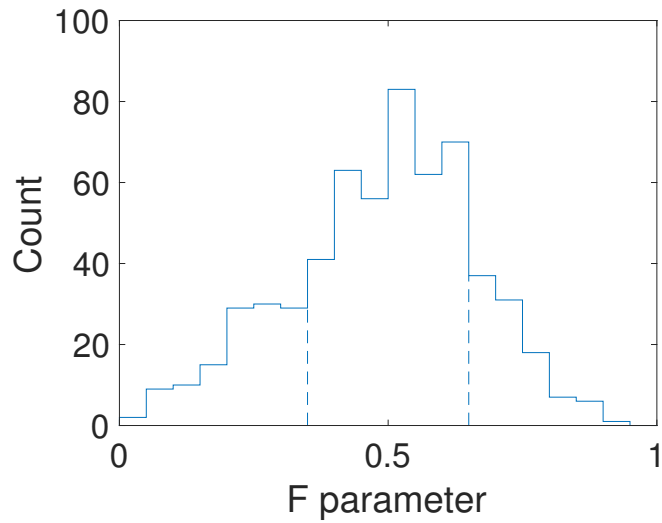


Figure 3.5: Of 891 meteor events, 599 were single peaked. The mean F parameter value is 0.49. Fourteen per cent of the 891 events were early peaked; forty-two per cent were symmetric; and eleven per cent were late-peaked.

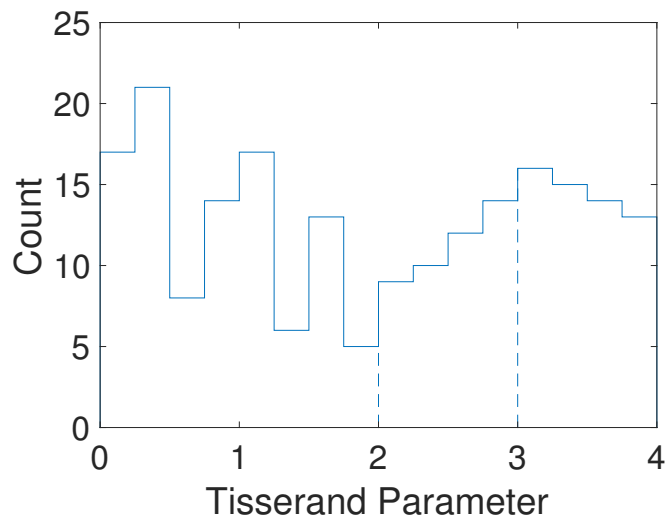


Figure 3.6: Meteor events with Tisserand parameter values between zero and four. The dashed vertical lines indicate the distinction between the parent classes: T_J less than or equal to two describe long period comets; T_J less than or equal to three, but greater than two describe Jupiter family comets; and T_J greater than three describe asteroids.

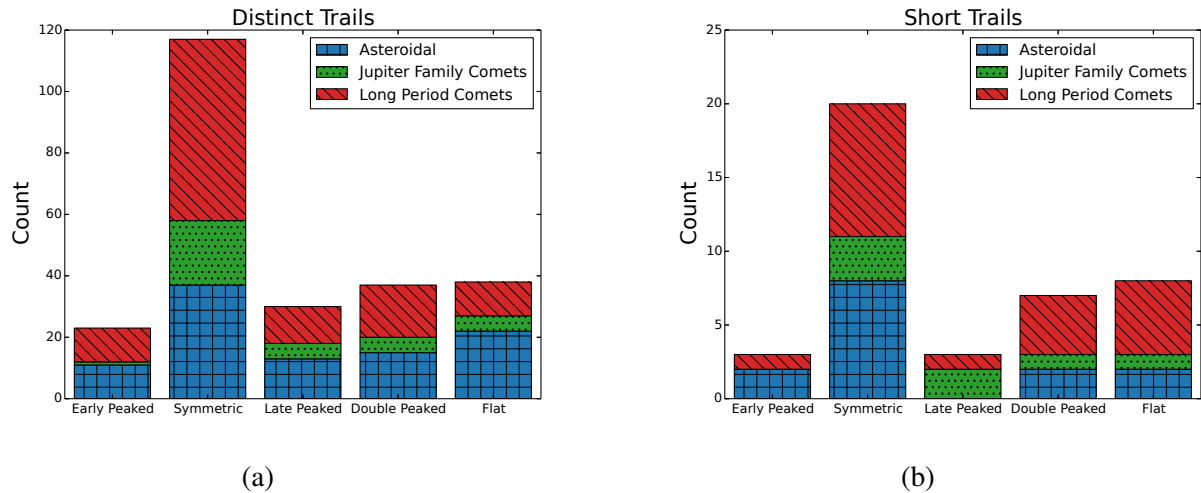


Figure 3.7: Histograms of meteor events according to their light curve shapes. Figure 3.7a shows meteors with distinct trails, and Figure 3.7b shows meteors that show negligible trails.

variety of light curve shapes. Sorting the data by morphology and plotting it as a histogram according to the light curve shape, and divided by parent class contribution allows us to verify or refute these expectations. Figure 3.7 shows the two most commonly seen video morphologies: meteors with distinct trails, and meteors with short trails. Both subsets unexpectedly show very similar distributions of light curve shape (mostly symmetric in both cases), and contributions by parent classes. It should be reiterated that this result is unexpected as meteoroid ablation models predict that meteors with short trails (interpreted to undergo negligible fragmentation) should produce late-peaked light curves, which was not the case here.

3.4.4 Parent class subsets

To evaluate predictions of differential ablation and fragmentation behaviour between asteroidal and cometary meteoroids, the data set was sorted by Tisserand parameter into two groups (asteroidal origin and cometary origin), and histograms were plotted according to the light curve shape and divided by high-resolution video morphology. These are shown in Figure 3.8. Asteroidal and cometary meteoroids show similar properties, evidenced by similar distributions in Figure 3.8. Asteroidal meteors, which we expect to be stronger than those originating from

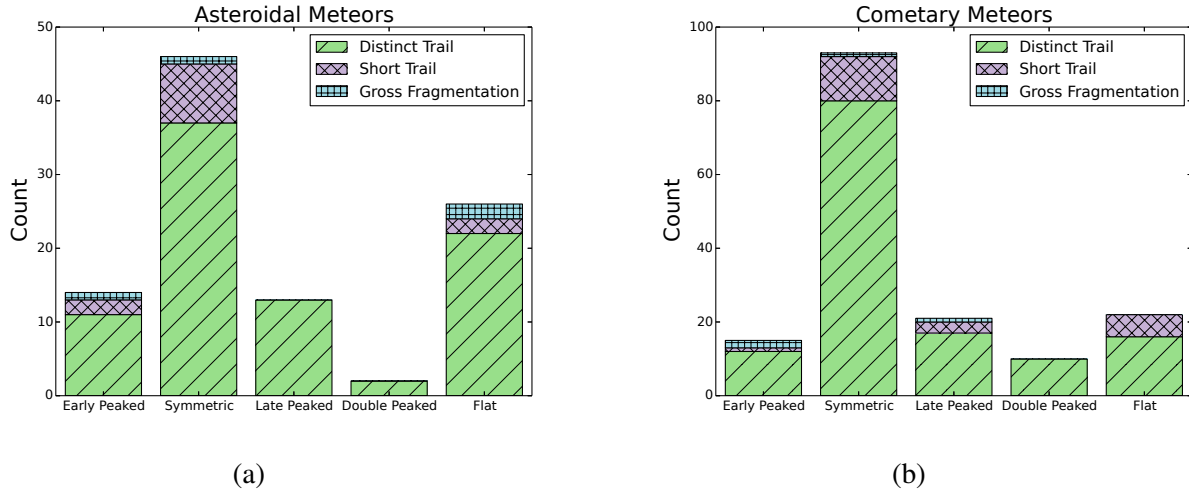


Figure 3.8: Meteor events segregated by their Tisserand parameter, and then by their light curve shape. Figure 3.8a shows the distribution of asteroidal meteors, and Figure 3.8b shows the distribution of cometary meteors.

comets, were expected to show mostly late-peaked curves, and negligible fragmentation.

3.4.5 K_b parameter

The K_b parameter can be used as a measure of the strength of meteoroids, so one would expect that meteors with long trails, which are crumbling, would have lower strength than meteors which fragment into a few pieces, while non-fragmenting meteors should be strongest. In Figure 3.9, the meteor events are sorted by video morphology and the distributions of K_b for each morphology are plotted. The different K_b groups are listed in the top panel of the figure. This allows us to evaluate the strength and volatility of the events according to their observed morphology. Meteors showing long trails are expected to be weak, and to have low K_b values, whereas those showing gross fragmentation are expected to be strong, fracture into large objects, and have high K_b values.

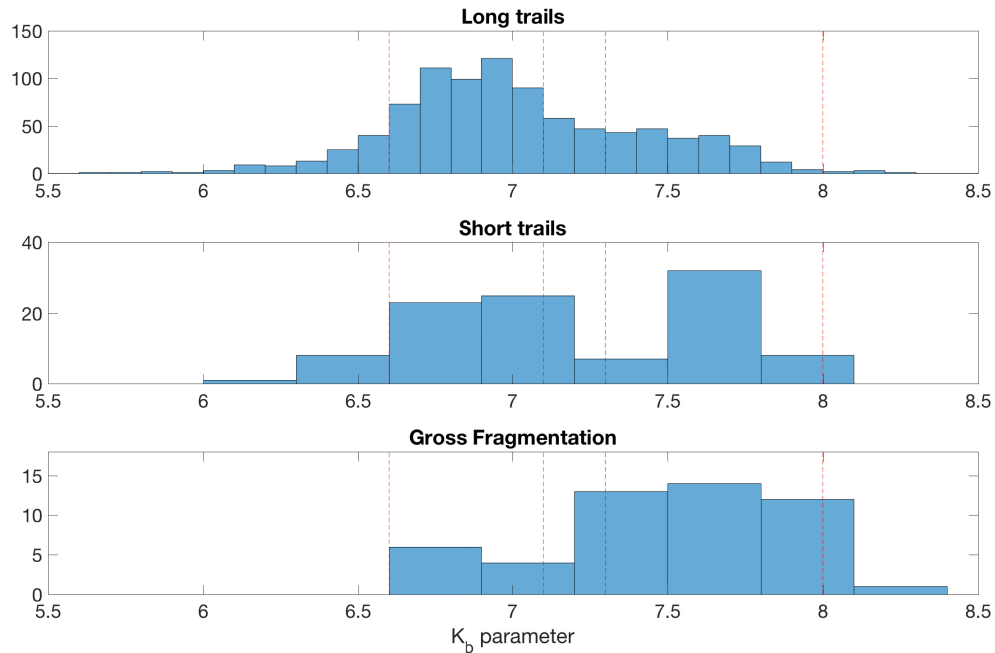


Figure 3.9: K_b histograms for the three morphologies. The groups defined by Ceplecha (1988) are given in the top panel, and the red dashed lines define those boundaries.

3.4.6 Orbital elements

As discussed below, the Tisserand parameter is not always a reliable indicator of origin. Inclination, on the other hand, is not affected by radiative forces, so low or high inclination should reliably divide long period cometary material from asteroidal or Jupiter family comet material. Meteor events were analysed according to their orbital elements to see if any further relationships exist. Events with inclination uncertainties greater than five degrees, were removed, as were those with unrealistic velocities and poor convergence angles. A plot of inclination versus eccentricity is shown in Figure 3.10, with the narrow-field video morphologies shown in different colours. Objects of asteroidal origin are expected to have low inclinations and low eccentricities, as are objects that show little to no fragmentation.

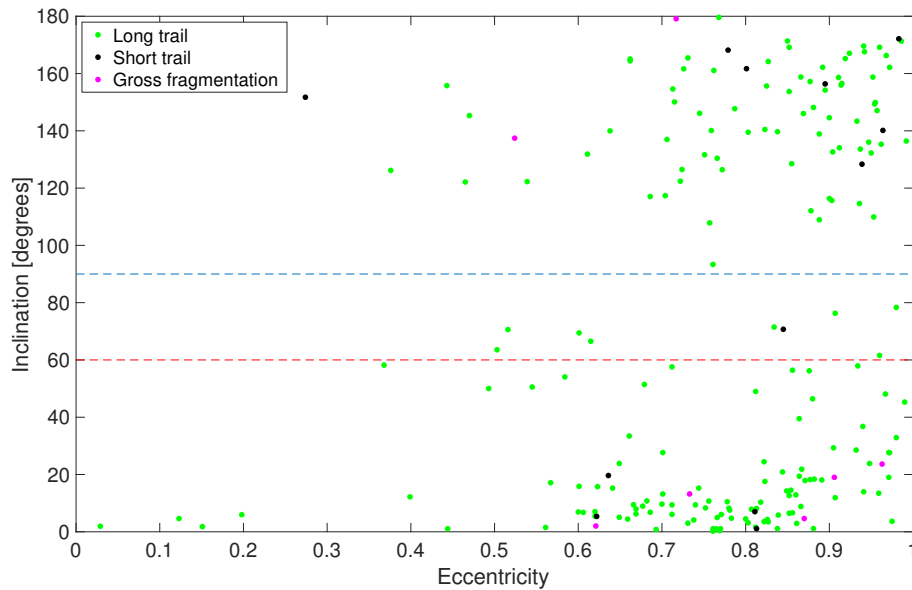


Figure 3.10: This figure includes all events with acceptable convergence angles and velocities, that end onscreen. The remaining events with inclination uncertainties greater than 5 degrees, were removed. The blue dashed line marks the boundary between prograde and retrograde objects, and the red dashed line marks the boundary between low and high inclination objects.

3.5 Discussion

Figure 3.4 shows that most of the meteors observed by CAMO have distinct trails, consistent with continuous fragmentation. This supports the dustball model, implying that most meteoroids are made of loosely bound grains which separate when the meteoroid heats up. A study by Weryk et al. (2013) found that 75 per cent of all tracked, multistation events showed fragmentation in some form. We find that approximately 90 per cent of our full data set (1496 video classifications) show fragmentation (continuous or gross). This discrepancy may be due to a few factors: different data sets were used for the two studies and the threshold criteria for fragmentation may have been different. The Weryk et al. (2013) study considered multistation events, whereas this study did not require that narrow-field observations be recorded at both sites as long as there were two station wide-field observations to calculate the meteor trajectory and light curve. The mean F parameter value for our light curve data set of 891 meteors is 0.49, and this is consistent with other studies on faint meteor light curves: Fleming et al.

(1993) studied 34 meteors, mainly sporadic meteors, and found an average F value of 0.51 for curves 1 and 2 magnitudes below the peak magnitude; Beech & Murray (2003) analysed Leonid light curves from 1998 - 2001, and found a range of F values from 0.487 to 0.652, for light curves measured 1.25 mag below the peak magnitude. In this work, the mean F parameter for cometary meteors was 0.49, and for asteroidal meteors was 0.48, which is essentially the same.

The ranges used for the F parameter (early peaked [$F < 0.35$]; symmetric [$0.35 \leq F \leq 0.65$]; late peaked [$F > 0.65$]) were chosen such that the symmetric range would have a smaller range than early peaked and late peaked, to ensure that only truly symmetric curves would be selected. However, this is subjective. To assess how the results would change if we implemented a stricter range for the symmetric category, we reclassified meteor events, allowing the symmetric category to hold only those events with $0.4 \leq F \leq 0.6$. We found that both cometary and asteroidal groups of meteors kept approximately the same fraction of events that show distinct trails, short trails, and gross fragmentation, in spite of the different F range used for symmetric light curves. With a narrower range, symmetric light curves are still the most frequently seen, but late peaked light curves become a larger portion of the overall distribution. A narrower range for symmetric light curves changes the proportion of events in each F parameter category, but does not change the overall results of our study.

The most surprising result to come out of this work are the proportions shown in Figure 3.4. We expected that most cometary meteors would show continuous fragmentation (long distinct trails), while asteroidal meteoroids would show fragmentation less frequently (short, negligible trails). As seen in Figure 3.4, this was not the case. The fact that the proportions are almost equal suggests that the fragmentation mode [distinct trail (dustball fragmentation) vs negligible trail (single-body ablation) vs gross fragmentation] is not an indicator of the object's origin. This implies either (1) that cometary and asteroidal meteors may be more similar in structure than previously believed. This agrees well with studies of comet Wild 2 (on particles smaller than those in our data set) that suggest large-scale radial mixing occurred in the early Solar

System (Brownlee et al., 2012). Or (2) that sporadic meteors on asteroidal orbits may have originated from cometary parent bodies, but had their orbits slowly circularised by radiative forces, pushing them across the dynamic boundary.

The majority of meteors observed in this study are cometary in origin, as shown in Figure 3.6. However, the Tisserand parameter is a constant only under the restricted three-body problem. It is important to note that we only see the current orbit in our analysis. Objects that appear to be on asteroidal orbits may have had their originally cometary orbits perturbed by radiative forces. Overlap between categories is a possibility, and has been previously observed (comet 2P/Encke has an asteroidal orbit, for example). This means that the distribution of meteor events shown in Figure 3.6 may not accurately describe the observed objects: because Poynting Robertson drag will increase the Tisserand parameter, the particles found to be asteroidal in origin may actually come from Jupiter family comets. To assess the likelihood of contamination between dynamic groups, we considered dynamic and collisional lifetimes of small particles. Simulations done by P. Pokorny (private communication) of millimetre-sized particles show that within 50 000 years, objects on Jupiter family comet orbits are able to change their Tisserand parameters to values greater than 3, suggesting that contamination of asteroidal objects by decaying cometary meteoroids is likely. This may explain the similarities found in this study between dynamically asteroidal and cometary particles.

The orbital elements of our meteor events were examined to better understand how their Tisserand parameters relate to their orbital elements. From Figure 3.10, we find that there are almost no events with low inclinations and low eccentricities, where we would expect most asteroidal objects to belong. Interestingly, we find that by colouring the events by their video morphology, it becomes apparent that many of the short trailed objects are in retrograde orbits (7 vs 5 in prograde orbits). The difference is greater when the events are divided into groups with inclination greater than and less than 60° (the red dashed line): we see that there are more high inclination short trailed objects than low inclination (8 vs 4). While there are very few short trailed objects that end onscreen in total, these results are lower limits. We were cautious

in flagging events as ending onscreen: both wide-field observations needed to end onscreen, or the event was flagged as ending offscreen. When we recreate Figure 3.10 with events that end both on and offscreen, the same trend is seen (short trailed events are highly inclined), but in greater numbers (39 retrograde vs 27 prograde; 49 high inclination vs 17 low inclination). Objects that show minimal amounts of fragmentation are expected to have low inclinations and eccentricities, which is contrary to our results. While it is possible to change the inclination of a particle dramatically through a planetary interaction, it is very unlikely to change a prograde orbit to a retrograde orbit, so most of these non-fragmenting objects are likely cometary in origin.

Figure 3.7 shows that the majority of meteors observed by CAMO are cometary meteoroids with symmetric light curves. We expected meteors with asteroidal origins to show minimal amounts of fragmentation (little to no wake in the high-resolution video), and we expected meteors with negligible fragmentation to have late peaked light curves, consistent with single body ablation. Figure 3.8a shows that our data do not support those predictions. Instead the majority of dynamically asteroidal meteors observed with CAMO show symmetric light curves (indicative of a distribution of grain sizes) and long trails, like the cometary meteoroids. These objects were expected to ablate as single bodies, and the lack of classically shaped light curves is unexpected, but may be due to non-uniform compositions or densities, or non-spherical shapes. Pockets of volatiles may be present. This does not explain the observed trails, however.

From Figure 3.7b, we see that meteors with short trails show mainly non-classical light curves. This may also be indicative of differential ablation. We find that meteor light curves are unable to predict the fragmentation behaviour of the meteoroid.

The K_b parameter, when plotted for sporadic meteors, shows two distinct maxima (Ceplecha, 1967). The distribution of our meteor events, when sorted by video morphology, is shown in Figure 3.9. Non-fragmenting meteors (those that show short trails) are expected to be strongest; the crumbling meteors that show long trails are expected to be the weakest; and those that show gross fragmentation are somewhere in between. The K_b parameter is also

a measure of volatility: a strong meteoroid with pockets of volatiles will have a high begin height. Meteors which do not fragment but have higher than expected begin heights (low K_b parameter) may be like this. We find that meteors that show long trails (crumbling meteors) are predominantly weak; meteors that show short trails (non-fragmenting) can be either weak or strong, surprisingly; and meteors that show gross fragmentation are strong.

3.6 Conclusions and Future Work

In this work, we classified and compared faint meteors on asteroidal and cometary orbits by combining high-resolution video observations, light curve shape, and the computed meteoroid orbit. We find that the majority of meteors observed with the Canadian Automated Meteor Observatory have cometary orbits ($T_J \leq 3$) and show long distinct trails in high-resolution video (pixel scale ~ 3 m at 100 km). We observed that dynamically asteroidal meteors tended to fragment as often as their cometary counterparts. This contradicts the expectation that asteroidal objects are stronger and less susceptible to fragmentation, and may mean that the particles on asteroidal orbits are actually cometary.

The two most commonly seen morphologies, distinct trails and short trails, show the same trend, unexpectedly: whether a meteoroid experiences continuous fragmentation or not, it is likely to show a symmetric light curve. This is not what we predicted: meteoroids that show negligible fragmentation (i.e. a short trail) were expected to show a late peaked light curve. As a result, ablation of a non-homogeneous object, or differential ablation, may have to be considered for these cases. Light curve shape should not be considered a reliable sign of a meteoroid's fragmentation behaviour. When the dataset is analysed in terms of the Tisserand parameter, we see that dynamically asteroidal meteors show remarkably similar proportions and properties to cometary meteors.

With our large data set, there are a few next steps to consider. In this work, we did not separate out shower meteors. Doing so will allow us to compare our results to similar studies

of double-station video observations of meteors, such as work by Štork et al. (2002) or Koten et al. (2004). The goal of that work would be to do the same kind of analysis as done in this study (i.e. study light curve and fragmentation behaviour to infer strength and structure), but to control the parent body more strictly.

From our original video data set of 2041 observations, we removed 545 events that showed multiple morphologies. Objects that we observe beginning with no trail which then develop one may allow for detailed modelling of fragmentation and determination of physical properties, since we are seeing the onset of fragmentation. Conversely, meteoroids that show a trail that vanishes, may be objects with a unique grain size distribution, with a superposition of a certain conventional profile (e.g. power law) and a single large refractory grain. Finally, we have a number of meteor events that show gross fragmentation with both transverse dispersion of fragments and dispersion along the direction of motion. As the mechanism responsible for the transverse spread of fragments at these heights ($h > 90$ km) is poorly understood, this set of events may be able to provide some strong constraints for new models of small meteoroid fragmentation.

Bibliography

- Beech, M., & Murray, I. S. 2003, *Monthly Notices of the Royal Astronomical Society*, 345, 696
- Borovička, J. 2007, in *IAU Symposium*, Vol. 236, *IAU Symposium*, ed. G. B. Valsecchi, D. Vokrouhlický, & A. Milani, 107–120
- Borovička, J., Spurný, P., & Koteš, P. 2007, *Astronomy and Astrophysics*, 473, 661
- Brownlee, D., Joswiak, D., & Matrajt, G. 2012, *Meteoritics and Planetary Science*, 47, 453
- Brownlee, D., Tsou, P., Aléon, J., et al. 2006, *Science*, 314, 1711
- Campbell-Brown, M. D., Borovička, J., Brown, P. G., & Stokan, E. 2013, *Astronomy and Astrophysics*, 557, A41
- Campbell-Brown, M. D., & Koschny, D. 2004, *Astronomy and Astrophysics*, 418, 751
- Cepelcha, Z. 1958, *Bulletin of the Astronomical Institutes of Czechoslovakia*, 9, 154
- . 1967, *Smithsonian Contributions to Astrophysics*, 11, 35
- . 1988, *Bulletin of the Astronomical Institutes of Czechoslovakia*, 39, 221
- Drolshagen, G. 2008, *Advances in Space Research*, 41, 1123
- Faloon, A. J., Thaler, J. D., & Hawkes, R. L. 2004, *Earth Moon and Planets*, 95, 289
- Fleming, D. E. B., Hawkes, R. L., & Jones, J. 1993, in *Meteoroids and their Parent Bodies*, ed. J. Stohl & I. P. Williams, 261
- Hawkes, R. L., & Jones, J. 1975, *Monthly Notices of the Royal Astronomical Society*, 173, 339
- Jacchia, L. G. 1955, *Astrophysical Journal*, 121, 521

- Kikwaya, J.-B., Campbell-Brown, M., & Brown, P. G. 2011, *Astronomy & Astrophysics*, 530, A113
- Koten, P., & Borovička, J. 2001, in *ESA Special Publication*, Vol. 495, *Meteoroids 2001 Conference*, ed. B. Warmbein, 259–264
- Koten, P., Borovička, J., Spurný, P., Betlem, H., & Evans, S. 2004, *Astronomy and Astrophysics*, 428, 683
- Murray, I. S., Beech, M., Taylor, M. J., Jenniskens, P., & Hawkes, R. L. 2000, *Earth Moon and Planets*, 82, 351
- Murray, I. S., Hawkes, R. L., & Jenniskens, P. 1999, *Meteoritics and Planetary Science*, 34, 949
- Stokan, E., & Campbell-Brown, M. D. 2014, *Icarus*, 232, 1
- Štork, R., Koten, P., Borovička, J., & Spurný. 2002, in *ESA Special Publication*, Vol. 500, *Asteroids, Comets, and Meteors: ACM 2002*, ed. B. Warmbein, 189–192
- Weryk, R. J., & Brown, P. G. 2013, *Planetary and Space Science*, 81, 32
- Weryk, R. J., Brown, P. G., Domokos, A., et al. 2008, *Earth Moon and Planets*, 102, 241
- Weryk, R. J., Campbell-Brown, M. D., Wiegert, P. A., et al. 2013, *Icarus*, 225, 614
- Whipple, F. L. 1950, *Astrophysical Journal*, 111, 375
- . 1951, *Astrophysical Journal*, 113, 464
- Wiegert, P., Vaubaillon, J., & Campbell-Brown, M. 2009, *Icarus*, 201, 295

Chapter 4

Luminous Efficiency -I

A version of this chapter has been published as:

Subasinghe, D; Campbell-Brown, M.D., & Stokan, E. (2017). *Luminous efficiency estimates of Meteors -I. Uncertainty Analysis*. Planetary and Space Science, 143, 71

4.1 Introduction

Determining the mass of a meteoroid, a basic property, is currently very difficult to do. Because most meteoroids are too small to reach the ground, meteoroid mass needs to be determined through observations. The simplest method is to use the total luminous energy emitted during ablation. The large uncertainty associated with mass is due to many unknown variables, such as the bulk density, shape, and luminous efficiency, and their (possible) changes during ablation. Spacecraft hazard estimates rely on accurate meteoroid masses: while rare, collisions and damage to satellites by meteoroids have occurred (Caswell et al., 1995).

There are two coupled differential equations in classical meteor physics that describe the state of the meteoroid and allow mass to be determined: the luminous intensity equation and the drag equation. The luminous intensity, given in Equation 4.1, assumes the brightness (or

luminous intensity, I) of a meteor is proportional to the change in kinetic energy.

$$I = -\tau \frac{dE_k}{dt} = -\tau \left(\frac{v^2}{2} \frac{dm}{dt} + mv \frac{dv}{dt} \right) \quad (4.1)$$

The proportionality constant, τ , is the luminous efficiency, the fraction of kinetic energy dissipated as meteor light. The m refers to the total instantaneous meteoroid mass, including any fragments. Despite their small masses ($< 10^{-4}$ kg), the majority of small meteoroids do fragment (Subasinghe et al., 2016), and that light is taken into account when calculating the *photometric* mass.

Equation 4.1 may be rearranged to solve for the photometric mass, but there is typically a large associated uncertainty, due to the vast range in luminous efficiency values. The second term in Equation 4.1 is often neglected, as the deceleration for fast, faint meteors is negligible, relative to the first term. Using typical values, it can be shown that for slow meteors the deceleration term is almost equal in importance to the mass loss term, but becomes significantly less important at higher speeds (i.e. the deceleration term is about 40% of the mass loss term for a meteor moving at 11 km/s, but only 1% for a meteor travelling at 70 km/s).

The drag equation given in Equation 4.2, can also be used to determine the mass of a meteoroid, and is derived through conservation of momentum.

$$\frac{dv}{dt} = - \frac{\Gamma \rho_{atm} v^2 A}{m^{\frac{1}{3}} \rho_m^{\frac{2}{3}}} \quad (4.2)$$

The mass in this equation is called the *dynamic* mass, as it is based on the deceleration of the largest, brightest fragment (or group of similarly sized fragments). The other variables in Equation 4.2 are the drag coefficient Γ , the atmospheric density ρ_{atm} , the velocity v , the shape factor A , and the meteoroid density ρ_m . Previous studies have found that the dynamic mass of faint meteors is consistently smaller than the photometric mass, and is thus not an accurate measure of the true meteoroid mass for fragmenting meteors (Verniani, 1965). Again, this is because the photometric mass considers the mass of all light producing fragments, and the

dynamic mass only considers the largest, brightest fragment.

Since most meteoroids do fragment, it is therefore useful to better understand the luminous efficiency to determine the meteoroid mass through the luminous intensity equation. The goal of this study is ultimately to examine faint meteoroids that do not appear to fragment, to determine their luminous efficiencies. In those cases, the dynamic mass, found by the deceleration, is equivalent to the photometric mass, and we can solve for the luminous efficiency. This luminous efficiency can then be used to find the masses of other meteoroids, even those that fragment. It has been suggested that the luminous efficiency depends on meteoroid speed and height, camera spectral response (an iron-rich meteoroid may emit strongly in the blue portion of the visible spectrum, but may not be detected if the camera system is not sensitive to that range), meteoroid and atmospheric composition, and possibly meteoroid mass, among other factors, but the extent to which it depends on each variable is unknown (Cepilecha et al., 1998).

4.1.1 Previous luminous efficiency studies

As a meteoroid enters the atmosphere, it heats up through collisions with atmospheric atoms and molecules. This results in meteoroid ablation and the release of meteoritic atoms and molecules into the atmosphere. Evaporated meteoritic material interacts with atmospheric molecules or other ablated atoms, leading to the excitation of the meteoritic and atmospheric species. The luminosity observed is due to the decay of these excited states and is emitted in spectral lines.

Many of the early luminous efficiency studies were done by Opik, who used a theoretical approach to determine luminous efficiencies for various atoms. Uncertainty in the approach used led to questions of the validity of his work: he is mentioned here for completeness. Verniani (1965) combined the drag equation with the luminous intensity equation to solve for the luminous efficiency. This method explicitly equates the photometric mass with the dynamic mass, which is problematic since these masses are not equivalent for meteoroids that fragment, and studies have shown that the majority of observed meteoroids show fragmentation (Subas-

inghe et al., 2016; Weryk et al., 2013). Verniani (1965) attempted to correct for fragmentation, and assumed that luminous efficiency can be described as shown in Equation 4.3, with luminous efficiency proportional to speed raised to some power.

$$\tau = \tau_0 v^n \quad (4.3)$$

He found for the 413 Super-Schmidt meteors he studied, that $n = 1.01 \pm 0.15$ and 1.24 ± 0.22 for fragmenting and non-fragmenting meteors respectively. He further investigated whether luminous efficiency depends on mass (he found that it does not), and found that luminous efficiency does not depend on the atmospheric density. He used a single non-fragmenting meteor, suggested to be asteroidal in origin (based on orbital characteristics), to conclude that in the photographic band pass, the constant τ_0 in Equation 4.3, is $\log_{10} \tau_0 = -4.37 \pm 0.08$ for $n = 1$. These results, along with the following studies, are illustrated in Figure 4.1.

Many lab experiments were performed in the sixties and seventies, with the obvious advantage of being able to control many aspects of the ablation process such as the mass and composition of the ablating particles, and the gas density in which the particles ablate. One of the limitations of lab experiments for luminous efficiency estimates is the difficulty in reaching all valid meteor speeds – Friichtenicht et al. (1968) reached speeds between 15 - 40 km/s, while Becker & Friichtenicht (1971) explored speeds between 11 - 47 km/s. The experimental lab set up involved charging and accelerating particles in a Van deGraaf generator (detectors measured the charge and velocity), and then observing as the particles ablated in a gas region meant to simulate free molecular flow (13.3 Pa). Becker & Friichtenicht (1971) used 167 iron and 120 copper spherical simulated meteors, with diameters between 0.05 and 1 micron, and their results are shown in Figure 4.1. Becker & Slattery (1973) used essentially the same methods as Becker & Friichtenicht (1971), but studied silicon and aluminium particles with similar diameters, as they ablated in a gas region of air, nitrogen, or oxygen, at a pressure around 27 Pa. These results are not applicable to optical meteors directly, as these lab studies used particles much smaller than the millimetre sized objects that most optical cameras observe, and

the pressures at which the micron sized particles ablated correspond to heights much lower (between 55 - 65 km) than those at which optical cameras typically observe (around 90 - 110 km).

Artificial meteoroids are another method of determining the luminous efficiency. In this method, objects of known mass and composition are subjected to atmospheric re-entry, and observed as they ablate. Ayers et al. (1970) used iron and nickel objects, launched between 1962 and 1967, observing a total of ten artificial meteors. These artificial meteoroids had either a disk or cone shape, and their masses ranged between 0.64 - 5.66 grams. The average begin and end heights were 76 and 66 km, respectively. These artificial meteoroids were observed optically, and the luminous intensity and velocity were collected. Combined with the measured initial meteoroid mass, the luminous efficiency was calculated using a simplified version of Equation 4.1, in which the second term (related to the deceleration) is ignored. Ayers et al. (1970) found that $n = 1.9 \pm 0.4$ in Equation 4.3 for four artificial meteoroids, including one from McCrosky & Soberman (1963). Ayers et al. (1970) also formulated a luminous efficiency relationship for meteoroids of stony composition, assuming that 15% of the mass is iron, which is the main emitter in their blue sensitive cameras: that between 20 and 30 km/s, the luminous efficiency increases monotonically; and that above 30 km/s, $n = 1$. This may not be applicable to other more red-sensitive optical systems. They noted that this work was a first approximation. A slight reworking of the Ayers et al. (1970) results was done by Ceplecha & McCrosky (1976), who increased the proportion of iron by weight from 15% to 28%. The luminous efficiency suggested by Ceplecha & McCrosky (1976) is a piece-wise function (shown in Figure 4.1), and was used for fireball analysis.

Jones & Halliday (2001) defined an excitation coefficient, which is the average number of times a meteoritic atom is excited during ablation. In combining theory and lab measurements, they found that their primary excitation probability is unphysical beyond 42 km/s (they assumed ionised atoms are unavailable for excitation). They referred to scattering and diffusion cross-sections to describe the excitation coefficient, but found that the values were higher than

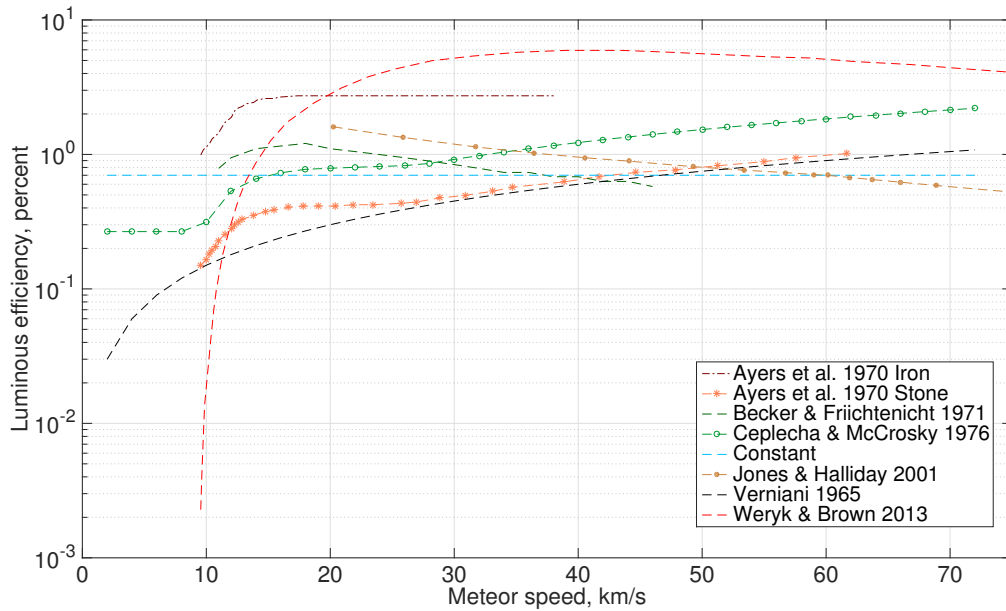


Figure 4.1: Some of the past work done on luminous efficiency using various methods (lab experiments; artificial meteors; radar and optical observations). Note that the luminous efficiency values (given as a percentage) are shown on a log scale: the large discrepancies between luminous efficiency values for a given meteor speed cause large uncertainties in the derived mass. The constant 0.7% luminous efficiency corresponds to the value used in this study for the simulated meteor events.

experimental values suggested.

Simultaneous optical and radar observations of meteors were used by Weryk & Brown (2013) to determine the luminous efficiency for the band pass of their GEN-III image intensifiers. The ratio of the ionisation coefficient β (the number of electrons produced per ablating atom) to the luminous efficiency τ can be determined through radar and video measurements, and assuming a value for either β or τ allows the other to be determined. Jones (1997) determined an expression for β using both theory and observations, which Weryk & Brown (2013) used to determine a peak bolometric value of $\tau = 5.9\%$ at 41 km/s, for their Gen-III band pass (470 - 850 nm).

4.2 Method

The purpose of this work is to develop a method, using simulated data, to calculate luminous efficiency from non-fragmenting meteors observed with a high-resolution optical system, and to investigate the sensitivity of the method to the various assumed parameters. Equating the dynamic and photometric masses is appropriate, provided the meteoroid does not fragment, and allows for the determination of the luminous efficiency. The classical meteoroid ablation equations apply to a solid, single, non-fragmenting body. The Canadian Automated Meteor Observatory (CAMO; discussed below) has at best, a resolution of 3 metres per pixel in its narrow-field optical camera, which means it can confirm that the meteor events collected do not significantly fragment on that scale. The dynamic mass can then be equated to the photometric mass to solve for the luminous efficiency: rearranging Equations 4.1 and 4.2 gives us:

$$m = -\frac{\Gamma^3 \rho_{atm}^3 v^6 A^3}{\rho_m^2 \left(\frac{dv}{dt}\right)^3} \quad (4.4)$$

$$\tau = -\frac{I}{\frac{v^2}{2} \frac{dm}{dt} + mv \frac{dv}{dt}} \quad (4.5)$$

Assumptions must be made for certain parameters: the drag coefficient Γ , which can range from 0 - 2; the shape factor A , given by $\frac{\text{cross-sectional area}}{\text{volume}^{\frac{2}{3}}}$; and the meteoroid density ρ_m , which can range from 1000 - 8000 kg/m³. For the drag coefficient and the shape factor, typical values were used ($\Gamma = 1$; $A = 1.21$ (sphere)). An atmospheric density profile was taken from the NRLMSISE-00 model (Picone et al., 2002).

4.2.1 Future application to real data

The Canadian Automated Meteor Observatory is a two station, image intensified video system, located in Ontario, Canada (Weryk et al., 2013). The two stations are approximately 45 km apart, with one station in Tavistock, Ontario, Canada (43.265°N, 80.772°W), and the other

in Elginfield, Ontario, Canada (43.193°N, 81.316°W). Sky conditions permitting, the camera systems run each night. The guided system, used for data collection, consists of two cameras: a wide-field camera, with a field of view of 28°, and a narrow-field camera, with a field of view of 1.5°. The wide-field cameras, which run at 80 frames per second, allow for orbit determination, as well as light curve measurements; and the narrow-field cameras, which run at 110 frames per second, provide high-resolution observations of the meteoroid. To reduce the possibility of image saturation, the cameras each have 12 bit image depth.

Meteors are detected in the wide-field camera in real time with the All Sky and Guided Automatic Realtime Detection (ASGARD) software (Weryk et al., 2008), and ASGARD directs a pair of mirrors to track the meteor and direct the image into the narrow-field camera.

With the high-resolution narrow-field cameras, meteors that appear to show single-body ablation can be selected and studied to determine their luminous efficiencies. In a future work, we will analyse a number of events and apply this luminous efficiency determination method to them. The meteor events will be reduced using *mirfit*: software designed to process meteor events recorded with the CAMO tracking system, and provide high-precision position measurements (sub-metre scale).

4.3 Sensitivity Analysis

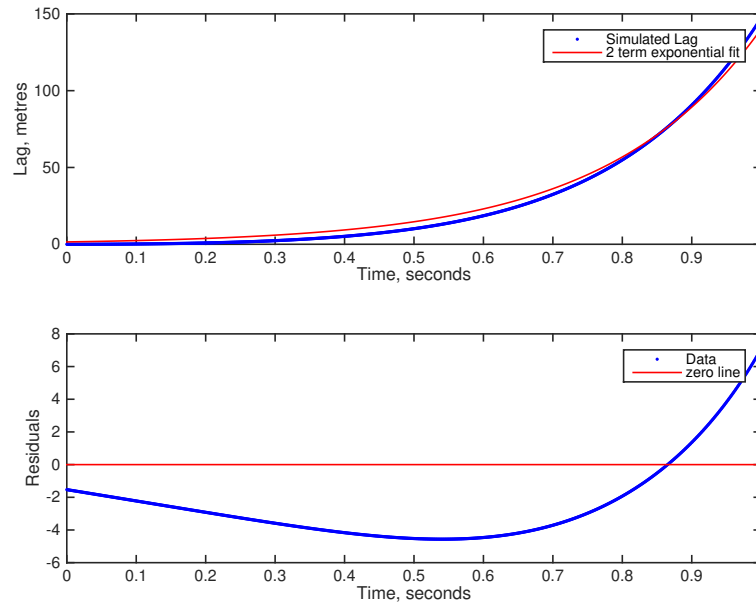
One of the main difficulties in solving for luminous efficiency is determining the measured deceleration of the meteor, needed for both the dynamic mass (Equation 4.4) and the luminous efficiency (Equation 4.5). Small uncertainties in the measured position result in large point-to-point errors in the speed, and very large scatter in the deceleration. To test the sensitivity of our technique to the assumptions made and the fitting techniques used, we simulated meteors using the model of Campbell-Brown & Koschny (2004). We used the classical ablation model to investigate different smoothing and fitting algorithms. The lag is the distance that the meteoroid falls behind an object with a constant velocity (equal to the initial meteoroid velocity,

which is determined by fitting the first half of the distance-time data), and requires a monotonically increasing form. As a first attempt, we expect an exponential relationship between the meteoroid lag and time, based on the atmospheric density encountered by the meteoroid increasingly roughly exponentially with time. A two-term exponential will provide a better fit than a single-term exponential (more terms and/or higher order terms will fit the data better, but it is important to note that adding more terms will eventually overfit the data and does not have any physical justification).

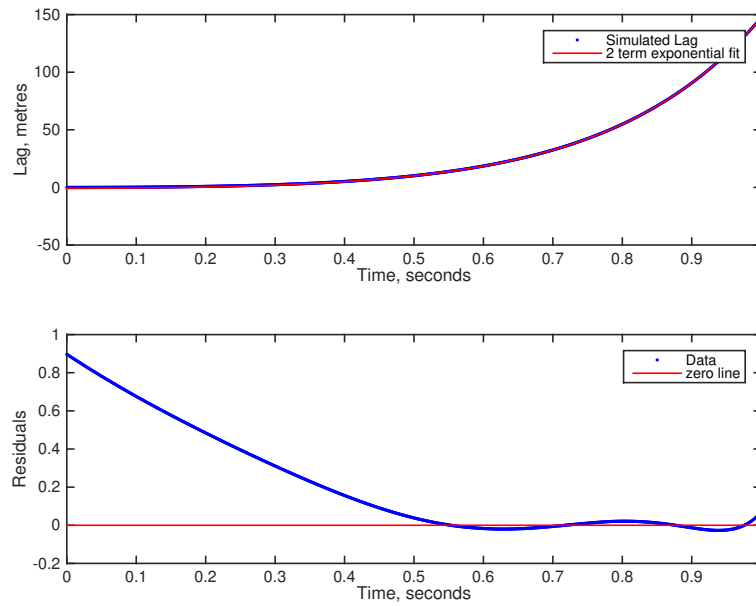
A classically modelled meteor with the following parameters was investigated for fitting: mass of 10^{-5} kg, density of 2000 kg/m^3 , and initial speed of 30 km/s. Because meteors show very little deceleration at the beginning of their ablation, a comparison of fitting the lag from the full curve versus the second half of the lag was done and the results are shown in Figure 4.2.

Fitting only the second half of the lag curve gives smaller residuals (relative to the model lag), and is more accurate at later times, when the meteoroid deceleration is more apparent and easier to fit. The RMSE value for fitting the entire lag profile was 3.4861, and for fitting only the second half of the lag profile was 0.0179. Because meteoroid ablation can last from less than a second to a few seconds, the decision was made to fit the second half of the ablation profile, rather than the last second, or half second. A comparison of the derived deceleration (based on the second derivative of the two-term exponential fit to the lag) to the model deceleration was also done, and is shown in Figure 4.3. When fitting the entire lag profile, the derived deceleration matches the simulated deceleration well towards the beginning of the ablation profile, but the magnitude of the relative error is large towards the end where deceleration is greatest, and which is of greatest interest for finding luminous efficiency. In Figure 4.3b, only the second half of the lag data was fit, but the fit was extended backwards for comparison purposes. The relative percentage error is smaller when the deceleration is greatest, compared to when the entire lag is fit, as shown in Figure 4.3a.

Based on Figures 4.2 and 4.3, a two-term exponential fit $y = ae^{bx} + ce^{dx}$ to the second half

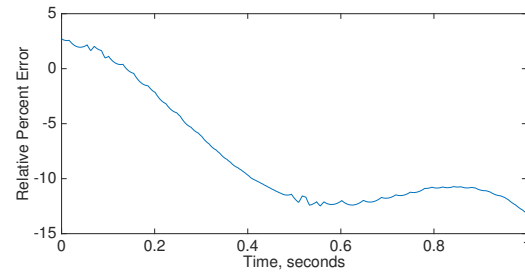
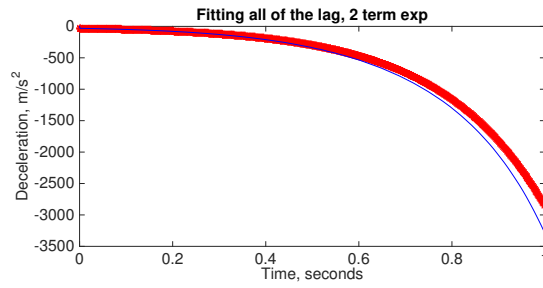


(a)

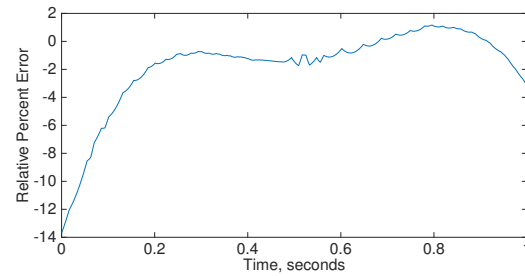
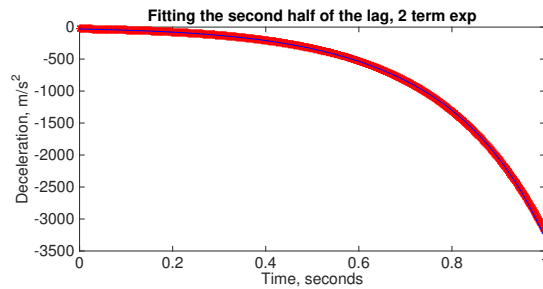


(b)

Figure 4.2: Residual plots for fitting the entire lag (shown in the upper two plots, (a)) compared to fitting only the second half of the lag (shown in the bottom two plots, (b)), with a two-term exponential. For the bottom two plots, the fit has been applied to the entire ablation time period for comparison.



(a)



(b)

Figure 4.3: A comparison of the relative percent error in deceleration, when fitting a two-term exponential to the entire modelled meteoroid lag, versus fitting only the second half of the lag. The red points correspond to the fitted points, and the blue solid line shows the simulated deceleration.

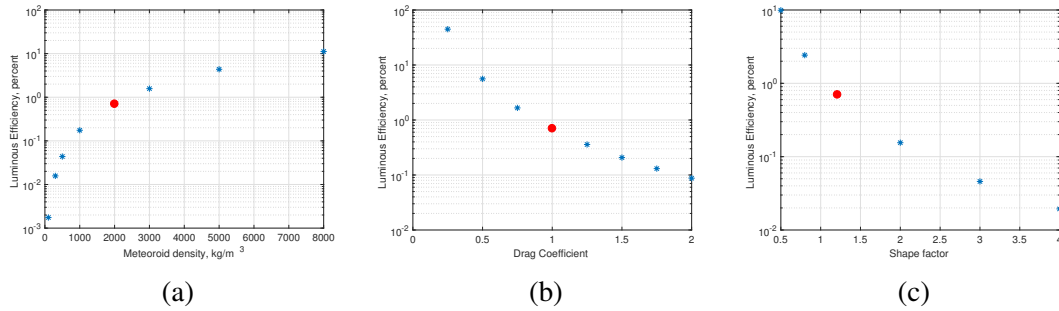


Figure 4.4: The variation of luminous efficiency with the variables assumed to be constants during ablation. The red asterisk in each figure indicates the luminous efficiency value of 0.7% used in the standard event. (a) shows the change in calculated luminous efficiency as a function of meteoroid density – keeping all parameters identical and varying only the meteoroid density can cause the calculated luminous efficiency to range from 0.7% at a density of 2000 kg/m^3 , to 11% at a density of 8000 kg/m^3 . Similar changes are seen in (b) and (c), for drag coefficient and shape factor.

of the lag data is able to visually reproduce a classically modelled meteoroid reasonably well.

To investigate this method for other parameters, a set of simulated meteors were created, each with different parameters (speed, mass, shape factor, meteoroid density, drag coefficient) and tested to see if the luminous efficiency used to simulate the meteor could be extracted from simulated observations with this method. The simulated meteors were generated with the ablation model of Campbell-Brown & Koschny (2004). Calculation of the luminous efficiency was done blind, with no knowledge of the value used in the simulation until the analysis was complete.

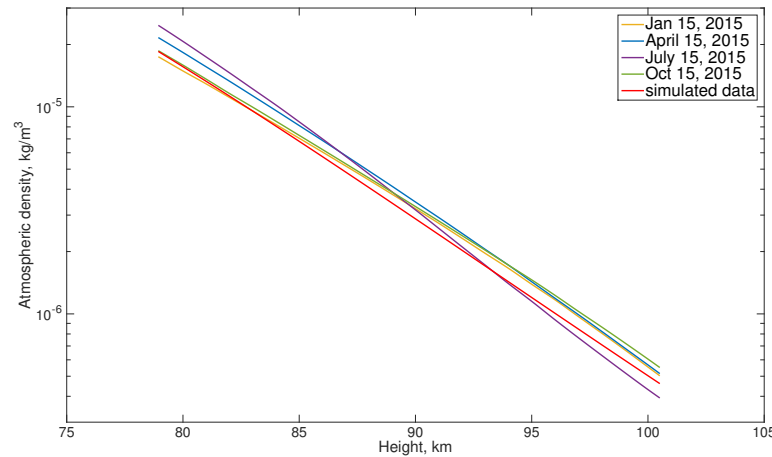
There are three variables in Equations 4.4 and 4.5 that are assumed to be constant with time: the drag coefficient, the shape factor, and the meteoroid density. These variables cannot be measured and values must be assumed. A representative event was simulated with the following parameters: initial speed 30 km/s; shape factor 1.21 (sphere); drag coefficient 1; meteoroid density 2000 kg/m^3 , and a mass of 10^{-5} kg . Any difference between an assumed constant term and the simulated value will change the luminous efficiency by a scaling factor, and the variation and uncertainty in the calculated luminous efficiency (for a range of physically possible values) is shown in Figure 4.4.

A more complicated parameter to deal with is the atmospheric density. Each of the simu-

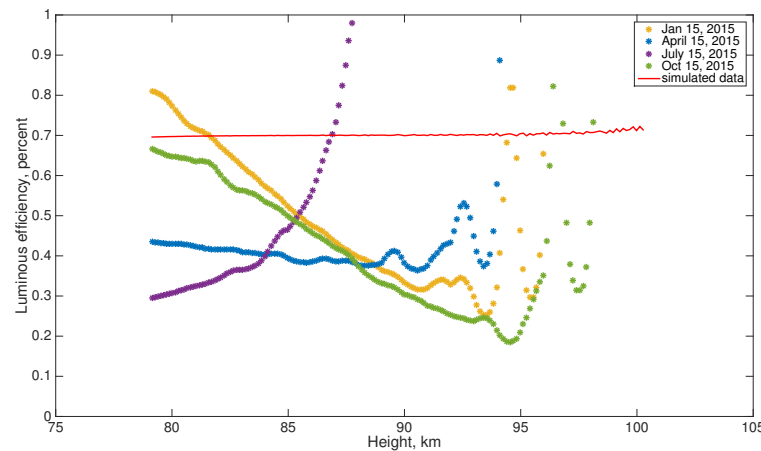
lated meteor events used the same atmospheric density profile, not specific to any date or location. However, with real meteor events, the atmospheric density on that day, at that time and location needs to be used. To investigate the variation in luminous efficiency due to variations in atmospheric density, four days of data (each from a different season) from the NRLMSISE-00 Atmosphere Model (Picone et al., 2002) were compared. The four days of modelled data and the simulated atmospheric density are shown in Figure 4.5a, and the resulting luminous efficiency estimates (keeping everything the same except for the atmospheric density profile) are shown in Figure 4.5b. The resulting luminous efficiency profiles show values that range from 0.2% up to 1%. However, not all luminous efficiency profiles have valid solutions at all heights: when the atmospheric density used in calculating the luminous efficiency is lower than the modelled atmospheric density, we end up with a nonphysical situation where the meteoroid is gaining rather than losing energy as it ablates, and a singularity appears in our luminous efficiency profile.

After investigating our simulated representative meteor to determine how meteoroid density, drag coefficient, shape factor, and atmospheric density model affect our calculated luminous efficiency values, the full parameter space of mass, speed, meteoroid density, zenith angle, and shape factor, was explored. Fifty meteors were simulated for each mass - speed group. The simulated meteors had a mass of 10^{-4} , 10^{-5} , or 10^{-6} kg. The speeds used were 11, 20, 30, 40, 50, 60, and 70 km/s. This meant there were 21 possible groups; however some of the low mass - low speed groups did not produce enough light that they would be detected by the CAMO optical system. This reduced the number of mass - speed groups to 18. The luminous efficiency for each meteor in this set of simulated meteors was 0.7%, constant over time.

To investigate how sensitive our results are to the chosen two-term exponential fit of the meteoroid lag, we analysed each meteor in our mass - speed groups according to our method: the simulated position was used to determine the lag, which was fit by a two-term exponential function. This function was then numerically differentiated (i.e. finite differenced) to determine the deceleration. By using all values (drag coefficient; atmospheric density; velocity; shape



(a) Four days of atmospheric density data taken from the NRLMSISE-00 model, from 2015. The red line is the simulated atmospheric density and was used in the standard event.



(b) The resulting luminous efficiencies for the four different atmospheric density models, and the model from the simulation. All parameters were kept constant except for the atmospheric density model. A luminous efficiency value of 0.7% was used in the standard event. Note that this method is unable to reproduce the exact luminous efficiency used (0.7% constant over time) even when using the same atmospheric density model used in the simulation.

Figure 4.5: Atmospheric density variations over 2015 and their effect on derived luminous efficiency.

Table 4.1: Mean luminous efficiency value (percentage) and standard deviation for each mass - speed group of simulated meteor events. Each group initially contained 50 meteors, but some events were removed from consideration because nonphysical luminous efficiency values were obtained, or due to errors in the simulated data that prevented luminous efficiency values from being determined. The luminous efficiency value used for each simulated meteor was 0.7%.

	10^{-4} kg	10^{-5} kg	10^{-6} kg
11 km/s	0.30 ± 0.11
20 km/s	0.57 ± 0.15	0.51 ± 0.07	...
30 km/s	0.64 ± 0.18	0.84 ± 0.21	0.50 ± 0.14
40 km/s	0.68 ± 0.27	0.86 ± 0.26	0.89 ± 0.33
50 km/s	0.60 ± 0.26	0.80 ± 0.28	0.90 ± 0.29
60 km/s	0.60 ± 0.27	0.76 ± 0.29	0.91 ± 0.32
70 km/s	0.58 ± 0.27	0.69 ± 0.28	0.92 ± 0.34

factor; meteoroid density; intensity) directly from the simulation, with the exception of the determined lag, we were able to see how sensitive our derived luminous efficiency values were to our fit to the meteoroid lag. Our derived luminous efficiencies did not come out as constant values over the ablation due to the sensitivity of this method to small variations in deceleration. The mean and standard deviation for the luminous efficiency of each meteor was determined, and the average of those values in each mass - speed group are given in Table 4.1. Fitting a two-term exponential to the lag, to find the deceleration and the luminous efficiency seems to work for most mass - speed groups. Table 4.1 shows that almost all of the mass - speed groups investigated show luminous efficiency ranges that include the true value of 0.7%. This is not the case for high-mass, low-velocity meteors (11 km/s). In fact, for each mass group, the lowest speed that produces a luminous efficiency profile does not produce a mean luminous efficiency range that includes the value that was used in the simulation.

A comparison of the fitted lag, the corresponding deceleration, and the resulting luminous efficiency profile of a typical event are shown in Figure 4.6. While the simulated lag appears to be fit well by the two-term exponential, the resulting deceleration from the fit deviates from the simulated deceleration. This may be due to numerical temperature fluctuations in the ablation

model. The luminous efficiency derived using only the ablation model output is unable to produce the exact luminous efficiency (constant 0.7% over the ablation period) used in the simulation, as shown in Figure 4.6.

4.4 Discussion

Our method for determining the luminous efficiency uses only the luminous intensity and drag equations, while the ablation model by Campbell-Brown & Koschny (2004) is more sophisticated. Campbell-Brown & Koschny (2004) use the classical form of the drag equation, but their mass loss equation is not classical: they instead use the Knudsen-Langmuir formula with the Clausius-Clapeyron equation to simulate the meteoroid ablating as soon as it begins heating up. When the meteoroid becomes very hot, a spallation term is included (to account for mass loss of pieces). The third differential equation used in the Campbell-Brown & Koschny (2004) model is the temperature equation, which describes the energy gained (through collisions with the atmospheric atoms) and lost (through radiation and evaporation of material).

As seen in the previous figures, uncertainties in each of the variables of Equations 4.4 and 4.5 yield corresponding variances in the computed luminous efficiency. Figures 4.4b and 4.4c were created assuming the drag coefficient and shape factor are constant over the ablation. This is not necessarily true for real meteor events, but for simplicity, was assumed for this work, both in the modelling and analysis. If a real meteor event has a constant drag coefficient or shape factor, but an incorrect value is assumed in the analysis, the difference will be a simple scaling factor; if the value changes over the course of the flight the luminous efficiency will be off by an amount proportional to the difference in the assumed value and the average of the true value.

It is obvious that variations in the atmospheric density over the course of a year (even as much as a factor of two) can change the derived luminous efficiency profile. The solid red line in Figure 4.5b indicates the calculated luminous efficiency using the same atmospheric density model that was used in the simulation. A constant luminous efficiency of 0.7% was used in

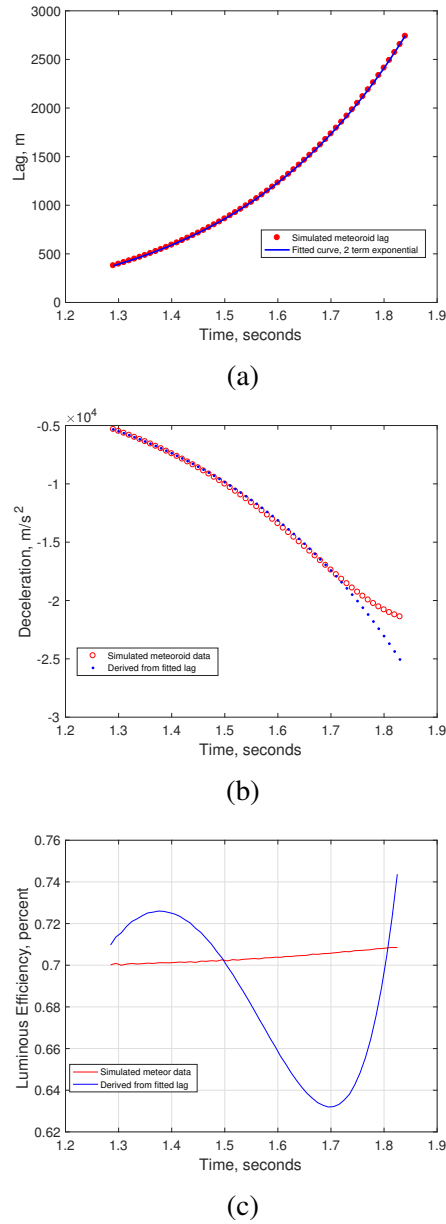


Figure 4.6: A comparison of the output from a simulated meteoroid to fitted equivalents based on a two-term exponential fit to the simulated lag. (a) shows the simulated lag fit with a two-term exponential function. (b) shows in red the deceleration produced by the simulation compared to the blue dots produced by taking the second derivative of the fit to the lag. (c) shows in red, the luminous efficiency determined using only parameters output from the ablation model, while the blue line shows the luminous efficiency derived using identical parameters aside from the deceleration, which was derived from the fit shown in the top panel.

the simulation, but this method is unable to exactly reproduce that: the calculated luminous efficiency is quite close to, but not exactly, a constant 0.7%. We find that small rounding errors in the ablation model cause the small variations we see in the luminous efficiency.

One of the most challenging aspects of this work is determining which functional form to fit to the lag; while more complex functional forms are able to fit the lag better (a combination of an exponential with a polynomial, for example), they do not necessarily provide a better fit to the deceleration, to which the luminous efficiency is very sensitive. Various combinations of exponential fits with polynomials (lag = ae^{bx^2+cx+d} ; lag = $ae^{bx} + cx + d$; lag = $ae^{bx} + e^{cx} + dx + f$; etc.) were tried. Much better results were obtained when the modelled deceleration was fit directly, but this approach will not work for real data. Even very precise observations from CAMO have enough noise in the measured lag that finite differencing produces wildly oscillating decelerations. A smooth fit to the lag is crucial in order to obtain a useful second derivative.

We found that the luminous efficiency calculated by fitting the lag with a two-term exponential did not reproduce the model's constant 0.7% (see Table 4.1). On average, this fitting method does return the correct luminous efficiency, except in the lowest speed groups. In particular, high mass (10^{-4} kg) meteors with initial speeds of 11 km/s had a much lower mean luminous efficiency, because there was poor agreement between the simulated lag and the two-term exponential functional fits by visual inspection. Visual inspection also determined that visually good fits to the lag data may or may not produce a good match to the simulated deceleration.

4.5 Conclusion

An attempt at quantifying the uncertainty in using the classical meteoroid ablation equations to determine the luminous efficiency of meteors has been made. Certain parameters (drag coefficient; meteoroid density; shape factor) were assumed to be constant. The wrong drag

coefficient could produce errors of roughly a factor of 2; the meteoroid density can vary by a factor of 8, but is much more likely to be within a range of a factor of 2; and the shape factor may be different from a sphere, but is not very likely to be as extreme as the end values modelled here, which correspond to an oriented needle and a disk with its largest dimension oriented to the airstream. It's much more likely that the shape factor will be within a factor of 2 of a sphere, and therefore these three parameters together are each a small random effect on the luminous efficiency. The atmospheric density over the course of a year changes by a factor of 2 in the height range that meteors are detected with our optical system, and these variations cause similar factor-of-2 discrepancies in the luminous efficiency computed for simulated events. The possibility of using radar echo decay measurements to verify atmospheric density profiles at the location of the optical cameras is being investigated. Simulated meteor events were studied by examining how different functional fits to the simulated meteoroid lag and derived deceleration affected the luminous efficiency computed for each simulated meteor. A simple two-term exponential fit to the lag provides reasonable decelerations, which in turn provide an average luminous efficiency value close to what was used in the simulation. This method however, was only tested on simulated events that were free of noise. In a future work, we will test the method with noise that approximates the noise observed with the CAMO optical system, and then on actual meteor events recorded by CAMO that show single-body ablation. Measuring luminous efficiencies requires precise measurements and a thorough knowledge of the sources of uncertainty. The high-resolution CAMO tracking system will allow luminous efficiencies to be calculated much more accurately than previous observational attempts, and should be able to reveal the order of magnitude of the luminous efficiency and any trend in luminous efficiency with speed.

Bibliography

- Ayers, W. G., McCrosky, R. E., & Shao, C.-Y. 1970, SAO Special Report, 317
- Becker, D. G., & Friichtenicht, J. F. 1971, *Astrophysical Journal*, 166, 699
- Becker, D. G., & Slattery, J. C. 1973, *Astrophysical Journal*, 186, 1127
- Campbell-Brown, M. D., & Koschny, D. 2004, *Astronomy and Astrophysics*, 418, 751
- Caswell, R. D., McBride, N., & Taylor, A. D. 1995, *International Journal of Impact Engineering*, 17, 139
- Cepplecha, Z., Borovička, J., Elford, W. G., et al. 1998, *Space Science Reviews*, 84, 327
- Cepplecha, Z., & McCrosky, R. E. 1976, *Journal of Geophysical Research*, 81, 6257
- Friichtenicht, J. F., Slattery, J. C., & Tagliaferri, E. 1968, *Astrophysical Journal*, 151, 747
- Jones, W. 1997, *Monthly Notices of the Royal Astronomical Society of Canada*, 288, 995
- Jones, W., & Halliday, I. 2001, *Monthly Notices of the Royal Astronomical Society*, 320, 417
- McCrosky, R. E., & Soberman, R. K. 1963, *Smithsonian Contributions to Astrophysics*, 7, 199
- Picone, J. M., Hedin, A. E., Drob, D. P., & Aikin, A. C. 2002, *Journal of Geophysical Research: Space Physics*, 107, doi:10.1029/2002JA009430
- Subasinghe, D., Campbell-Brown, M. D., & Stokan, E. 2016, *Monthly Notices of the Royal Astronomical Society*, 457, 1289
- Verniani, F. 1965, *Smithsonian Contributions to Astrophysics*, 8, 141
- Weryk, R. J., & Brown, P. G. 2013, *Planetary and Space Science*, 81, 32
- Weryk, R. J., Brown, P. G., Domokos, A., et al. 2008, *Earth Moon and Planets*, 102, 241
- Weryk, R. J., Campbell-Brown, M. D., Wiegert, P. A., et al. 2013, *Icarus*, 225, 614

Chapter 5

Luminous Efficiency -II

A version of this chapter has been accepted for publication as:

Subasinghe, D, & Campbell-Brown, M.D. (2017). *Luminous efficiency estimates of meteors -II. Application to Canadian Automated Meteor Observatory meteor events*. *Astronomical Journal*, in press.

5.1 Introduction

Meteoroid masses are poorly constrained. Various studies have used different experimental and observational techniques in the past to determine meteoroid masses from the light they emit, but results vary by up to two orders of magnitude for a given meteoroid speed. This can have consequences for meteoroid flux estimates, which can affect satellites and spacecraft in orbit around Earth (National Research Council, 2011). Because all small meteoroids ablate completely in the atmosphere, mass estimates need to be made based on observations which are typically less than one second long. There are many unknown parameters which affect calculations of the mass of a meteoroid, such as its shape and density. Assuming the meteoroid is a solid, non-fragmenting object, its mass can be determined with either of a pair of coupled differential equations that describe the mass loss and deceleration of the meteoroid. The luminous

intensity equation (shown in Equation 5.1) allows one to determine the mass of a meteoroid m from the change in its kinetic energy E_k , given the speed v and brightness I .

$$I = -\tau \frac{dE_k}{dt} = -\tau \left(\frac{v^2}{2} \frac{dm}{dt} + mv \frac{dv}{dt} \right) \quad (5.1)$$

A value must be chosen for the proportionality constant τ , the luminous efficiency - a measure of how much of the kinetic energy lost by the meteoroid is used for visible light production. The mass given in Equation 5.1 is the *photometric* mass and includes the mass of all fragments if the meteoroid has broken up. There is a large uncertainty associated with the photometric mass due to the uncertainty in the luminous efficiency.

The deceleration of the meteor is described by Equation 5.2, the drag equation, derived from conservation of momentum.

$$\frac{dv}{dt} = -\frac{\Gamma \rho_{atm} v^2 A}{m^{\frac{1}{3}} \rho_m^{\frac{2}{3}}} \quad (5.2)$$

It provides a second way to determine the meteoroid mass. In this equation, the mass m is the *dynamic* mass and describes the leading (usually largest and brightest) fragment; Γ is the drag coefficient and describes the efficiency of momentum transfer between the atmosphere and meteoroid; ρ_{atm} is the atmospheric density; ρ_m is the meteoroid density; and A is the shape factor, defined as the cross sectional area divided by the object volume to the exponent 2/3. Often, the drag coefficient, the meteoroid density, and the shape factor are assumed to be constant.

Because most meteoroids fragment (Subasinghe et al., 2016), it is more practical to determine the meteoroid mass through the luminous intensity equation, assuming a suitable value can be found for the luminous efficiency.

The uncertainty in the luminous efficiency is large since it may depend on many factors: meteoroid speed and height; meteoroid and atmospheric composition; the spectral response of the detector; and possibly mass (Ceplecha et al., 1998). Whether each factor has an effect, and its effect on the luminous efficiency, is unknown.

The luminous efficiency of meteors has been investigated with numerous methods in the past. A theoretical approach was first taken by Öpik (1933), but has been disregarded by many researchers due to theoretical considerations (such as not knowing how quantum states are populated) (Thomas & Whipple, 1951; Verniani, 1965), and a modern theoretical approach was taken by Jones & Halliday (2001), using excitation cross-sections to predict the light produced (however they assumed that ionised atoms were unavailable for excitation). Verniani (1965) determined the luminous efficiency by equating the dynamic and photometric masses of Super-Schmidt meteors; this study is still the source of luminous efficiencies commonly in use (e.g. Ceplecha & McCrosky, 1976). Verniani (1965) assumed that luminous efficiency is proportional to meteoroid speed to some constant exponent ($\tau \propto v^n$), which his data found to be $n = 1$. Verniani (1965) made an effort to correct his results for fragmentation as it was well known that many of the Super-Schmidt meteors crumbled during ablation, but his calibration for τ is based on a single non-fragmenting asteroidal meteor at low altitude. Lab experiments entail charging and accelerating tiny metal particles in a Van deGraaf generator and observing as they ablate in a low-pressure air chamber. A common difficulty in completing these lab studies is accurately recreating atmospheric compositions and conditions. A number of studies were carried out in the late sixties and early seventies (see Friichtenicht et al., 1968; Becker & Friichtenicht, 1971; Becker & Slattery, 1973), and work in this area has recently been revived, though no results for luminous efficiency have been published yet (Thomas et al., 2016). Another method of determining luminous efficiency is to use artificial meteoroids, in which objects of known mass, composition, and density are launched into the atmosphere and observed as they ablate. This was done by Ayers et al. (1970) for iron and nickel projectiles, at relatively low speeds compared to meteors. Simultaneous radar and optical studies, which use the ionisation efficiency to determine the luminous efficiency, were carried out by Saidov & Simek (1989) (who assumed the optical data was more correct) and Weryk & Brown (2013) (who assumed the radar data was more correct), but the results of the two studies do not agree. A combination of theoretical and lab work was analysed by Hill et al. (2005), and the result

(corrected for bandpass and composition) is presented in Weryk & Brown (2013).

Many of these studies are summarised in Subasinghe et al. (2017), who investigated the precision of using the dynamic mass to determine the photometric mass using meteor data simulated with the ablation model of Campbell-Brown & Koschny (2004). Data with sub-metre scale resolution from the Canadian Automated Meteor Observatory (CAMO) has the potential to redo the work of Verniani much more accurately. In testing the method, we found that uncertainties in the meteoroid density (which cannot be uniquely determined from observations) and atmospheric density account for a factor of two uncertainty, each, in the calculated luminous efficiency. A similar factor of two uncertainty was found when investigating simulated meteors of different masses and speeds. Good agreement was found between the luminous efficiency value used in the simulations and the derived values for all of the mass-speed groups except for the lowest speed group for each of the three masses, which had slightly poorer agreement. Subasinghe et al. (2017) used simulated data free from measurement noise, so the effects of observed noise were not considered, or the possibility that parameters in Equation 5.2 may not be constant over time.

In this work, we continue that investigation by applying a modified method to real meteor events recorded with the high-precision Canadian Automated Meteor Observatory.

5.2 Method Refinement

The simulated data used in Subasinghe et al. (2017) was free of noise, which is unrealistic, but made it easy to evaluate various functional fits to the meteor lag, or distance by which the meteor lags behind an object travelling at constant speed. That study found that a two-term exponential fit to the lag matched the luminous efficiency most closely. The real data used in this study have residuals in position of about 2 m: we added scatter of this order to the positions generated by the ablation model, and again tried to recover the luminous efficiency used in the model. A simplification from the two-term exponential ($\text{lag} = ae^{bx} + ce^{dx}$) to a single-term

exponential ($\text{lag} = ae^{bx}$) was necessary, because when noise was added to the model the two-term exponential produced unphysical values of the speed and deceleration. A single-term exponential is a relatively poor fit for the full lag curve, but does well when fitting only the last half of the curve, which is where the deceleration is high enough to calculate a meaningful luminous efficiency. The final method used in this work fits a single-term exponential to the second half of the meteor lag data, and uses the fit parameters to determine the speed and deceleration profiles used for the luminous efficiency determination.

To illustrate the process, we present a standard, non-fragmenting simulated event (with the parameters given in Table 5.1) run through our method, and the resulting luminous efficiency profile. The event was simulated using the meteoroid ablation model of Campbell-Brown & Koschny (2004) with an assumed luminous efficiency of 0.7%, constant over the entire ablation time. The derived luminous efficiency was calculated using Equations 4.1 and 4.2, with values for the drag coefficient Γ , meteoroid density ρ_m , shape factor A , and atmospheric density ρ_{am} coming from the simulation (for real events, these will be estimates except for the atmospheric density which will come from a model). A single-term exponential (given in Equation 5.3) was fit to the second half of the lag data of the standard event, and the fitted parameters were $a = 1.112$ and $b = 6.84$.

$$\text{lag} = ae^{bx} \tag{5.3}$$

The speed and deceleration values are based on these fitted parameters. The fit to the lag is shown in Figure 5.1, and the corresponding speed and deceleration plots are shown in Figure 5.2, with the simulated values plotted against the curves based on the fit parameters from the lag.

Using the speed and deceleration profiles based on the lag fit, and all other values taken from the simulation, we find the luminous efficiency profile shown in Figure 5.3. Recall that in the simulation, a constant luminous efficiency of 0.7% was used. Figure 5.3 shows two profiles: the blue asterisks show the luminous efficiency determined using all the simulation

Table 5.1: Standard event parameters. These are the parameters used in the Campbell-Brown & Koschny (2004) ablation model to simulate our standard event for testing purposes.

Initial Speed (km/s)	Initial Mass (kg)	Shape Factor	Drag Coefficient	Meteoroid Density (kg/m ³)	Zenith Angle (degrees)
30	10 ⁻⁵	1.21	1	2000	30

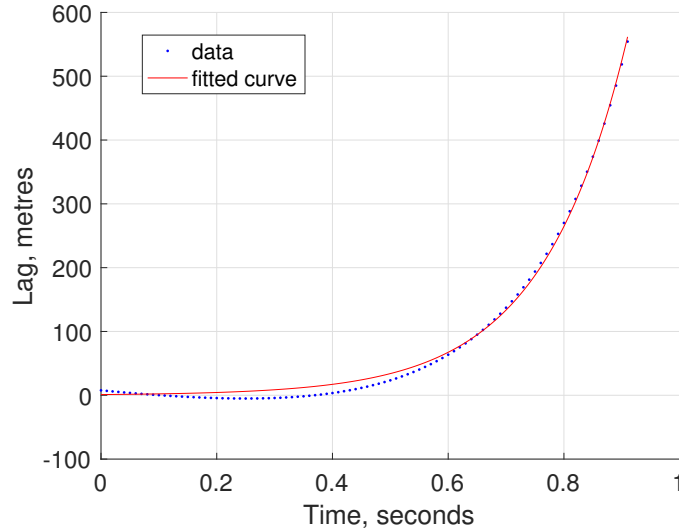


Figure 5.1: The second half of the lag (from 0.45 seconds onward) was fit with a single-term exponential. The fit has been plotted over the entire lag profile (shown as blue dots). The negative lag points are due to the method used to determine the lag – if we fit fewer than 50% of the meteor position points to determine the initial speed, there would be no negative lag values.

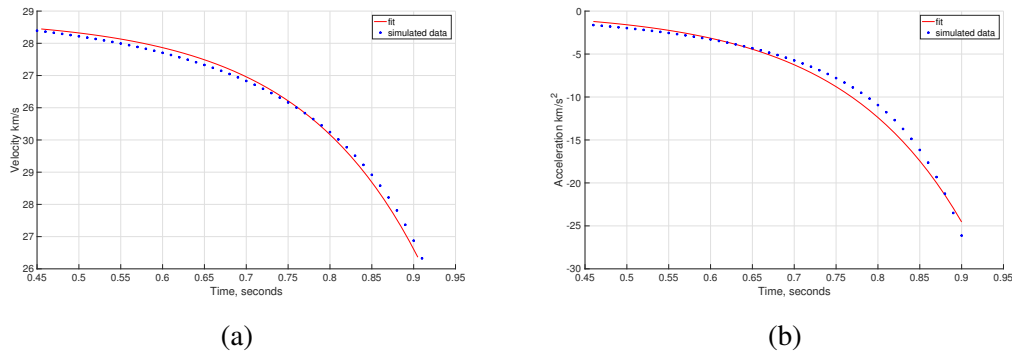


Figure 5.2: The speed profile of the standard simulated event, with the simulated data shown as blue asterisks, and the velocity based on the lag fit shown as a solid red line is on the left. On the right is the deceleration profile for both the simulated data and the data based on the lag fit, shown with blue asterisks and a solid red line respectively. In both plots, only the second half of the simulated meteor data is shown, as that was all that was fit by the single-term exponential.

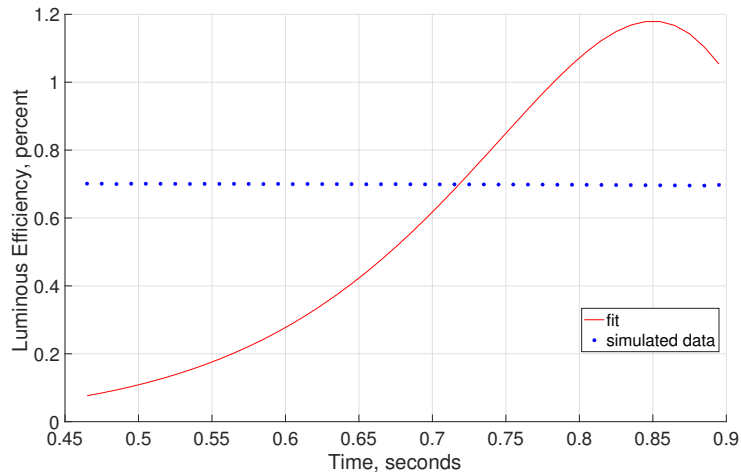


Figure 5.3: The luminous efficiency profile for the simulated meteor based on the simulated speed and deceleration profiles is shown with blue asterisks, and the luminous efficiency profile based on the speed and deceleration derived from the fitted lag is shown with a solid red line. To quantify the luminous efficiency for each profile, the mean value was used, based on the second half of the meteoroid ablation data.

parameters, including the simulated deceleration and simulated speed. The red line shows the luminous efficiency found using the speed and deceleration profiles based on the single-term exponential fit to the lag. The resulting profile from the simulated data is not able to perfectly reproduce the constant 0.7% luminous efficiency used in the simulation due to the simplicity of this method compared to the physics in the ablation model that was used. The average luminous efficiency of the profile based on the fitted lag is 0.60%, and 0.70% for the profile resulting from using all the simulated data. Subasinghe et al. (2017) explored the deviation from an assumed luminous efficiency due to different functional fits and each parameter in the drag and luminous intensity equations.

5.3 Equipment and Data Reduction

5.3.1 Equipment

The meteor events in this study were recorded by the Canadian Automated Meteor Observatory (CAMO), which is located in Ontario, Canada. CAMO is a two-station image intensified

optical system which records meteors nightly, under appropriate weather conditions. One station is located in Tavistock, Ontario, Canada (43.265°N , 80.772°W), and the other is about 45 km away in Elginfield, Ontario, Canada (43.193°N , 81.316°W). For our work we are using the guided system which is a two-part system, consisting of a wide-field camera (with a field of view of 28°) and a narrow-field camera (1.5° FOV). The wide-field camera detects meteors in real time with the All Sky and Guided Automatic Realtime Detection (ASGARD) software (Weryk et al., 2008) which guides a pair of mirrors to direct the meteor light into the narrow-field camera. The cameras run at different frame rates (80 and 110 fps for the wide-field and narrow-field, respectively), and each camera is used for different science goals. The wide-field camera typically captures the full meteoroid ablation profile, which allows for light curve calculation, as well as orbit determination. The narrow-field camera does not capture the entire meteoroid ablation profile as collection only begins after the meteor has been detected in the wide-field camera over 4 to 7 frames, and it typically takes a few frames of observation in the narrow-field camera before the meteor is tracked smoothly by the mirrors. However, the narrow-field camera is a high-resolution camera able to resolve up to 3 m per pixel at 100 km range, which allows the fragmentation behaviour of the object to be observed. These observations allow us to find objects that show single-body ablation, which is required when using the classical ablation equations, and to measure the deceleration very precisely. More details about the cameras can be found in Weryk et al. (2013).

5.3.2 Data Reduction

CAMO records meteors each night if certain sky conditions are met, and has been in operation since 2007 (Weryk et al., 2013). This large database of meteors was searched for meteor events recorded at both stations in the narrow-field cameras that showed either single-body ablation, or a leading fragment with no wake. The classical meteoroid ablation equations apply to objects that are solid, single-bodies that do not fragment. Any object which does fragment will have a smaller dynamic mass (this is the mass of the largest and brightest fragment) than the

photometric mass (this is the mass of the entire meteoroid), and therefore an artificially large luminous efficiency. Despite CAMO having recorded thousands of meteor events, finding meteors that showed next to no fragmentation proved to be a difficult task, as more than 90% of CAMO meteors show some form of fragmentation in the form of wake (Subasinghe et al., 2016). A meteor with a leading fragment is a special case where a fragment of the main body decelerates less than the others, and this piece shows little to no fragmentation. Examples of these non-fragmenting morphologies are shown in Figure 5.4. Meteors that met the requirements of showing single-body ablation (either the entire body, or a leading fragment) were then analysed with two software packages: METAL (Weryk & Brown, 2012) and mirfit.

METAL allows for orbit determination and light curve analysis of a meteor in the wide-field camera. Astrometric and photometric plates are computed using a minimum of 10 stars from each station: each stellar pixel centroid and brightness are calibrated against those from the SKY2000v4 catalogue. Once this is complete, the head of the meteor is picked in each frame, for both stations, for which the entire meteor is visible, and a trajectory solution is determined using an implementation of the least squares method (Borovicka, 1990) called MILIG. By masking out pixels containing light from the meteor, the meteor apparent magnitude can be determined, and converted to an absolute magnitude using the photometric calibration plate and meteor range.

The software package mirfit allows video observations taken with the high-resolution narrow-field cameras to be analysed. Because the field of view is so small (1.5°) compared to video taken with the wide-field cameras (28°), stellar astrometric plates cannot be done due to the lack of visible stars; in addition, the field of view is moving during the observations. To determine meteor positions in the narrow-field cameras, the mirror positions need to be taken into account. These are recorded every 0.5 ms, so the position of the centre of the field at the beginning of the exposure can be interpolated. Then, the distance (or offset) between the position of the meteor on the narrow-field image and the image centre is determined, and converted into an offset in mirror encoder coordinates. This offset is then added to the mirror position at



(a) Leading fragment



(b) Single-body ablation

Figure 5.4: Examples of a meteor with a leading fragment and another showing single-body ablation. Each image is from an individual frame, with the meteor cropped, rotated, and stacked such that time increases downwards. The images are inverted to show detail. The image on the left has the leading fragment centered (clearly showing the deceleration of the rest of the body behind it), while the meteor on the right has the entire object centered. The 100 m scale bar for the leading fragment example is for a height of 80 km, and for the single-body example, is for a height of 85 km.

that time, and mapped onto the celestial sphere. This is done using two plates: a scale plate which determines the offset and converts pixel position to mirror encoder coordinates; and an exact plate which maps the mirror encoder coordinates into celestial coordinates. A calibration for the exact plate is done at the beginning of any night's observations, and every two hours through the night.

If the program that creates the exact plate calibration makes an error, for example by attempting to calibrate a star in the field of view with a different star in the catalogue, errors with the plates can occur, so plates are verified prior to meteor analysis, since bad calibration data cannot be replaced. Stars visible in the field of view will be trailed across each frame, with the predicted location of the initial position indicated by the software. If the plates are functioning correctly, the predicted star positions will not drift across the star trails, but will have the same position relative to the star streak in each frame. The method we are using to determine meteor luminous efficiency is very sensitive to the position measurements (as deceleration values are needed), which means for the most reliable results, we should only use meteor events with accurate plates. The number of useful meteors is then restricted not only to the few meteors which show no fragmentation, but to those non-fragmenting meteors which also have accurate plates. Meteor events that pass both of these requirements are then analysed in mirfit. The meteor astrometry is done through centroiding for each frame, in both stations; centroiding works particularly well on meteors with no visible wake. Photometry was also done for each meteor. mirfit is not able to calibrate the meteor brightness because of the lack of calibration stars in the field, but can calculate the log of the sum of the brightness of the meteor pixels, which is proportional to the meteor magnitude. This relative light curve is then calibrated using the photometry for the meteor in the wide-field camera.

Data reduction was completed for thirteen meteors showing a leading fragment, and two meteors showing single-body ablation. A single frame from each meteor is shown in Figure 5.5. Five fragmenting meteors were also analysed for comparison, though the luminous efficiencies calculated for those meteors must be upper limits: the dynamic masses will be less than the

photometric masses, leading to larger derived luminous efficiency values. The mirfit analysis provides high-precision meteor positions, with an average random position uncertainty of 1.6 m for the fifteen non-fragmenting events (with a maximum uncertainty of 2.5 m, and a minimum of 0.9 m). The position data was turned into lag values (i.e. the distance the meteoroid would fall behind an identical object moving with a constant speed). The speed used was the initial meteoroid speed, found by fitting the first half of the distance-time data, though the exact value is not important since only derivatives of the lag are used. The second half of this lag was fit by a single-term exponential function, and the derivatives were used for the speed and deceleration profiles. Typical values were used for the drag coefficient ($\Gamma = 1$); shape factor ($A = 1.21$); meteoroid density (values taken from either Kikwaya et al. (2011) or Kikwaya Eluo (2011)); and the atmospheric density profile was taken for the event date from the NRLMSISE-00 Atmosphere model (Picone et al., 2002). An analysis of how sensitive this method is to each of the parameters can be found in Subasinghe et al. (2017).

5.4 Results

5.4.1 Noise analysis

Prior to evaluating the luminous efficiency for each of our fifteen events, we investigated the effect that noise has on our method. In Subasinghe et al. (2017) we investigated a set of simulated meteor events that covered the entire physical phase space of mass, speed, meteoroid density, zenith angle, and shape factor. There were 21 mass-speed groups (three different masses and seven different meteor speeds), each of which had 50 possible meteors (all combinations of five possible meteoroid densities, two possible zenith angles, and five possible shape factor values; the possible values are given in Table 5.2); however, not all meteors produced enough light that the CAMO optical system would detect it. This left 18 mass-speed groups, with up to 50 meteors, to study. Each meteor was simulated with a luminous efficiency of 0.7%, constant over time. Five uncertainty levels (standard deviations of 0.1, 0.5, 1, 2, 5 m) were selected to

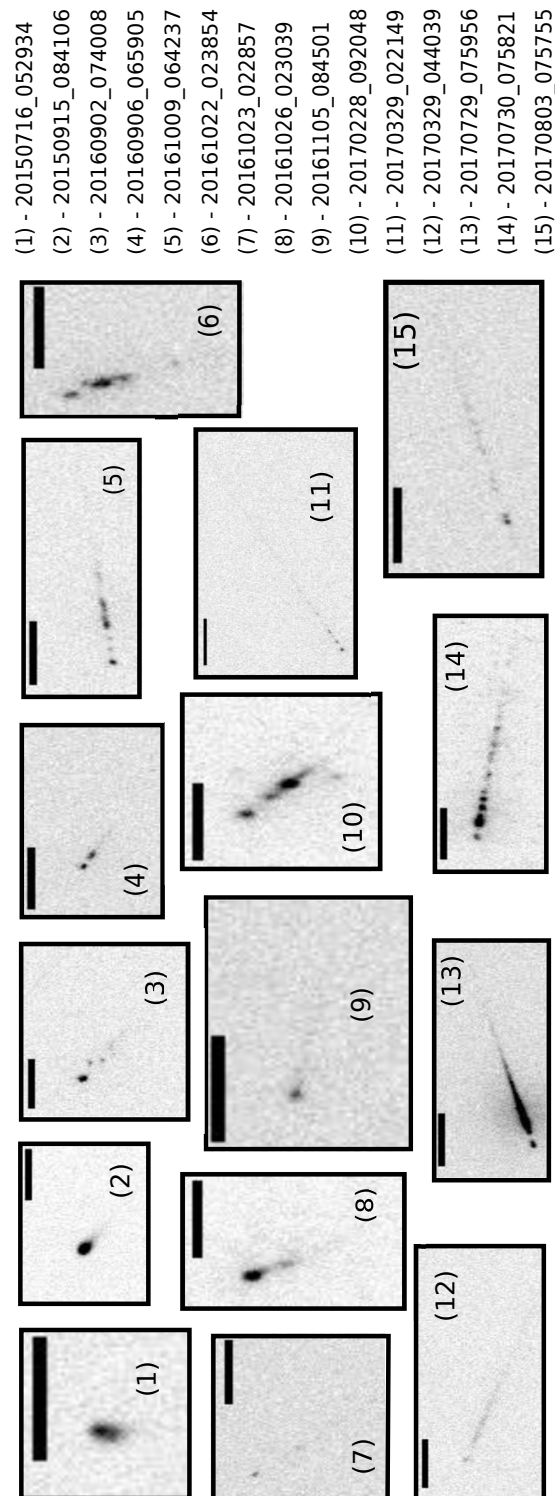


Figure 5.5: A single frame from the analysed meteor events. The scale bar in each frame corresponds to 100 m. In frames showing multiple fragments, the fragment of interest is the front most one. Images have been inverted to show detail.

Table 5.2: Parameters used to simulate meteors.

Mass (kg)	Speed (km/s)	Meteoroid density (kg/m ³)	Zenith angle (degrees)	Shape factor
10 ⁻⁴	11	1000	30	0.5
10 ⁻⁵	20	2000	60	0.8
10 ⁻⁶	30	3000	...	1.21
...	40	5000	...	2
...	50	8000	...	4
...	60
...	70

showcase the effect that position precision would have on the results, with the 2 m uncertainty being closest to our measured uncertainties. Noise was randomly added 500 times at each uncertainty level to each meteor in the 18 mass-speed groups, and the luminous efficiency was calculated. The mean value of each profile was found, and the 500 mean luminous efficiency values for each event were averaged. These results are presented in Figure 5.6, separated by mass.

5.4.2 Atmospheric density variations

As an extension to the work presented in Subasinghe et al. (2017), we investigated the influence of atmospheric density changes on derived luminous efficiency values. It was found that changes in the model atmospheric density profiles over the course of one year could affect derived luminous efficiency values by at most a factor of two (with the model atmospheric density profiles varying at different heights by at most a factor of 2). Figure 5.7 shows in the top panel how seasonal variations over the course of 2016 would affect the derived luminous efficiency profile of our standard event. Everything was identical in each run except for the atmospheric profile used; in the standard profile for comparison, the atmospheric density profile used in the simulation was used to find luminous efficiency. All other values (meteoroid density and so

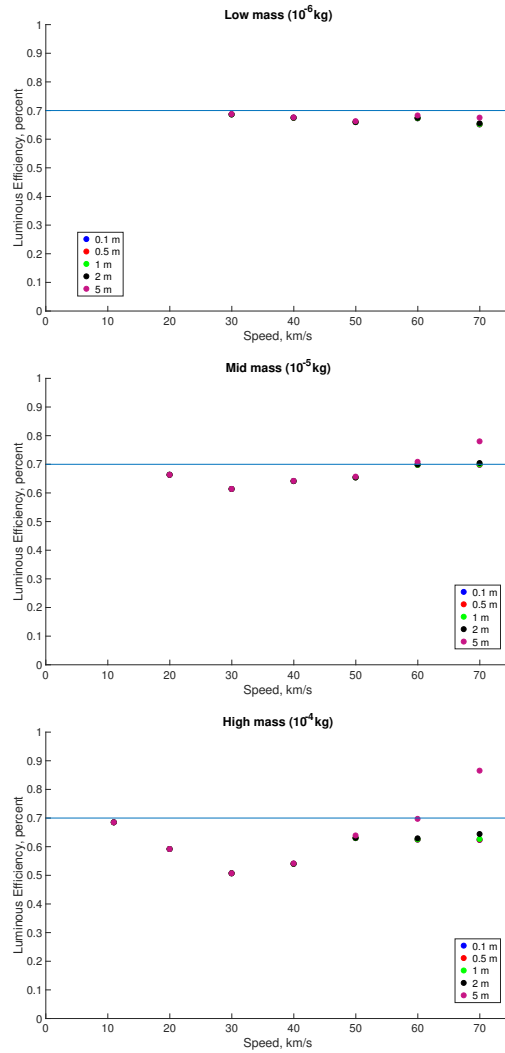


Figure 5.6: Different amounts of uncertainty were added to simulated meteor position picks, and the resulting derived averaged luminous efficiencies are shown for three different mass groups. Each meteor was simulated with a constant luminous efficiency of 0.7%, shown as a solid blue line. The different coloured points indicate the position uncertainty.

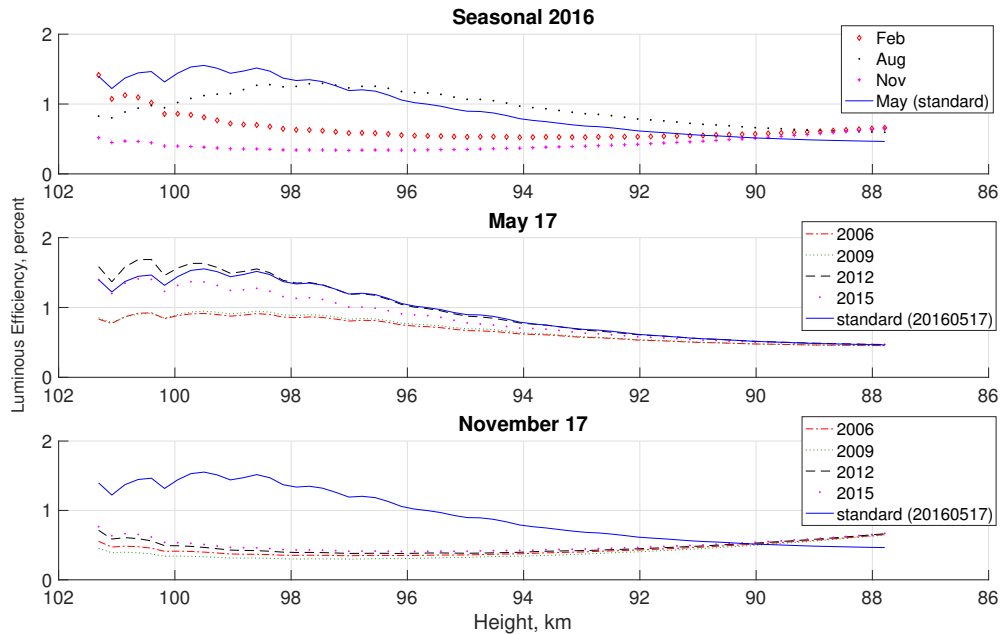


Figure 5.7: Atmospheric density variations on a simulated meteor event. The top panel shows seasonal changes over 2016. The middle and bottom panels show solar cycle changes. All values for the derived luminous efficiency profiles came from the simulation, except for the seasonal and yearly atmospheric density models. There are minimal differences in derived luminous efficiency profiles over the solar cycle, which may be due to a lack of data at meteoroid ablation heights.

on) matched those used in the simulation. The middle and bottom panels instead show how the solar cycle affects the luminous efficiency for two dates over the course of 2006 - 2012. At the time of writing, the NRLMSISE-00 model provides data up to April 17 2017. However, some of our meteor events were recorded in July and August 2017. The results of Figure 5.7 indicate that atmospheric density data from the same day but different years will result in very similar derived luminous efficiency results: the May 17 derived mean luminous efficiency results vary at most by a factor of 1.4, and the Nov 17 derived mean luminous efficiency values vary at most by a factor of 1.3. Therefore, for our meteor events recorded in July and August 2017, atmospheric density profiles from the previous year were used.

5.4.3 Photometry calibration

When determining the luminous efficiency with the drag and luminous intensity equations, the meteoroid brightness is needed, as seen in Equation 4.1. This information can be obtained from both the narrow-field and wide-field cameras; however, if the fragment of interest is a leading fragment, the wide-field photometry will include the brightness of all fragments (the resolution is not high enough to separate the fragment brightness from the rest of the object). Thus, the narrow-field photometry is necessary for determining the luminous efficiency of the relevant fragment only. The method of obtaining the meteor photometry from both the wide-field and narrow-field cameras is described below.

The calibration of meteor photometry for meteors observed with the CAMO guided wide-field system was discussed in Weryk et al. (2013). As we are using positions derived from the narrow-field analysis, we investigated the possibility of calibrating the narrow-field meteor photometry with stars observed in the narrow-field camera, to eliminate the need for the wide-field cameras in this work. In METAL, pixels are masked out in each frame to select the light from the meteor (giving the instrumental apparent magnitude), and converted to the absolute magnitude using both the previously determined photometric plate and range to the meteor in each frame. The uncertainty in METAL photometry is close to 0.2 mag (Subasinghe et al., 2016). Similarly, in mirfit, pixels can be masked out in each frame to give the instrumental apparent magnitude from the log of the sum of the pixel values (lsp); however, there is no photometric plate due to the small number of visible stars in the small field of view.

To calibrate the narrow-field instrumental apparent magnitudes, we compared those log-sum-pixel values to the absolute magnitudes determined in the wide-field observations and used them as a calibration to determine the absolute magnitude of the meteor in the narrow-field camera. To verify these narrow-field absolute magnitudes, we investigated the method of calibrating against stars visible in the narrow-field camera, in spite of their small number.

Photometry calibrations were investigated for seven of the meteor events in our dataset (four events had no visible stars, and nine events were added after this investigation was com-

pleted). Each investigated event had at least one visible star, but no more than two – more than two visible stars occurred multiple times, but stars were eliminated from the study if they were only visible for a few frames, or if they were binary stars. The average instrumental apparent magnitude of each star was determined, and the offset from the SKY2000v4 catalogue R magnitude was found. This offset was applied to the meteor lsp values to correct them to apparent magnitude values. If a station had two visible stars the average offset was applied to the meteor log sum pixel values to correct them to an apparent magnitude. The average difference between the mirfit calibrated photometry and the METAL calibrated photometry was -0.3098 and -0.2666 magnitude, for Tavistock and Elginfield respectively. For our luminous efficiency analysis, we used the METAL calibrations simply because there are many more stars to calibrate against, but our result here indicates that there is only a minor difference between the METAL and mirfit brightness calibrations which are typically based on two stars.

Equation 4.1 uses the meteor intensity, rather than the meteor magnitude. To convert between magnitude and intensity, we use the results of Weryk & Brown (2013) who determined that for the Gen III image intensified video cameras we are using, a zero magnitude meteor emits 820 W.

5.4.4 Meteoroid density

One parameter we have control over in our analysis is the initial meteoroid density. In our study we assume for simplicity that this density is constant over time. The density for each meteoroid was determined using the results from Kikwaya et al. (2011) and Kikwaya Eluo (2011), in which meteoroid densities were found after searching the entire parameter space in an attempt to match each meteor deceleration and light curve shape using the ablation model of Campbell-Brown & Koschny (2004). Kikwaya et al. (2011) used the classification of Borovička et al. (2005), which considers meteoroid physical composition, in their meteoroid density analysis, and uses not only the meteoroid Tisserand parameter, but individual orbital elements to help classify objects. The Tisserand parameter with respect to Jupiter is based on an object's orbital

Table 5.3: Meteoroid densities based on Tisserand parameter values. The first two columns are from Borovička et al. (2005), and the associated meteoroid densities are based on work from Kikwaya Eluo (2011) and Kikwaya et al. (2011).

Orbit type	Orbital element and Tisserand parameter	Density (kg/m ³)
Sun-approaching	$q < 0.2$ AU	3206
Ecliptic shower	e.g. Northern Iota Aquariids	3200
Halley type	$T_J < 2$ or $2 < T_J < 3$ and $i > 45^\circ$	890
Jupiter family	$2 < T_J < 3$ and $i < 45^\circ$ and $Q > 4.5$ AU	3190
Asteroidal-chondritic	$T_J > 3$ or $Q < 4.5$ AU	4200

elements, and is given by:

$$T_J = \frac{a_J}{a} + 2 \sqrt{\frac{a}{a_J} (1 - e^2) \cos(i)} \quad (5.4)$$

Where a , e , and i are the semimajor axis, eccentricity, and inclination of the meteoroid, respectively, and a subscript J indicates an orbital element belonging to Jupiter. A Tisserand parameter greater than 3 suggests that an object has an asteroidal orbit; between 2 and 3 is associated with Jupiter-family comets; and T_J less than 2 describes a Halley-type orbit.

The meteoroid orbit classification described by Borovička et al. (2005) and the associated meteoroid densities from Kikwaya et al. (2011) used in this work is given in Table 5.3 (note: q is the perihelion distance and Q is the aphelion distance).

In our set of non-fragmenting meteor events we have eight meteors with Halley type orbits, five with Jupiter family orbits, and two with asteroidal-chondritic orbits. Of our five fragmenting meteor events, two are Halley-type, one has a Jupiter family orbit, and two have asteroidal-chondritic orbits. Kikwaya et al. (2011) give a mean density for objects with Jupiter family orbits and objects with asteroidal-chondritic orbits. They give a minimum and maximum density for objects on Halley type orbits: the mean density for Halley type objects comes from the raw data in Kikwaya Eluo (2011).

5.4.5 Error analysis

In Table 5.4 we present the luminous efficiency values determined for each of the twenty events. Each luminous efficiency value is presented with an associated uncertainty which takes into account the uncertainty from assuming the drag coefficient, meteoroid density, shape factor, and random errors in the position. A random error of up to half a pixel was added to each analysed position pick, one hundred times. Half a pixel corresponds to approximately 2 m at a range of 110 km, which was found to be closest to the average error in our measured positions. The entire parameter space of drag coefficient, meteoroid density, and shape factor was then tested with each of those one hundred variations, and the luminous efficiency was found. Table 5.4 presents the mean luminous efficiency and corresponding standard deviation. The range of drag coefficient values tested was from 0.8 to 1.2 (with 1.0 being an inelastic collision); shape factor varied from 0.71 to 1.71 (with 1.21 being a sphere); and meteoroid density taken from Kikwaya et al. (2011) with an uncertainty of $\pm 500 \text{ kg/m}^3$. The distribution of luminous efficiency values spanning the entire parameter space was more skewed than normal, however Table 5.4 presents the mean, median, and standard deviation values.

5.4.6 Meteor event 20161009_064237

In Figure 5.8 we present the analysis of one event, from fitting the lag, to the final determined luminous efficiency profile. To reduce the noise that comes from finite differencing the values, we smoothed the speed and deceleration values by finite differencing over larger separations. Despite this, there is still considerable scatter in the speed and deceleration points, emphasising the importance of both precise position measurements for this work, and using a suitable fit for the meteor lag. The lag fit parameters for this event are $a = 0.8908$ and $b = 23.82$, and the following parameters were assumed: meteoroid density of 3190 kg/m^3 ; drag coefficient of 1; and shape factor of 1.21. The fitted parameters are based on the original data analysis: they do not take into account searching the parameter space, or the uncertainty of half a pixel in position. The average luminous efficiency over the second half of this meteoroid's ablation

Table 5.4: Parameters for the twenty meteor events analysed for this work. The initial speed is based on the entire meteoroid ablation profile, and not just the second half of the meteor data. The orbit classification and meteoroid density determination is described in Section 5.4.4. The Origin column labels the meteors as either sporadic (SPO), or by their meteor shower code. The initial mass and luminous efficiency values were found after searching the entire phase space of meteoroid density, shape factor, and drag coefficient, and are mean values unless specified. Under NOTE, events with an asterisk describe meteors that were found to be sensitive to position picks, and SB refers to meteors showing single-body ablation, while LF describes leading fragment events, and F describes those that show long distinct trails.

Event	v_i (km/s)	T_J	Orbit type	Origin	ρ_m (kg/m ³)	m_i (10 ⁻⁶ kg)	τ (mean) (per cent)	τ (median) (per cent)	Note
20160902_074008	68.9	-0.2	HT	SPO	890	0.81±1.18	0.30±0.43	0.15	LF
20160906_065905	62.4	-0.8	HT	SPO	890	56.86±470.80	0.08±0.20	0.02	LF
20161009_064237	32.5	2.7	JF	SPO	3190	3.47±3.16	0.10±0.11	0.06	LF
20161022_023854	54.0	1.2	HT	SPO	890	1.94±3.06	0.22±0.33	0.11	LF
20161023_022857	39.9	1	HT	CTA	890	17.41±27.58	0.05±0.07	0.02	LF
20161026_023039	25.4	3.8	AC	SPO	4200	0.03±0.03	18.71±9.68	18.70	LF*
20161105_084501	65.2	-0.6	HT	ORI	890	1.31±1.93	0.13±0.19	0.06	LF
20170228_092048	63.5	1.1	HT	SPO	890	13.73±97.20	0.04±0.06	0.01	LF
20170329_022149	13.0	3.1	AC	SPO	4200	17.89±22.97	0.10±0.14	0.06	LF
20170329_044039	26.7	2.9	JF	SPO	3190	0.22±0.22	0.28±0.34	0.16	LF
20170729_075956	42.2	2.2	JF	SDA	3190	13.73±26.24	0.28±0.31	0.16	LF
20170730_075821	41.0	2.4	JF	SDA	3190	0.28±0.26	0.39±0.44	0.23	LF
20170803_075755	40.2	2.4	JF	SDA	3190	0.07±0.06	2.77±3.01	1.62	LF*
20150716_052934	41.7	2.9	HT	SPO	890	0.65±1.95	0.85±1.35	0.38	SB
20150915_084106	68.8	0.6	HT	SPO	890	0.80±7.62	27.84±22.38	22.66	SB*
20160709_042521	15.3	3.0	JF	SPO	3190	0.03±0.03	47.27±15.71	43.34	F*
20160710_065147	41.6	1.9	HT	NZC	890	1.15±1.66	6.18±4.42	5.65	F*
20160803_073937	19.3	3.5	AC	SPO	4200	0.16±0.14	31.98±9.59	29.88	F*
20161105_030709	28.8	3.2	AC	NTA	4200	0.02±0.01	39.10±15.61	33.94	F
20170323_070356	57.0	3.0	HT	SPO	890	0.68±0.98	9.35±8.71	6.45	F*

was $0.101 \pm 0.111\%$.

5.4.7 Final Meteor results

The calculated luminous efficiency values for each meteor event analysed, as a function of initial speed, are presented in Figure 5.9, plotted over a few past studies for comparison. The error bars are based on searching the entire parameter space of appropriate meteoroid density, drag coefficient, and shape factor, and the downward arrows indicate that the determined luminous efficiency values are upper limits (due to fragmentation), or that the lower bound of the luminous efficiency is less than zero. Some meteor events moved out of the narrow-field camera's field of view at one station: these events are plotted as either blue squares or red diamonds in Figure 5.9. The single-term exponential was fit to single station data rather than two station data in those cases; however, data from both stations was used to calculate the meteoroid trajectory.

5.4.8 Luminous Efficiency and mass

It has been suggested that while the calculated meteoroid mass depends on luminous efficiency, the luminous efficiency may depend on mass according to fireball studies (Halliday et al., 1981; Ceplecha et al., 1998). To investigate this, Figure 5.10 illustrates the relationship between the average initial mass and luminous efficiency of each meteor. It is worth noting that these initial masses are smaller than the true initial mass of the meteoroid: this is the dynamic mass at the beginning of the second half of the trajectory, and in some cases the mass of the leading fragment instead of the whole meteoroid. As with the above results, these initial masses are an average determined after searching through the entire parameter space. The meteor events are coloured by initial speed.

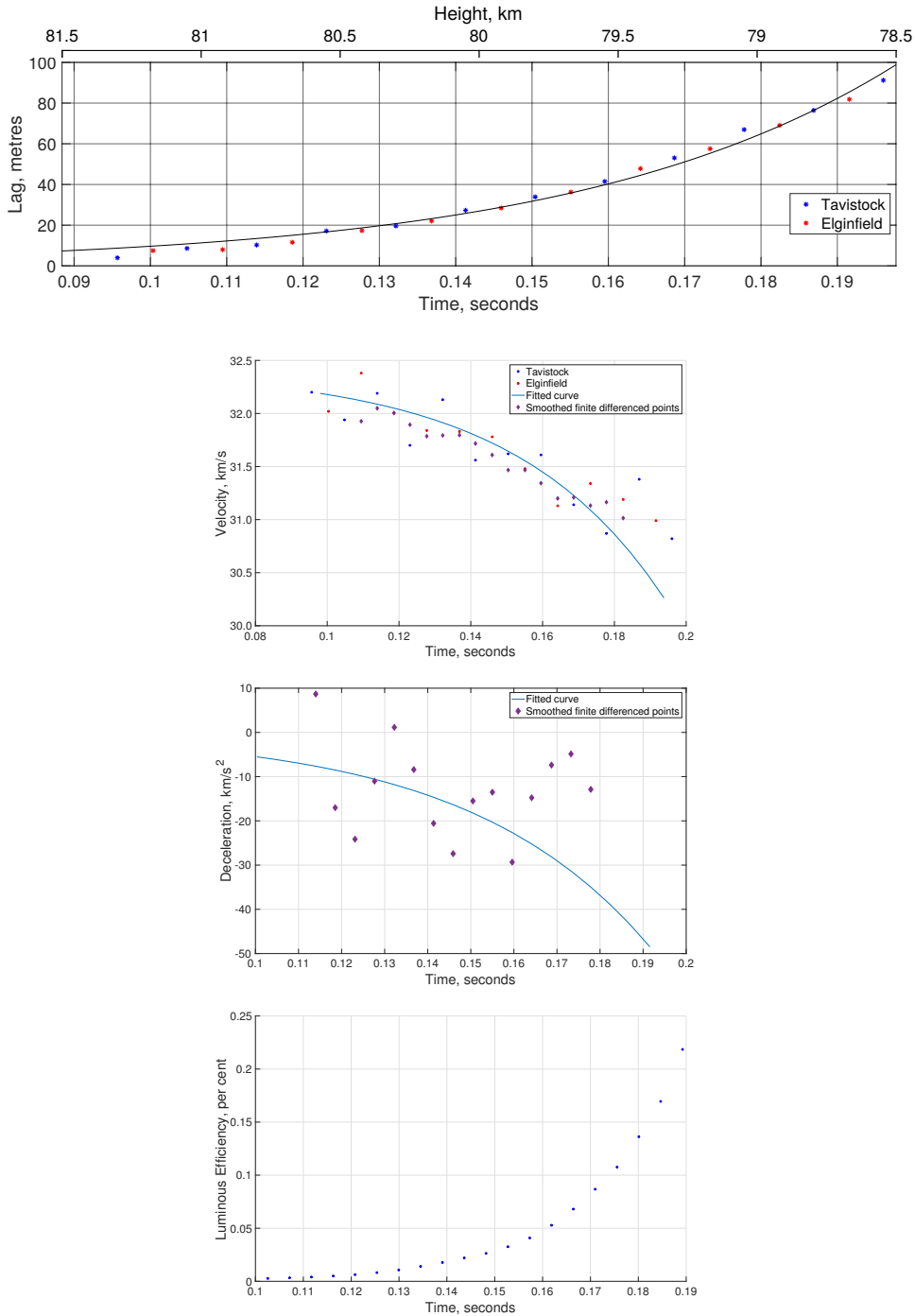


Figure 5.8: Meteor event 20161009_064237. The top plot shows the second half of the meteor lag data (with the data points coloured by station), fit with a single-term exponential. The second plot shows the speed curve derived from the fitted lag. The cyan points are lag data points finite differenced over a larger separation to reduce the scatter. The third plot shows the deceleration curve and the finite differenced values (also over a larger separation to reduce scatter). The bottom plot shows the resulting luminous efficiency profile, based on the speed and deceleration curves, with an initial meteoroid density of 3190 kg/m³; drag coefficient 1; shape factor 1.21.

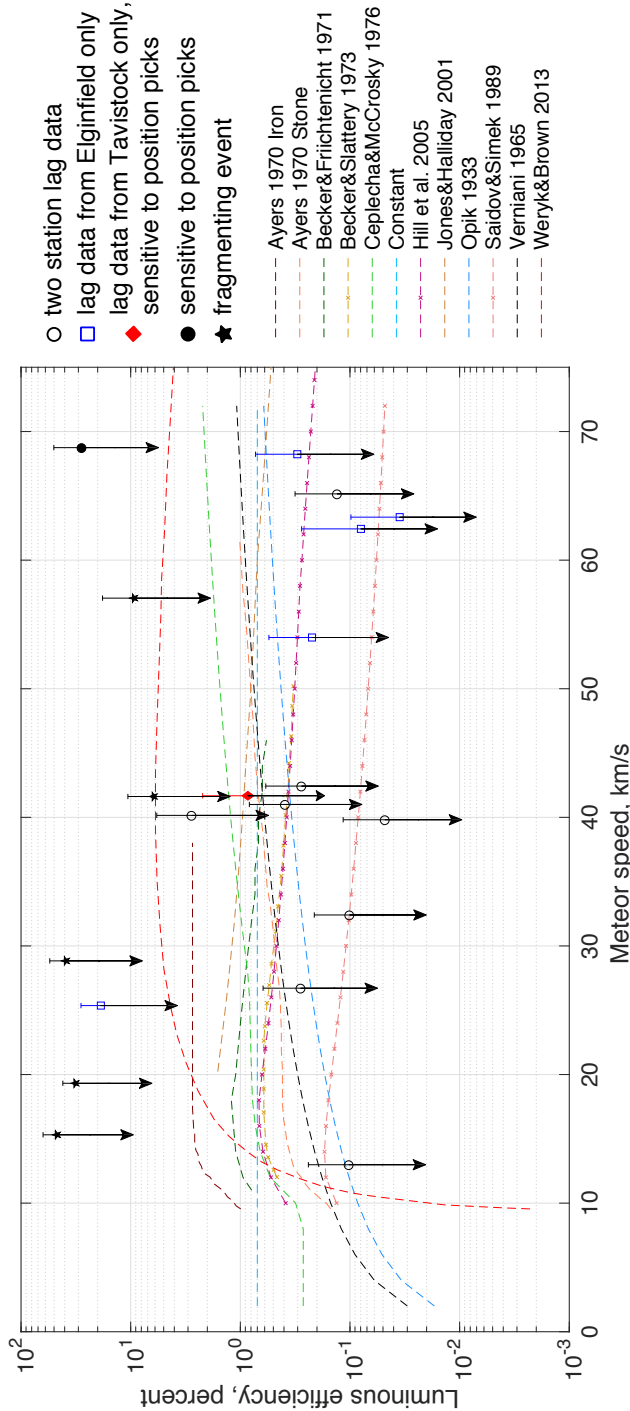


Figure 5.9: Luminous efficiency as a function of initial speed. Note that the initial meteor speed is based on the entire meteoroid ablation profile, and not where the single-term exponential begins. The curves showing other studies have not been corrected to a particular bandpass. The instruments used in the Weryk & Brown (2013) study are the same ones used in this study, but their results are bolometric values.

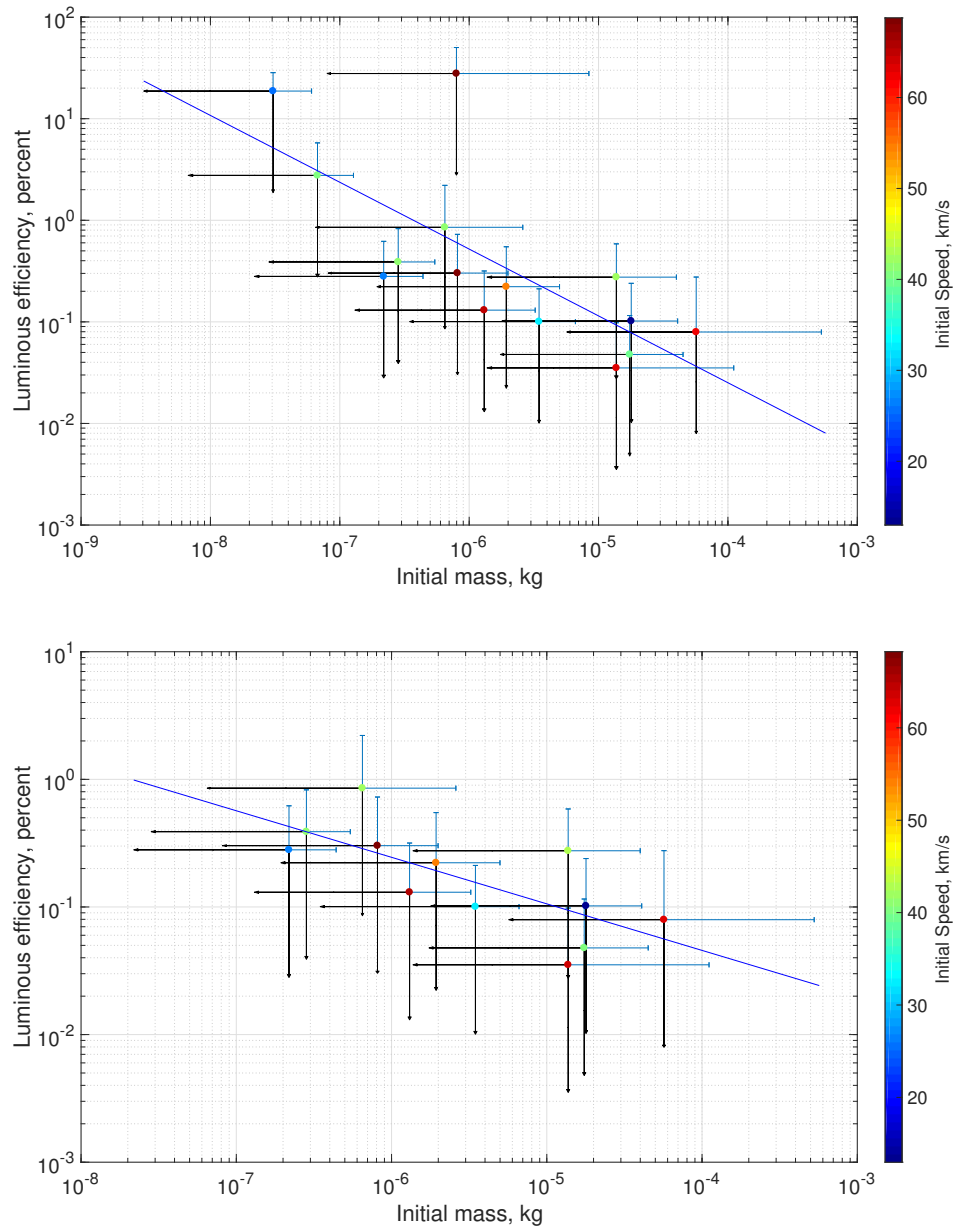


Figure 5.10: Luminous efficiency as a function of initial mass for non-fragmenting events. Each meteor event is coloured according to its initial speed, with the scale given in the colour-bar. The upper figure includes all leading fragment and single-body events (and the line of best fit has a slope of -0.6578 and an intercept of -4.2303 in log-log space), while the lower figure excluded events from that set that were sensitive to position picks (and has a slope of -0.3647 and an intercept of -2.7994 , in log-log space).

5.4.9 Fragmentation

Five meteors showing obvious fragmentation (long distinct trails) were analysed with this method. These events served as a sanity check to see whether meteors showing fragmentation will result in unphysical luminous efficiencies, much greater than 100%. To be able to plot these results, we ignored luminous efficiency values greater than 100% when computing the average. A clear distinction between the fragmenting and non-fragmenting meteor events can be seen in Figure 5.9.

5.5 Discussion

As discussed in Subasinghe et al. (2017), our method involves fitting the second half of the lag because the luminous efficiency can only be calculated in the part of the trajectory with maximum deceleration. For ideal data, the change in functional fit from a two-term exponential to a single exponent worsened the agreement of values given in Table 1 of Subasinghe et al. (2017) with the 0.7% constant luminous efficiency used to simulate the events. In spite of this, the single-term exponential is a better choice for real data with noise.

To test the effect of the fit on the derived luminous efficiency values, and as an extension of the work done in Subasinghe et al. (2017), a simple polynomial ($\text{lag} = ax^3 + bx^2 + cx + d$, which gives a linear deceleration) was fit to meteor event 20161009_064237. The polynomial could not be of order two or less, as that resulted in a constant deceleration, meaning the dynamic mass was not changing. The luminous efficiency was also determined using a simple point to point method, in which the mean deceleration was determined for two different sections of the meteor data near the end of ablation (resulting in two deceleration values). These were used to find a dynamic mass, compared to the photometric mass lost between those points and used to calculate the luminous efficiency. These two methods found luminous efficiency values that were within a factor of three of the value determined by fitting a single-term exponential function to the second half of the meteor lag data. The exponential fit was used for this analysis

as it best describes the atmospheric density that is encountered by the meteoroid.

We analysed fifteen non-fragmenting meteors, which is a very small fraction of the thousands recorded by CAMO. However, as seen in Figure 5.5, the images for the thirteen leading fragment events show very little to no wake, suggesting fragmentation is not important and that they can be treated as single bodies validating our method and results. Two of the meteor events (20150716_052934 and 20150915_084106) analysed show single-body ablation (but are not leading fragment events); however, they are likely undergoing fragmentation on a scale that we cannot resolve, as with the CAMO meteor in Campbell-Brown (2017) which appeared to have negligible wake but could only be modelled with significant fragmentation. Thus those two results should be considered upper limits on the luminous efficiency for those events - the determined dynamic mass (which considers only the largest fragment) will be less than the photometric mass (which considers light production from all fragments), and for the same amount of light production, this would cause the luminous efficiency to be artificially increased.

Our simulated noise analysis shows that for low (10^{-6} kg), mid (10^{-5} kg), and high-mass meteors (10^{-4} kg), low speed meteors are most likely to produce luminous efficiency results closest to the value used in the simulation. This is likely because slower meteors decelerate more, so uncertainties affect the dynamic mass less than for fast meteors which ablate before they significantly decelerate. For the entire range of meteor speeds, our method tends to underestimate the luminous efficiency of meteors.

We used meteoroid bulk density values from Kikwaya et al. (2011) based on the Tisserand parameters of our meteor events. The results from Kikwaya et al. (2011) assumed a luminous efficiency value. To eliminate any bias this assumed luminous efficiency value may have had on our derived luminous efficiency results, we present the derived luminous efficiency results with meteoroid density 1000 kg/m^3 and 3000 kg/m^3 for each event, in Figure 5.11. Assuming a density of 1000 kg/m^3 has the effect of decreasing the calculated luminous efficiencies for slow meteors, while not significantly changing those of faster meteors, while assuming a density of 3000 kg/m^3 increases the calculated luminous efficiencies of fast meteors, while not

significantly changing those of slower meteors. Both assumed densities show an increase in calculated luminous efficiency with speed, while the density values from Kikwaya et al. (2011) and Kikwaya Eluo (2011) show a constant relationship with speed.

The main results of this work are presented in Figures 5.9 and 5.10. Our results are typically consistent with lower values of luminous efficiency from previous studies, and seem to rule out the highest luminous efficiencies. It is difficult to directly compare our results to others because several past studies knew the composition of their meteoroids (in the case of lab meteoroids, or artificial meteoroids). We attempt to account for this by exploring a large range of possible meteoroid densities.

Figure 5.10 shows that there is a relationship between luminous efficiency and initial mass, which is not related to meteoroid speed. Unexpectedly, it shows that meteoroids with smaller mass radiate light more efficiently than more massive meteoroids. The first plot in Figure 5.10 shows the linear fit (in log-log space) when including all the analysed meteor events, and the second figure excludes the three events that were found to be very sensitive to meteor position picks. The entire parameter space of drag coefficient, meteoroid density, shape factor, and random errors in position was searched, with random errors of up to half a pixel being added. Three of the fifteen events were found to be very sensitive to these position pick variations, leading to wildly different luminous efficiencies for similar position picks. Even when these three events are removed, a negative linear trend is still apparent in the luminous efficiency-mass plot. The uncertainty in each point is large, however, and more meteor events may cause this to change.

It is important to keep in mind the low number of meteor events studied here. While Figure 5.10 shows negative linear trends, these events are not necessarily representative of the entire population of meteors observed with the CAMO system. There are no meteors in the low luminous efficiency - low mass area of the plots in Figure 5.10: it is unlikely that the CAMO system could observe such faint meteors. However, there are also no high luminous efficiency - high mass meteors: the CAMO system should be able to see these bright meteors. One matter

of great interest is the dependence of luminous efficiency on speed, since some previous studies predict an increase (e.g. Verniani, 1965), and some a decrease with speed (e.g Hill et al., 2005). Our results using the densities of Kikwaya et al. (2011) show no clear trend with speed, while using a constant density there is a weak increase with speed. At low speeds, our results are even less conclusive; we have a single meteor event with an initial speed less than 20 km/s, which does not allow us to corroborate or reject the steep increase in luminous efficiency at low speeds typically found in past studies. The error in each event is typically greater than the derived luminous efficiency value, which makes it unreasonable to draw lower bounds on the luminous efficiency value with this study. This is indicated by downward pointing arrows. It is not unreasonable to assume that the trend in luminous efficiency with speed depends on the composition, with some atoms radiating more effectively at higher collision energies, and some less effectively. In this case, any trend will be masked if the meteoroids have different compositions.

An important note is that thirteen of our fifteen meteor events were leading (or terminal) fragments. These fragments were composed of the strongest material in the meteoroid, which is implied by the fact that they continued to ablate after most of the meteoroid had ablated. These fragments may have had a different composition (and therefore spectrum) from the rest of the meteoroid, which means they may have a different luminous efficiency than their parent meteoroid. It is therefore difficult to compare these leading fragment meteor events to other studies. For example, if the leading fragments contain little volatile sodium, they would produce less light than sodium-rich parts of the meteoroid.

5.6 Conclusion

This paper presents the most recent study of modern high-resolution meteor observations used to determine luminous efficiency, by comparing the dynamic and photometric masses. The second half of the observed meteor lag is fit with a single-term exponential, and the resulting

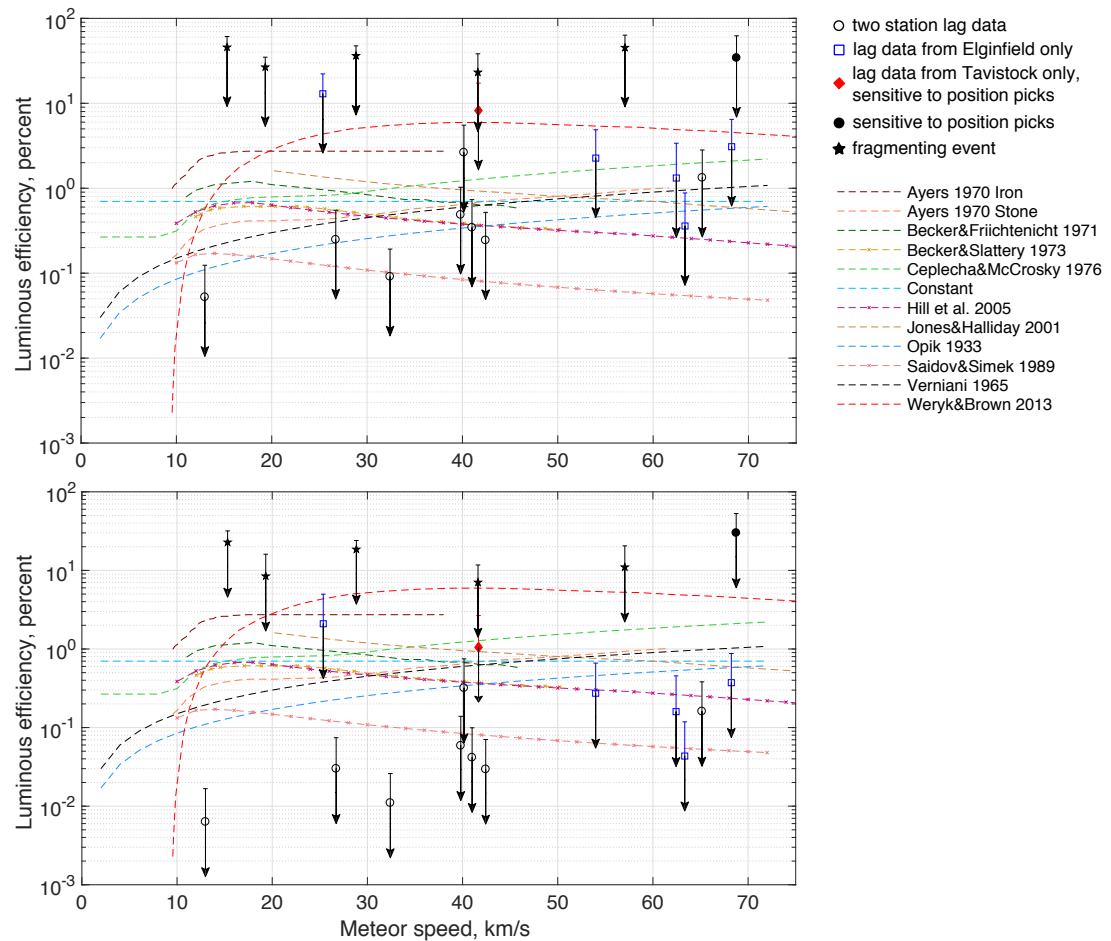


Figure 5.11: Luminous efficiency as a function of initial speed, assuming each meteoroid has a bulk density of 3000 kg/m^3 (upper plot), or 1000 kg/m^3 (lower plot).

speed and deceleration curves are used in conjunction with best fit values for meteoroid density, shape factor, and drag coefficient. To determine uncertainties, the entire phase space of potential values for the above parameters was searched. Fifteen meteor events were observed, thirteen of which displayed leading fragment behaviour (a fragment that persisted after the majority of the meteoroid had ablated, and showed essentially no fragmentation), and two which show as close to single-body ablation as we could find. While there is no obvious relationship found between luminous efficiency and initial meteor speed, this may be due to the variability of meteoroid compositions, on which we have gathered no information for this study. It is also difficult to directly compare our results to past studies (artificial meteoroids, lab studies, simultaneous radar/optical studies) as our leading fragment events are composed of the strongest material in each meteoroid, which may not necessarily be represented in past studies. There seems to be an unexpected negative linear relationship between luminous efficiency and initial meteoroid mass; however, as there are only fifteen events, this may not be meaningful. In the future, we will add spectral capabilities to the CAMO system and collect more data with the necessary high-resolution calibrations. This may cause relationships between luminous efficiency and other parameters (such as mass and speed) to reveal themselves.

Bibliography

- Ayers, W. G., McCrosky, R. E., & Shao, C.-Y. 1970, SAO Special Report, 317
- Becker, D. G., & Friichtenicht, J. F. 1971, *Astrophysical Journal*, 166, 699
- Becker, D. G., & Slattery, J. C. 1973, *Astrophysical Journal*, 186, 1127
- Borovicka, J. 1990, *Bulletin of the Astronomical Institutes of Czechoslovakia*, 41, 391
- Borovička, J., Koten, P., Spurný, P., Boček, J., & Štork, R. 2005, *Icarus*, 174, 15
- Campbell-Brown, M. 2017, *Planetary and Space Science*, 143, 34
- Campbell-Brown, M. D., & Koschny, D. 2004, *Astronomy and Astrophysics*, 418, 751
- Cepplecha, Z., Borovička, J., Elford, W. G., et al. 1998, *Space Science Reviews*, 84, 327
- Cepplecha, Z., & McCrosky, R. E. 1976, *Journal of Geophysical Research*, 81, 6257
- Friichtenicht, J. F., Slattery, J. C., & Tagliaferri, E. 1968, *Astrophysical Journal*, 151, 747
- Halliday, I., Griffin, A. A., & Blackwell, A. T. 1981, *Meteoritics*, 16, 153
- Hill, K. A., Rogers, L. A., & Hawkes, R. L. 2005, *Astronomy and Astrophysics*, 444, 615
- Jones, W., & Halliday, I. 2001, *Monthly Notices of the Royal Astronomical Society*, 320, 417
- Kikwaya, J.-B., Campbell-Brown, M., & Brown, P. G. 2011, *Astronomy & Astrophysics*, 530, A113
- Kikwaya Eluo, J.-B. 2011, PhD thesis, University of Western Ontario, <http://ir.lib.uwo.ca/etd/96>
- National Research Council. 2011, *Limiting Future Collision Risk to Spacecraft: An Assessment of NASA's Meteoroid and Orbital Debris Programs* (Washington, DC: The National Academies Press), doi:10.17226/13244

- Öpik, E. 1933, Atomic Collisions and Radiation of Meteors (Harvard Reprint No 100, Harvard College Observatory), reprinted from Acta et Commentationes Univ. Tartuensis (Dorpatensis) A26, Pt 2
- Picone, J. M., Hedin, A. E., Drob, D. P., & Aikin, A. C. 2002, Journal of Geophysical Research: Space Physics, 107, doi:10.1029/2002JA009430
- Saidov, K. H., & Simek, M. 1989, Bulletin of the Astronomical Institutes of Czechoslovakia, 40, 330
- Subasinghe, D., Campbell-Brown, M. D., & Stokan, E. 2016, Monthly Notices of the Royal Astronomical Society, 457, 1289
- . 2017, Planetary and Space Science, 143, 71
- Thomas, E., Horányi, M., Janches, D., et al. 2016, Geophysical Research Letters, 43, 3645
- Thomas, R. N., & Whipple, F. L. 1951, Astrophysical Journal, 114, 448
- Verniani, F. 1965, Smithsonian Contributions to Astrophysics, 8, 141
- Weryk, R. J., & Brown, P. G. 2012, Planetary and Space Science, 62, 132
- . 2013, Planetary and Space Science, 81, 32
- Weryk, R. J., Brown, P. G., Domokos, A., et al. 2008, Earth Moon and Planets, 102, 241
- Weryk, R. J., Campbell-Brown, M. D., Wiegert, P. A., et al. 2013, Icarus, 225, 614

Chapter 6

Conclusion

6.1 Thesis summary

The main goal of this thesis was to improve our understanding of the physical properties of faint meteors. As discussed in Chapter 1, it is difficult to study meteors because they ablate so quickly. A better understanding of these primitive bodies will provide information on not only the physical properties of asteroids and comets, but on the conditions in the early Solar system that allowed those bodies to form. To investigate current beliefs of meteor properties, high-resolution optical observations were combined with commonly used wide-field optical observations to explore fragmentation, strength, and origin. The feasibility of using the classical meteoroid ablation equations to determine the luminous efficiency was also studied. These equations were then applied to real meteor data, to determine the luminous efficiency values of each of the fifteen observed meteor events.

In Chapter 3, optical observations from narrow-field and wide-field cameras were combined in a survey on faint meteors. A total of 891 wide-field observations were analysed, and 1496 observations were studied with the narrow-field camera. Based on the observed light curve data, a smooth curve was interpolated based on the two station data, and classified according to its F parameter. The narrow-field data was manually classified according to the observed frag-

mentation behaviour, whether that was continuous fragmentation, negligible fragmentation, or gross fragmentation. A mean F parameter value of 0.49 was found for the 891 wide-field observations, which is in line with many other studies on light curves of faint meteors. The fragmentation mode was not found to be indicative of meteoroid origin: while comets might be expected to have some stronger material (Fulle et al., 2015), it is surprising that asteroidal material is just as weak. This may suggest that dynamical mixing has occurred, meaning that meteoroids classified as asteroidal actually come from Jupiter family comets, or that the Solar system is actually well mixed and our ideas on asteroids are biased because only the strongest material survives as meteorites. Meteors that showed little to no wake showed non-classical light curves, and this may imply that they are actually fragmenting: Campbell-Brown (2017) successfully modelled a CAMO observed meteor which showed minimal wake with an ablation model in which the object fragmented in many small bursts.

The luminous efficiency of meteors is poorly understood and past studies have suggested values that span two orders of magnitude. This leads to large uncertainties in meteoroid mass determinations. Chapter 4 presents an uncertainty analysis for the determination of luminous efficiency by equating dynamic and photometric masses. While this approach has been attempted in the past, it requires meteors that show no fragmentation and very precise position measurements, conditions that have only been properly met now. This method was found to be appropriate when applied to simulated meteor data, as the uncertainty in each parameter causes at most, a factor of two difference from the luminous efficiency used in the simulations. Precise deceleration values are needed to determine the luminous efficiency, and a thorough analysis of fits to the position data to determine deceleration found that an exponential fit is most appropriate, as it best represents the change in atmospheric density, and works best.

In Chapter 5 fifteen meteor events observed with the Canadian Automated Meteor Observatory were analysed, and their luminous efficiencies determined using this method. A single-term exponential was fit to the second half of the observed meteor lag, and the fit parameters were used to determine the deceleration. Combined with most likely values for other required

parameters, this allowed the luminous efficiency to be found. By exploring the parameter space of each variable, upper limits were placed on the results. Twelve of the fifteen meteor events were found to have luminous efficiency values of less than 1%, which agrees with lower results from past studies. However, no obvious relationship with speed was found. Most of the meteors observed in this study are comprised of the strongest material in the meteoroid, and because their compositions and spectra may differ from typical meteors, it is difficult to directly compare the results.

6.2 Future Work

Despite decades of meteoroid research, the physical properties of these small Solar system bodies are not well known. Studies that combine various types of observations (such as those described in Chapter 3) will continue to advance our knowledge. In particular, using high-resolution observations can improve our understanding of meteoroid ablation processes by providing new constraints for ablation models. As many studies have shown (e.g. Weryk et al., 2013; Subasinghe et al., 2017), meteor fragmentation is very common; however, within the broad category of fragmentation, there are different ways meteors can fragment (transversely vs along the line of motion; gross vs continuous) and further studies should investigate these to determine physical properties and to explore the physical processes that lead to fragmentation.

The study described in Chapter 3 found that fewer than 20% of meteor light curves studied showed double peaked shapes, and 15% showed flat light curves. A further investigation into these unusual light curve shapes should be attempted in the future, similar to work done by Roberts et al. (2014): including the high-resolution narrow-field observations may shed light on how these objects fragment, which would be crucial to accurately modelling them, and correctly determining physical properties like density.

While the high-resolution observations are valuable on their own, a spectral system would greatly improve the scientific output of CAMO by collecting information on meteoroid com-

positions. Because CAMO observes dozens of meteors each night, within a few months, a spectral system would provide data for a large survey of meteor compositions, which could be combined with observations of trajectories, light curve shapes, and fragmentation behaviour.

Additionally, a study on meteor luminous efficiency would be greatly enhanced with information about meteor compositions, or relative abundances of certain elements. Past studies were undertaken for known compositions (when studied in the lab, or with artificial meteoroids), and a spectral system would allow for a more direct comparison with these studies. In particular, having spectral line measurements for each part of a fragmenting meteor would determine whether leading fragments have the same or different luminous efficiencies from the bulk of the meteoroid, and might turn up the dependence on velocity of particular emission lines.

Bibliography

Campbell-Brown, M. 2017, *Planetary and Space Science*, 143, 34

Fulle, M., Della Corte, V., Rotundi, A., et al. 2015, *The Astrophysical Journal Letters*, 802, L12

Roberts, I. D., Hawkes, R. L., Weryk, R. J., et al. 2014, *Meteoroids 2013*, arXiv:1402.6002

Subasinghe, D., Campbell-Brown, M. D., & Stokan, E. 2017, *Planetary and Space Science*, 143, 71

Weryk, R. J., Campbell-Brown, M. D., Wiegert, P. A., et al. 2013, *Icarus*, 225, 614

Appendix A

Copyright Permissions

Journal: Monthly Notices of the Royal Astronomical Society

DOI: 10.1093/mnras/stw019

Title: Physical characteristics of faint meteors by light curve and high-resolution observations, and the implications for parent bodies

Standard Licence

You hereby grant to Oxford University Press an exclusive licence for the full period of copyright throughout the world:

- to publish the final version of the Article in the above Journal, and to distribute it and/or to communicate it to the public, either within the Journal, on its own, or with other related material throughout the world, in printed, electronic or any other format or medium whether now known or hereafter devised;
- to make translations and abstracts of the Article and to distribute them to the public;
- to authorize or grant licences to third parties to do any of the above;
- to deposit copies of the Article in online archives maintained by OUP or by third parties authorized by OUP.

You authorize us to act on your behalf to defend the copyright in the Article if anyone should infringe it and to register the copyright of the Article in the US and other countries, if necessary.

In the case of a multi authored article, you confirm that you are authorized by your co-authors to enter the licence on their behalf.

You confirm to OUP that the Article

- is your original work;
- has not previously been published (in print or electronic format), is not currently under consideration by another journal, or if it has already been submitted to other journal, it will be immediately withdrawn;
- will not be submitted for publication to any other journal following acceptance in the above Journal; and
- OUP will be the first publisher of the Article.

You warrant to OUP that

- no part of the Article is copied from any other work,
- you have obtained ALL the permissions required (for print and electronic use) for any material you have used from other copyrighted publications in the Article; and
- you have exercised reasonable care to ensure that the Article is accurate and does not contain anything which is libellous, or obscene, or infringes on anyone's copyright, right of privacy, or other rights.

Further Information

(Full details of OUP's publication rights policies, including author rights can be found at http://www.oxfordjournals.org/access_purchase/publication_rights.html)

Author Self-Archiving Policy

On publication of your Article in the Journal you are not required to remove any previously posted ORIGINAL VERSIONS from your own personal website or that of your employer or free public servers of articles in your subject area, provided (1) you include a link (url) to the VERSION OF RECORD on the Journal's website; AND (2) the Journal is attributed as the original place of publication with the correct citation details given.

You may post the ACCEPTED MANUSCRIPT or the VERSION OF RECORD onto your own website, your institution's website and in institutional or subject-based repositories upon publication, provided that: (1) you include a link (url) to the VERSION OF RECORD on the Journal's website; (2) the Journal is attributed as the original place of publication with the correct citation details given.

Free Link to Published Article

On publication of your article, you will receive a URL, giving you access to the published article on the Journal website, and information on use of this link.

Educational Use

You may use the Article within your employer's institution or company for educational or research purposes only, including use in course-packs, as long as: (1) you do not use it for commercial purposes or re-distribution outside of the institution/company; (2) you acknowledge the Journal as the original place of publication with the correct citation details given.

Dilini Subasinghe signed this licence on 2016-01-07 16:14:23 GMT.

ELSEVIER LICENSE TERMS AND CONDITIONS

Sep 28, 2017

This Agreement between Ms. Dilini Subasinghe ("You") and Elsevier ("Elsevier") consists of your license details and the terms and conditions provided by Elsevier and Copyright Clearance Center.

License Number	4197680537159
License date	Sep 28, 2017
Licensed Content Publisher	Elsevier
Licensed Content Publication	Planetary and Space Science
Licensed Content Title	Luminous efficiency estimates of meteors -I. Uncertainty analysis
Licensed Content Author	Dilini Subasinghe, Margaret Campbell-Brown, Edward Stokan
Licensed Content Date	Sep 1, 2017
Licensed Content Volume	143
Licensed Content Issue	n/a
Licensed Content Pages	7
Start Page	71
End Page	77
Type of Use	reuse in a thesis/dissertation
Portion	full article
Format	both print and electronic
Are you the author of this Elsevier article?	Yes
Will you be translating?	No
Title of your thesis/dissertation	Physical properties of faint meteors through high-resolution observations
Expected completion date	Nov 2017
Estimated size (number of pages)	130
Requestor Location	Dilini Subasinghe Department of Physics and Astronomy 1151 Richmond Street London, ON N6A 3K7 Canada Attn: Ms. Dilini Subasinghe
Total	0.00 CAD

Terms and Conditions

INTRODUCTION

1. The publisher for this copyrighted material is Elsevier. By clicking "accept" in connection with completing this licensing transaction, you agree that the following terms and conditions apply to this transaction (along with the Billing and Payment terms and conditions established by Copyright Clearance Center, Inc. ("CCC"), at the time that you opened your Rightslink account and that are available at any time at <http://myaccount.copyright.com>).

GENERAL TERMS

2. Elsevier hereby grants you permission to reproduce the aforementioned material subject to the terms and conditions indicated.
3. Acknowledgement: If any part of the material to be used (for example, figures) has appeared in our publication with credit or acknowledgement to another source, permission must also be sought from that source. If such permission is not obtained then that material may not be included in your publication/copies. Suitable acknowledgement to the source must be made, either as a footnote or in a reference list at the end of your publication, as follows:
"Reprinted from Publication title, Vol /edition number, Author(s), Title of article / title of chapter, Pages No., Copyright (Year), with permission from Elsevier [OR APPLICABLE SOCIETY COPYRIGHT OWNER]." Also Lancet special credit - "Reprinted from The Lancet, Vol. number, Author(s), Title of article, Pages No., Copyright (Year), with permission from Elsevier."
4. Reproduction of this material is confined to the purpose and/or media for which permission is hereby given.
5. Altering/Modifying Material: Not Permitted. However figures and illustrations may be altered/adapted minimally to serve your work. Any other abbreviations, additions, deletions and/or any other alterations shall be made only with prior written authorization of Elsevier Ltd. (Please contact Elsevier at permissions@elsevier.com). No modifications can be made to any Lancet figures/tables and they must be reproduced in full.
6. If the permission fee for the requested use of our material is waived in this instance, please be advised that your future requests for Elsevier materials may attract a fee.
7. Reservation of Rights: Publisher reserves all rights not specifically granted in the combination of (i) the license details provided by you and accepted in the course of this licensing transaction, (ii) these terms and conditions and (iii) CCC's Billing and Payment terms and conditions.
8. License Contingent Upon Payment: While you may exercise the rights licensed immediately upon issuance of the license at the end of the licensing process for the transaction, provided that you have disclosed complete and accurate details of your proposed use, no license is finally effective unless and until full payment is received from you (either by publisher or by CCC) as provided in CCC's Billing and Payment terms and conditions. If full payment is not received on a timely basis, then any license preliminarily granted shall be deemed automatically revoked and shall be void as if never granted. Further, in the event that you breach any of these terms and conditions or any of CCC's Billing and Payment terms and conditions, the license is automatically revoked and shall be void as if never granted. Use of materials as described in a revoked license, as well as any use of the materials beyond the scope of an unrevoked license, may constitute copyright infringement and publisher reserves the right to take any and all action to protect its copyright in the materials.
9. Warranties: Publisher makes no representations or warranties with respect to the licensed material.
10. Indemnity: You hereby indemnify and agree to hold harmless publisher and CCC, and their respective officers, directors, employees and agents, from and against any and all claims arising out of your use of the licensed material other than as specifically authorized pursuant to this license.
11. No Transfer of License: This license is personal to you and may not be sublicensed, assigned, or transferred by you to any other person without publisher's written permission.
12. No Amendment Except in Writing: This license may not be amended except in a writing signed by both parties (or, in the case of publisher, by CCC on publisher's behalf).
13. Objection to Contrary Terms: Publisher hereby objects to any terms contained in any purchase order, acknowledgment, check endorsement or other writing prepared by you, which terms are inconsistent with these terms and conditions or CCC's Billing and Payment terms and conditions. These terms and conditions, together with CCC's Billing and Payment

terms and conditions (which are incorporated herein), comprise the entire agreement between you and publisher (and CCC) concerning this licensing transaction. In the event of any conflict between your obligations established by these terms and conditions and those established by CCC's Billing and Payment terms and conditions, these terms and conditions shall control.

14. **Revocation:** Elsevier or Copyright Clearance Center may deny the permissions described in this License at their sole discretion, for any reason or no reason, with a full refund payable to you. Notice of such denial will be made using the contact information provided by you. Failure to receive such notice will not alter or invalidate the denial. In no event will Elsevier or Copyright Clearance Center be responsible or liable for any costs, expenses or damage incurred by you as a result of a denial of your permission request, other than a refund of the amount(s) paid by you to Elsevier and/or Copyright Clearance Center for denied permissions.

LIMITED LICENSE

The following terms and conditions apply only to specific license types:

15. **Translation:** This permission is granted for non-exclusive world **English** rights only unless your license was granted for translation rights. If you licensed translation rights you may only translate this content into the languages you requested. A professional translator must perform all translations and reproduce the content word for word preserving the integrity of the article.

16. **Posting licensed content on any Website:** The following terms and conditions apply as follows: Licensing material from an Elsevier journal: All content posted to the web site must maintain the copyright information line on the bottom of each image; A hyper-text must be included to the Homepage of the journal from which you are licensing at <http://www.sciencedirect.com/science/journal/xxxxx> or the Elsevier homepage for books at <http://www.elsevier.com>; Central Storage: This license does not include permission for a scanned version of the material to be stored in a central repository such as that provided by Heron/XanEdu.

Licensing material from an Elsevier book: A hyper-text link must be included to the Elsevier homepage at <http://www.elsevier.com>. All content posted to the web site must maintain the copyright information line on the bottom of each image.

Posting licensed content on Electronic reserve: In addition to the above the following clauses are applicable: The web site must be password-protected and made available only to bona fide students registered on a relevant course. This permission is granted for 1 year only. You may obtain a new license for future website posting.

17. **For journal authors:** the following clauses are applicable in addition to the above:

Preprints:

A preprint is an author's own write-up of research results and analysis, it has not been peer-reviewed, nor has it had any other value added to it by a publisher (such as formatting, copyright, technical enhancement etc.).

Authors can share their preprints anywhere at any time. Preprints should not be added to or enhanced in any way in order to appear more like, or to substitute for, the final versions of articles however authors can update their preprints on arXiv or RePEc with their Accepted Author Manuscript (see below).

If accepted for publication, we encourage authors to link from the preprint to their formal publication via its DOI. Millions of researchers have access to the formal publications on ScienceDirect, and so links will help users to find, access, cite and use the best available version. Please note that Cell Press, The Lancet and some society-owned have different preprint policies. Information on these policies is available on the journal homepage.

Accepted Author Manuscripts: An accepted author manuscript is the manuscript of an article that has been accepted for publication and which typically includes author-incorporated changes suggested during submission, peer review and editor-author communications.

Authors can share their accepted author manuscript:

- immediately
 - via their non-commercial person homepage or blog
 - by updating a preprint in arXiv or RePEc with the accepted manuscript
 - via their research institute or institutional repository for internal institutional uses or as part of an invitation-only research collaboration work-group
 - directly by providing copies to their students or to research collaborators for their personal use
 - for private scholarly sharing as part of an invitation-only work group on commercial sites with which Elsevier has an agreement
- After the embargo period
 - via non-commercial hosting platforms such as their institutional repository
 - via commercial sites with which Elsevier has an agreement

In all cases accepted manuscripts should:

- link to the formal publication via its DOI
- bear a CC-BY-NC-ND license - this is easy to do
- if aggregated with other manuscripts, for example in a repository or other site, be shared in alignment with our hosting policy not be added to or enhanced in any way to appear more like, or to substitute for, the published journal article.

Published journal article (JPA): A published journal article (PJA) is the definitive final record of published research that appears or will appear in the journal and embodies all value-adding publishing activities including peer review co-ordination, copy-editing, formatting, (if relevant) pagination and online enrichment.

Policies for sharing publishing journal articles differ for subscription and gold open access articles:

Subscription Articles: If you are an author, please share a link to your article rather than the full-text. Millions of researchers have access to the formal publications on ScienceDirect, and so links will help your users to find, access, cite, and use the best available version. Theses and dissertations which contain embedded PJAs as part of the formal submission can be posted publicly by the awarding institution with DOI links back to the formal publications on ScienceDirect.

If you are affiliated with a library that subscribes to ScienceDirect you have additional private sharing rights for others' research accessed under that agreement. This includes use for classroom teaching and internal training at the institution (including use in course packs and courseware programs), and inclusion of the article for grant funding purposes.

Gold Open Access Articles: May be shared according to the author-selected end-user license and should contain a [CrossMark logo](#), the end user license, and a DOI link to the formal publication on ScienceDirect.

Please refer to Elsevier's [posting policy](#) for further information.

18. **For book authors** the following clauses are applicable in addition to the above:

Authors are permitted to place a brief summary of their work online only. You are not allowed to download and post the published electronic version of your chapter, nor may you scan the printed edition to create an electronic version. **Posting to a repository:** Authors are permitted to post a summary of their chapter only in their institution's repository.

19. **Thesis/Dissertation:** If your license is for use in a thesis/dissertation your thesis may be submitted to your institution in either print or electronic form. Should your thesis be published commercially, please reapply for permission. These requirements include permission for the Library and Archives of Canada to supply single copies, on demand, of the complete thesis and include permission for Proquest/UMI to supply single copies, on demand, of the complete thesis. Should your thesis be published commercially, please

reapply for permission. Theses and dissertations which contain embedded PJAs as part of the formal submission can be posted publicly by the awarding institution with DOI links back to the formal publications on ScienceDirect.

Elsevier Open Access Terms and Conditions

You can publish open access with Elsevier in hundreds of open access journals or in nearly 2000 established subscription journals that support open access publishing. Permitted third party re-use of these open access articles is defined by the author's choice of Creative Commons user license. See our [open access license policy](#) for more information.

Terms & Conditions applicable to all Open Access articles published with Elsevier:

Any reuse of the article must not represent the author as endorsing the adaptation of the article nor should the article be modified in such a way as to damage the author's honour or reputation. If any changes have been made, such changes must be clearly indicated.

The author(s) must be appropriately credited and we ask that you include the end user license and a DOI link to the formal publication on ScienceDirect.

If any part of the material to be used (for example, figures) has appeared in our publication with credit or acknowledgement to another source it is the responsibility of the user to ensure their reuse complies with the terms and conditions determined by the rights holder.

Additional Terms & Conditions applicable to each Creative Commons user license:

CC BY: The CC-BY license allows users to copy, to create extracts, abstracts and new works from the Article, to alter and revise the Article and to make commercial use of the Article (including reuse and/or resale of the Article by commercial entities), provided the user gives appropriate credit (with a link to the formal publication through the relevant DOI), provides a link to the license, indicates if changes were made and the licensor is not represented as endorsing the use made of the work. The full details of the license are available at <http://creativecommons.org/licenses/by/4.0>.

CC BY NC SA: The CC BY-NC-SA license allows users to copy, to create extracts, abstracts and new works from the Article, to alter and revise the Article, provided this is not done for commercial purposes, and that the user gives appropriate credit (with a link to the formal publication through the relevant DOI), provides a link to the license, indicates if changes were made and the licensor is not represented as endorsing the use made of the work. Further, any new works must be made available on the same conditions. The full details of the license are available at <http://creativecommons.org/licenses/by-nc-sa/4.0>.

CC BY NC ND: The CC BY-NC-ND license allows users to copy and distribute the Article, provided this is not done for commercial purposes and further does not permit distribution of the Article if it is changed or edited in any way, and provided the user gives appropriate credit (with a link to the formal publication through the relevant DOI), provides a link to the license, and that the licensor is not represented as endorsing the use made of the work. The full details of the license are available at <http://creativecommons.org/licenses/by-nc-nd/4.0>.

Any commercial reuse of Open Access articles published with a CC BY NC SA or CC BY NC ND license requires permission from Elsevier and will be subject to a fee.

Commercial reuse includes:

- Associating advertising with the full text of the Article
- Charging fees for document delivery or access
- Article aggregation
- Systematic distribution via e-mail lists or share buttons

Posting or linking by commercial companies for use by customers of those companies.

20. Other Conditions:

v1.9

Questions? customer@copyright.com or +1-855-239-3415 (toll free in the US) or

+1-978-646-2777.

Curriculum Vitae

Dilini Subasinghe

Department of Physics and Astronomy
1151 Richmond Street
London, Ontario, Canada
N6A 3K7

Education

Doctor of Philosophy (Astronomy)
University of Western Ontario
London, Ontario, Canada
2013 - 2017

Master of Science (Astronomy & Planetary Science)
University of Western Ontario
London, Ontario, Canada
2011 - 2012

Bachelor of Science Honors (Planetary Science)
University of Western Ontario
London, Ontario, Canada
2006 - 2010

Honours and Awards

Ontario Graduate Scholarship 2015-2016
Department of Physics and Astronomy Teaching Assistant Award 2010-2011

Related Work Experience

Teaching Assistant, Physics and Astronomy, The University of Western Ontario 2011 - 2017

Publications

1. **Subasinghe, D.**, and Campbell-Brown, M. D. 2017, “Luminous efficiency estimates of meteors -II. Application to Canadian Automated Meteor Observatory meteor events.” *The Astronomical Journal*, in press.
2. **Subasinghe, D.**, Campbell-Brown, M. D., and Stokan, E. 2017, “Luminous Efficiency Estimates of Meteors -I. Uncertainty Analysis.” *Planetary and Space Science*, 143, 71.
3. **Subasinghe, D.**, Campbell-Brown, M. D., and Stokan, E. 2016, “Physical characteristics of faint meteors by light curve and high-resolution observations, and the implications for parent bodies.” *Monthly Notices of the Royal Astronomical Society*, 457, 1289.
4. Roberts, I. D., Hawkes, R. L., Weryk, R. J., Campbell-Brown, M. D., Brown, P. G., Stokan, E., and **Subasinghe, D.** 2014, “Meteoroid structure and ablation implications from multiple maxima meteor light curves.” *Meteoroids 2013*.
5. **Subasinghe, D.**, and Wiegert P. A. 2013, “On the Use of Meteor Camera Systems in the Detection of Kuiper Belt Objects through Serendipitous Stellar Occultations.” *Earth, Moon, and Planets*, 111, 89.